DETERMINATION OF STRESS IN LATERALLY OVERGROWN GaN AND UNDERLYING DIAMOND STRIPES OF DIFFERENT DIMENSION BY VISIBLE RAMAN SPECTROSCOPY

by

Chhabindra Gautam, B.S.

A thesis submitted to the Graduate Council of
Texas State University in partial fulfillment
of the requirements for the degree of
Master of Science
with a Major in Physics
May 2020

Committee Members:

Edwin L. Piner, Chair

Mark W. Holtz

Alexander Zakhidov

COPYRIGHT

by

Chhabindra Gautam

2020

FAIR USE AND AUTHOR'S PERMISSION STATEMENT

Fair Use

Duplication Permission

DEDICATION

I am dedicating this work to my parents, Bhim Lal Sharma and Gopika Gautam.

ACKNOWLEDGMENTS

I am very fortunate to have had the opportunity to work and grow alongside many fine individuals throughout my graduate experience in M.S. Physics at Texas State University. I would like to thank my advisor Dr. Edwin L Piner for his support and personal investment in his students and his graceful abilities to teach and motivate. I would also like to thank my committee members Dr. Mark W Holtz and Dr. Alexander Zakhidov for their guidance and patience. I would like to thank Texas State's ARSC and NRSC technical teams and support staff with special acknowledgment to Dr. Casey Smith. I would like to thank all my seniors Dr. Raju Ahmed, Mr. Jonathan W Anderson, Dr. Anwar Siddique, Dr. Sandeep Sohal who helped me to finalize my project. The National Science Foundation (NSF) deserves a big thanks for providing me financial support for my thesis. I am extraordinarily grateful for my family, which encompasses a list of exceptional individuals too long to enumerate and too important to describe. Their continual encouragement and unconditional support throughout my work are invaluable.

TABLE OF CONTENTS

Page

LIST OF TABLES

Table **Page**

LIST OF FIGURES

Figure **Page**

LIST OF ABBREVIATIONS

Abbreviation	Description
HEMT	High Electron Mobility Transistors
ELO	Epitaxial Lateral Over-growth
NDC	Non-Diamond Carbon
MOCVD	Metal Organic Chemical Vapor Deposition
HFCVD	Hot filament Chemical Vapor Deposition
CVD	Chemical Vapor Deposition
RIE	Reactive Ionized Etching
ND	Nano Diamond
SEM	Scanning Electron Microscope
DMSO	Dimethyl Sulfoxide
PECVD	Plasma Enhanced Chemical Vapor Deposition
TMG	Trimethyl Gallium

ABSTRACT

Wide bandgap semiconductors forming High Electron Mobility Transistors (HEMT) have shown promise in RF technology, space science, and many other sectors which require high power. The local heat produced in the HEMT structure during its operation lowers its efficiency. However, this efficiency may be increased if a highly thermally conductive thin film such as diamond grown via Chemical Vapor Deposition (CVD) can be combined with the HEMT. Epitaxial Lateral Overgrowth (ELO) of GaN on selectively deposited diamond stripes offers the additional benefit that it does not include a barrier layer between the GaN and the Diamond interface. High thermal conductivity across the GaN-Diamond interface is expected because there is no barrier layer in between them. High thermal conductivity between GaN and Diamond will greatly improve thermal management within RF and power electronic HEMTs.

The way ELO GaN grows over the diamond stripes and the high lattice and thermal mismatches between GaN and diamond have led to the present investigation about the nature of the stress distribution on the GaN and diamond stripes. The primary objective is to ascertain the stress distribution at the ELO GaN and window GaN, and on the diamond stripes near the GaN-Diamond interface. The stress on the diamond stripes without ELO GaN has been previously determined, but this stress distribution should change after the ELO GaN layer is deposited. Furthermore, different dimensions of the stripes are expected to influence the stress distribution at the surfaces in question. Since stress significantly impacts device performance and dislocation density within the layers, results from this research will be very useful in estimating the overall efficiency of HEMT devices with and without diamond stripes.

The present studies determined the ELO GaN stress distribution by Raman spectroscopy over the diamond stripes and validated the results with Transmission Electron Microscopy and COMSOL modelling. The lower tensile stress above the diamond stripes is attributed to uncoalesced GaN wings and various defects present near the coalescence region. The gap located in between overgrown GaN and diamond is also contributing to lower ELO GaN stress. In addition to GaN stress, the underlying diamond and Si stress behavior has been mapped. The diamond stress was found compressive with maximum value at the center of the stripe while the Si substrate was found to be relaxed due to the intermediate nitride layers in between diamond and Si substrate. Furthermore, ELO and coherently grown GaN quality are compared by presenting defect distribution and symmetry breaking Raman modes. Finally, the stress distribution along the GaN growth direction is discussed which will enable the determination of the ELO GaN conditions needed to optimally grow high thermal transport III-Nitride devices.

1. INTRODUCTION

The formation of a diamond layer in contact with the GaN HEMT structure is expected to allow the local heat produced in those structures to pass rapidly through the high thermally conductive diamond. Due to the harsh diamond growth environment, rough diamond surface and the large lattice and thermal mismatch between GaN and diamond, epitaxial growth of diamond (GaN) directly on GaN (Diamond) has been challenging for many years. Recently ELO of GaN over the diamond stripes is receiving increasing interest as it has no intermediate layer, which is expected to reduce the stress and thermal boundary resistance[1]. The expected stress should reduce because the GaN layer is grown only over diamond stripes and not over an entire diamond substrate. The thermal boundary conductance is expected to significantly improve due to the absence of an interfacial (passivation) layer between GaN-Diamond.

Previous studies of ELO GaN over diamond stripes show a lower threading dislocation defect density, less Non-Diamond Carbon (NDC) on the diamond stripes, and better interface between the GaN and Diamond compared to all other techniques developed for GaN-diamond integration to date [1]. From various literature reports on the ELO growth mechanism the ELO GaN quality is better because the stripes over which GaN is grown acts as a barrier for the vertical propagation of dislocations [2]. In a similar way, diamond stripes minimize threading dislocation propagation above it, leading to very good crystalline quality GaN above the diamond stripes. Hence, quantification of stress in the ELO GaN is important to advance this approach. Formation of diamond stripes instead of a blanket diamond layer reduces the global stress, though some local stress near the diamond stripes is expected. The lower NDC content in the diamond stripe is due to the optimized CVD growth conditions and the GaN growth process. I.e., epitaxial and then lateral GaN growth is expected to improve the GaN-diamond interface [1]. Device performance and the dislocation density are affected by the stress distribution in the microstructure of the device, so the distribution of stress in ELO GaN, near

the coalescence regions of the GaN layer, as well as at the edge and center of the diamond stripes are investigated.

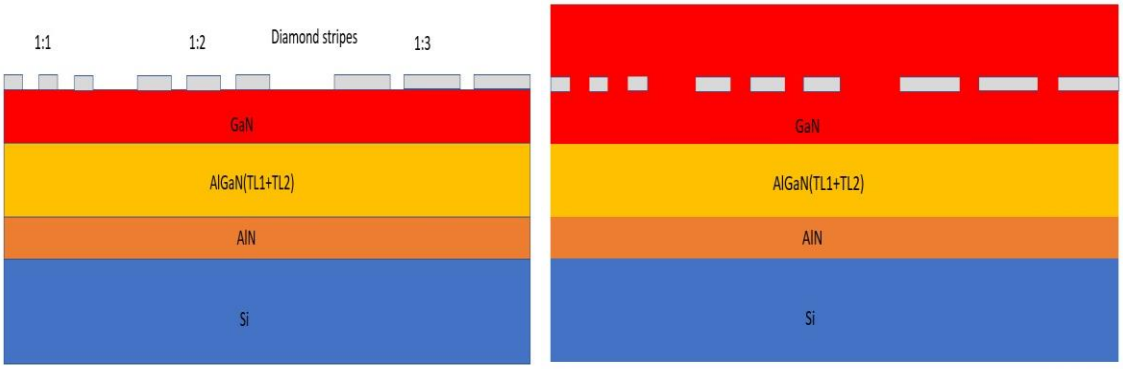

Figure 1: Schematic of material layers showing patterns of diamond stripes (Left), and ELO GaN (Right).

An approximately 2 µm thick structure consisting of a nucleation layer (AlN), two transition layers (AlGaN) and a buffer layer (GaN) was grown by Metal Organic Chemical Vapor Deposition (MOCVD). This initial structure was followed by the growth of SiN_x as a passivation layer, then diamond stripes with a thickness of ~ 250 nm were deposited on the GaN by hot filament CVD and finally a GaN layer ranging from 5-15 µm was grown between and over the diamond stripes. A schematic of the cross section of the sample is shown in Figure 1. The regrown GaN (i.e., second GaN growth process) grows first epitaxially over the non-diamond regions and then grows laterally above the diamond stripes. The thicknesses of ELO GaN are different on various samples investigated, as these samples were originally grown for an experiment to determine the growth conditions that yield coalesced and less defective ELO GaN layers. The samples under study were grown with different GaN thicknesses above diamond stripes of different dimensions. The primary objective of this study on the ELO GaN-diamond samples is to characterize both the ELO GaN and diamond stripes by using Raman spectroscopy. Although this sample structure is unique and new, literature suggests [3] that ELO GaN should have a stress pattern across the coalescence region and at the non-stripe region which can be

quantified with the phonon shift calculation. The primary reason for the stress in these kinds of thin films is the chamber environment during growth and subsequent cooling of the sample. In the work, the final GaN layer is grown at ~ 1030 °C and at this high temperature the structure is in a stress-free state. However, stress is induced in the sample as time progresses and it cools to room temperature. Because of the different coefficient of thermal expansion (CTE) of the GaN and diamond layers, as well as the silicon substrate, an equal temperature change creates a differing dimensional change and is the primary reason for thermal stress in these material structures. Our group has already published results investigating the stress distribution over diamond stripes. However, this stress distribution is likely different when stripe size is small and GaN is grown just above them without a barrier layer. This research will provide critical insight into the stress distribution of these newly developed GaN-Diamond microstructures. Finally, COMSOL Multiphysics will be used to theoretically model the stress above the diamond stripes and to verify the experimental results.

1.1 Selective Deposition of Diamond Stripes

The wide bandgap community has been investigating ways to deposit a diamond thin film over a HEMT device [4] for nearly two decades. The problem is that depositing a diamond thin film over the AlGaN/GaN HEMT causes a high global stress due to the difference in CTE and lattice mismatch between GaN and diamond [5, 6]. Recently, Ahmed et.al. [7] discovered a new technique to selectively deposit diamond on GaN to form stripes, which reduces the global stress at the diamond-GaN interface, although there are some local stress, as expected. Ahmad et.al. found very low interfacial Si-diamond roughness, NDC content and only local (not global) stress when the diamond stripes were grown directly over a Si substrate. The formation of these diamond stripes was made possible by selective seeding of the substrate. First the entire wafer was seeded then exposed to UV under an appropriate mask and developed in order to remove unwanted seeds, resulting in stripes of diamond nano seeds in the desired stripe

pattern. To further improve selectivity, Reactive Ionized Etching (RIE) was employed in the unseeded area so that during CVD growth only the seed laden area are populated by diamond crystals.

1.2 Epitaxial Lateral Overgrowth of GaN Over Diamond

Lateral overgrowth of GaN directly over the diamond stripes is a totally new material structure that is expected to overcome the challenges of integrating AlGaN/GaN HEMTs with diamond for thermal management. The ELO GaN over diamond is promising in regard to thermal management as it does not require an interfacial passivation layer between the diamond and the GaN. The presence of an interfacial layer acts as a thermal barrier which increase the thermal boundary resistance and reduces the heat dissipation offered by the thermally conductive diamond [8]. This newly discovered structure is expected to improve the efficiency of the HEMT device because there is no additional thermal barrier, there are fewer defects in the regrown GaN layer, there is less interfacial roughness between GaN and the diamond, and the NDC content on the diamond stripes is low. Although ELO above diamond stripes is a new technique, various research on ELO GaN over other materials has been conducted. In particular, ELO GaN over dielectric materials was previously reported by Kuball et al. [3]. In this paper, the Raman stress mapping of ELO GaN was explained, and is a good reference for the present research into the ELO GaN on diamond stripe stress mapping. In addition to stress comparison at coalescence, wings, and window regions, work has been reported comparing the crystal quality of the GaN layer in these regions on the sample. Kuball et.al. has shown that ELO GaN over sapphire has a compressive stress of 0.07 GPa at the coalescence boundary with respect to the wings. According to their study, the crystal structure and stress distribution at the wings and at the window region are different and much better GaN quality (low defect density) is observed at the wing region after ELO GaN. The quality of the GaN layer over the diamond stripes is very good as compared to nondiamond region because threading dislocations that

occur during epitaxial GaN growth do not propagate so the diamond stripes may effectively act as a barrier for these dislocations in the GaN layer.

1.3 Raman Stress Mapping in Epitaxial Lateral Overgrown GaN

Raman spectroscopy is a non-destructive, highly sensitive, and reliable method for stress measurement. If the material is under stress, changes in the phonon frequency will occur that allows the estimation of stress in the ELO GaN. Ahmed et.al. [9], estimated the amount of stress on the selectively deposited diamond stripes over a silicon wafer. They observed a high compressive stress of 0.84 GPa at the center of the diamond stripes and a relatively low tensile stress of 0.14 GPa in the Si substrate close to the diamond stripe and silicon substrate interface. Clearly, the data indicate that ELO GaN above the diamond stripes has a stress distribution. Kozawa et.al. [10] have studied the thermal stress in ELO GaN over a sapphire substrate with an AlN intermediate layer. They found a biaxial compressive stress in the GaN layer due to the difference in CTE. Kozawa et.al. also used Raman spectroscopy to quantify the stress in their samples and observed a broadening and shifting of the E_2 phonon GaN peak as a result of this stress.

A unique stress distribution is expected for both the diamond stripes and the ELO GaN layer due to the different CTE, different lattice constants and different growth mechanisms of GaN over diamond stripe and expect this to be clarified through this experimentation.

The research samples have diamond stripes of different dimensions (1, 2, 5, and 10 μm) and different spacing (1:1, 1:2, 1:3) as shown above in Figure 1. After careful investigation of the stress using Raman spectroscopy, the dependence of stress on the geometrical structure will be determined. Stress mapping of ELO GaN grown over diamond stripes without an intermediate layer has not been investigated, to date. This stress mapping will advance the scientific understanding of the formation and distribution of stress on these microstructures and aid in

developing a deeper understanding of the quality of the bonding between GaN and diamond using the ELO method. Insight into the dependence of ELO GaN thickness on stress will also be developed. Finally, the thermal stress is dependent on the growth environment (especially growth temperature), so this study will also aid in understanding the impact of the MOCVD and CVD growth environments on the overall stress distribution.

2. MOTIVATION FOR THE RESEARCH

Integration of CVD Diamond with AlGaN/GaN HEMT structures has been studied extensively. However, due to the roughness of the diamond surface, large thermal mismatch, and need for a protective layer over the HEMT structure during diamond growth, integration of diamond has been limited to a few research results. The deposition of GaN directly over Diamond was realized for the first time in our group, by Ahmed et.al. [1], via a technique for growing GaN over the diamond stripes without the addition of a barrier layer. The GaN growth was epitaxial and lateral, making the direct integration of GaN over diamond possible with a comparatively better interface and GaN quality than other methods that includes an interfacial layer. This technique is expected to improve thermal management of the AlGaN/GaN HEMT as there is no "extra" barrier layer decreasing the thermal boundary conductance. Characterizing this GaN-diamond structure is critical as it helps to determine whether eliminating this intermediate layer is beneficial and whether this structure should be modified to improve performance, in order to facilitate commercialization.

This is the first ever sample of GaN grown directly over diamond, although people have developed ELO GaN over other substrates (e.g. ELO GaN grown over sapphire stripes [10]). Since thermal stress in these microstructures is related to the interface materials and their growth conditions, different stress distributions than other previously studied ELO GaN samples are anticipated. The thesis is that the different CTE for GaN and diamond, and their high growth temperature in MOCVD and CVD are controlling factors for thermal stress in the sample.

The stress distribution in diamond stripes of different dimensions and different separations after ELO GaN is necessary to understand the effect of ELO GaN on these diamond structures. Finally, the stress determined from both experiment and modelling will provide insight about

how diamond stripe size and spacing as well as the thickness of the overgrown ELO GaN influence diamond stripe and ELO GaN stress. These calculations will help guide structural modifications that minimize stress to increase the lifespan and device performance of diamond integrated GaN HEMT devices.

3. CRYSTAL STRUCTURE AND THEIR PROPERTIES

3.1 Gallium Nitride (GaN)

GaN is a member of group III nitride semiconductors which have large band gap, high breakdown field, and good electron transport properties (electron velocity and peak velocity). The availability of thin heterostructure (AlGaN/GaN) epitaxial layers with comparatively high growth rate either from Hydride Vapor Phase Epitaxy (HVPE) or by Metal Organic Chemical Vapor Deposition (MOCVD) makes GaN a promising commercial material for high power and high frequency electronic devices.

GaN may crystallize in the wurtzite or cubic zinc blend structure but hexagonal wurtzite is the most thermodynamically stable form. The wurtzite lattice structure is described by three lattice parameters a, c and u which represent the length of the hexagonal side, height of the crystal lattice and bond length between Gallium and Nitrogen, respectively. Typical properties of wurtzite GaN and zinc blend GaN is summarized in Table 1 below [11]:

Table 1 Basic properties of Gallium Nitride.

	Wurtzite (Hexagonal)	Zinc blend (Cubic)	Unit
Density	6.15		$g\ cm^{-3}$
Band gap (E_g)	3.39	3.2-3.3	eV (at 300K)
Temperature dependence(dE_g/dT)	-6		10^{-4} eV K^{-1}
Pressure dependence(dE_g/dP)	4.2		10^{-3} eV $kbar^{-1}$
Lattice constant	a=3.189 c=5.185	a=4.52	10^{-8} cm 10^{-8} cm
CTE	$\Delta a/a$=5.59 $\Delta c/c$=3.17		10^{-6} K^{-1} 10^{-6} K^{-1}
Deformational potential	8.3		eV
Thermal conductivity	1.3		W cm^{-1} K^{-1}
Refractive index	2.33(at 1 eV) 2.67(at 3.38 eV)	2.9 (3 eV)	
Dielectric constant	$\varepsilon\infty$=5.35 ε_o=8.9-9.5		
Electron effective mass	0.2		m_o
Electron saturation velocity	2.5		10^7 cm s^{-1}
Break down field	>5		10^6 cm s^{-1}

3.2 Diamond

Diamond cubic is the crystal structure of diamond and can be visualized as two interpenetrating FCC lattices with tetrahedrally bonded carbon atoms as shown in Figure 2. Valence shell electrons are shared by four different carbon atoms resulting in a tetrahedral structure with sp^3 hybridization. Diamond is the sp^3 bonded form of carbon which forms a strongly bonded lattice thereby making diamond hard compared to sp^2 bonded graphite. Graphite is the stable form of carbon at room temperature and pressure wherein the sp^2 hybridization yields a sigma and pi bond network with the neighboring carbon atoms producing a sheet-like structure that is relatively soft. The lattice constant of diamond is 3.57 Å.

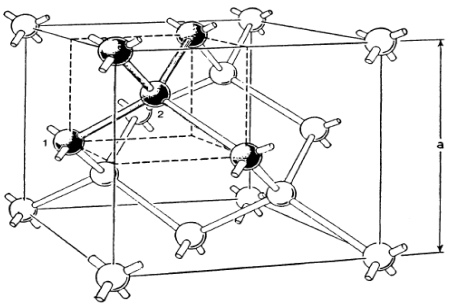

Figure 2: Diamond crystal structure showing tetrahedral coordination with interatomic bonding (e.g., between 1 and 2). [12]

Chemical Vapor Deposited (CVD) diamond is one of the most promising research materials as it has extremely high thermal conductivity, typically five times that of copper at room temperature [13]. The underlying mechanism of thermal conduction in diamond is quite different from metals because conductivity in metal is due to the electrons, while in diamond it is due to phonon transport. (The quanta of lattice vibrations (phonons) generated due to the available heat energy [13].) Although diamond has the highest thermal conductivity of any material, the presence of impurity atoms and crystalline defects can significantly decrease the

thermal conductivity and the higher the impurity / defect concentration the greater will be the scattering of phonons and, consequently, the thermal conductivity will be lower [13].

Another important factor is temperature of the material. Up to about 110 K, the thermal conductivity will increase as phonon velocity increases but above this temperature the thermal conductivity begins to decrease due to the decrease in mean free path. Electronic and optical properties of diamond are also noteworthy as it has an indirect band gap of 5.47 eV at 300K and high electron and hole mobilities of 2500 $cm^2V^{-1}s^{-1}$ and 1200 $cm^2V^{-1}s^{-1}$, respectively, high carrier saturation drift velocity 2.7×10^7cm s^{-1}, high electric breakdown field 10^7 Vcm^{-1}, small dielectric constant 5.7, and high surface acoustic wave velocity 1.2×10^4 m s^{-1}. These electronic properties are a function of intrinsic defects and/or extrinsic dopants such as Nitrogen, Phosphorous, Silicon, and Boron [14]. Diamond shows semiconductor properties even at high temperatures (500º C or higher) due to wide bandgap, while for example silicon and GaAs preserve semiconductor properties only up to 150 ºC and 250 ºC, respectively [13].

3.3 Lattice Vibration

Analogous to a photon of an electromagnetic wave the quanta of atomic vibration which obey the Bose Einstein (BE) statistics is termed a phonon. Since lattice vibration can be assumed as a mass spring system a second order differential equation can be used to solve for the one-dimensional lattice vibration. By assuming a plane wave solution, two solutions of second order differential equations are obtained. For the detailed mathematical derivation please refer to [15].

The general solution of one dimensional lattice vibration can be written as [15],

$$\omega^2 = \frac{2C(m_1 + m_2) \pm \sqrt{4C^2(m_1 + m_2)^2 - 4m_1m_2C^2K^2a^2}}{2m_1m_2} \quad (1)$$

Where C is the force constant, m_1 and m_2 are masses, a is the distance between two similar lattices (m_1 to m_1 or m_2 to m_2) and K is the wave vector which is inversely related with the wavelength.

For small K i.e. K << 1,

$$\omega_1{}^2 = \frac{\frac{1}{2}C}{m_1 + m_2}K^2a^2, \text{This is acoustic branch} \quad (2)$$

$$\omega_2{}^2 = 2C(\frac{(m_1 + m_2)}{m_1 m_2}) = 2C(\frac{1}{m_1} + \frac{1}{m_2}), \text{This is optical branch} \quad (3)$$

At the zone boundary K = ± π/a and the solution is, thus,

$$\omega^4 m_1 m_2 - 2C(m_1 + m_2)\omega^2 + 4C^2 = 0 \quad (4)$$

$$\omega^4 - 2C(\frac{1}{m_2} + \frac{1}{m_1})\omega^2 + \frac{4C^1}{m_1 m_2} = 0 \quad (5)$$

$\omega_1{}^2 = \frac{2C}{m_1}$(Acoustic Branch) , and $\omega_2{}^2 = \frac{2C}{m_2}$(Optical Branch)

If $m_1 > m_2$ then $\omega_1{}^2 < \omega_2{}^2$ and this yields the plot of ω(K) in the first Brillion zone as shown in Figure 3.

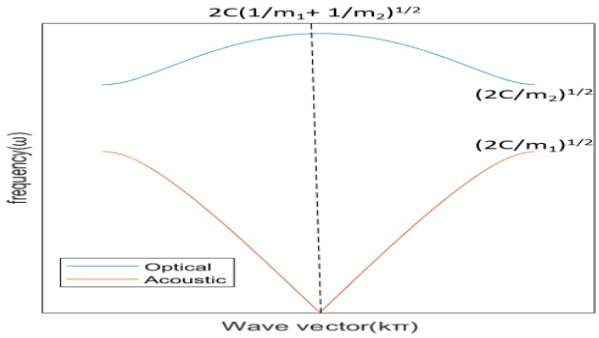

Figure 3: The optical and acoustic phonon modes in a diatomic linear solid.

The wavelike solution does not exist for certain frequencies which is the characteristic feature of an elastic wave in polyatomic lattices. Here the wavelike solution does not exist between ω_1 and ω_2. For optical branch on substituting the value of ω^2 into above equation, a relation to describe the motion of atoms (in the optical branch) is obtained [15],

$$\frac{u}{v} = -\frac{m_2}{m_1} \tag{6}$$

This equation indicates that the motion of atoms in the optical branch moves against each other keeping the center of mass fixed. An electromagnetic wave can excite this type of motion if atoms are oppositely charged. Unlike the optical branch, the motion of atoms in the acoustic branch moves in same phase as the acoustic waves in gases for long wavelength limit (K = 0).

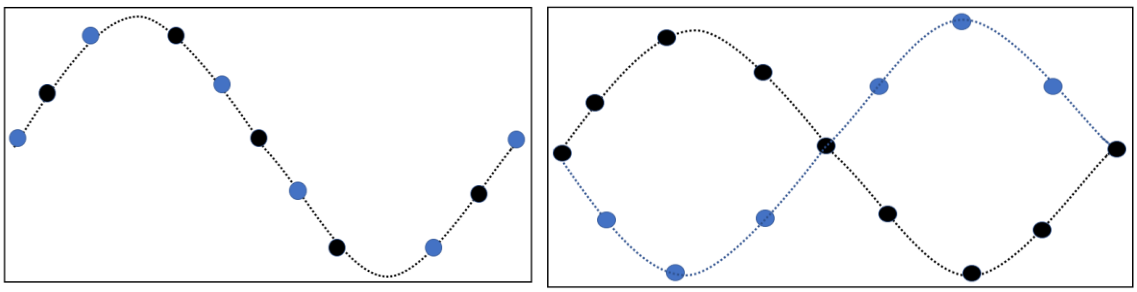

Figure 4: Showing lattice vibration in acoustic and optical mode, blue and black sphere representing atoms of opposite charges.

The degree of freedom is an important factor to determine the number of acoustic and optical branches in the crystal lattice. If N primitive cells has p number of atoms then the total number of atoms will be pN and each atom has three degree of freedom along x, y and z direction giving the total degrees of freedom for the crystal as 3pN. In one Brillion zone having N primitive cells the total number of allowed K values in a single branch is N. Hence the acoustic branches (LA and two TA branches) have 3N modes accounting for 3N degrees of freedom. Furthermore, the number of optical branches present in that crystal is 3Np-3N [15]. The atomic displacement of phonons is said to be the longitudinal mode if the wave vector of phonons and atomic vibration are in the same direction whereas the atomic vibration and wave vector of phonons are perpendicular for the transverse mode.

4. THE RAMAN EFFECT

4.1 Theory of Raman Spectroscopy

Raman Spectroscopy is one of the most powerful techniques for material characterization as it can provide local temperature, stress, and strain distribution, doping concentration, and the chemical nature of the material. In addition to this, it is non-destructive which is beneficial for material characterization. The classical and quantum mechanical explanations of Raman Spectroscopy are presented in the following sections in order to provide background knowledge of the working principles.

4.1.1 Classical Explanation of Raman Spectroscopy

When light is incident on a medium it gets polarized, so by the basic principle of electrodynamics, the polarization can be quantified as [16],

$$P = \varepsilon_0 \lambda E \tag{7}$$

Where P is polarization, ε_0 is permittivity of free space, χ is susceptibility tensor which is a function of position and frequency, and E is the electric field incident on the medium. Since susceptibility is position dependent, it can be expanded in terms of general coordinates. Finally, substituting the time dependent general coordinate to get the time dependent susceptibility yields the time dependent polarization as below. For a detailed mathematical derivation please refer to [17].

$$P(t)=\varepsilon_0(\lambda_{j1})_0 E_0 \mathrm{Cos}(\omega_I t) + \sum_s (\frac{\partial \lambda_{j1}}{\partial Q_s})_0 Q_s^0 E_0 \frac{1}{2}\{\mathrm{Cos}((\omega_I + \omega_s)t) + \mathrm{Cos}((\omega_I - \omega_s)t)\} \tag{8}$$

The first term of the above polarization expression represents the elastic scattering of light while the second term is the indicator of inelastic scattering of light. More precisely, the second term is the indicator of stokes and anti-stokes scattering events. The stokes component has lower frequency while anti-stokes has higher frequency by a factor $\pm\omega_s$, compared to the incident light frequency as shown in the above equation.

4.1.2 Quantum Mechanical Explanation of Raman Spectroscopy

Consider a system of an electron, photon and phonon, then the Hamiltonian of said system can be expressed as [17],

$$H = \hat{H}_e + \hat{H}_F + \hat{H}_L + \hat{H}_{eF} + \hat{H}_{eL} \tag{9}$$

Where, $\hat{H}_e$ is the electron Hamiltonian, $\hat{H}_F$ is the photon Hamiltonian, $\hat{H}_L$ is crystal lattice vibration Hamiltonian, $\hat{H}_{eF}$ is the Hamiltonian due to interaction of electron and photon while $\hat{H}_{eL}$ is another Hamiltonian which corresponds to the interaction of electron and phonon. The sum of the last two terms of the equation can be defined as the perturbation term and can be denoted as $\hat{H}_{int}$, which is the cause of electronic transition in this system.

Quantum mechanically, the transition of the electron per unit time from its initial state (i) to final state (f) can be well explained by time dependent perturbation theory.

$$W_{if} = \frac{2\pi}{\hbar}|K_{fi}|^2\delta(E_i - E_f) \tag{10}$$

The above equation is also called Fermi Golden rule and $|K_{fi}|^2$ is the matrix element representing the transition from initial state i to final state f. The nature of the matrix element is directly dependent on the type of scattering that occurs in the electron, photon, and phonon system. The first mode of interaction could be just inelastic scattering between electron and photon, the second mode is photon scattering by emission or absorption of one phonon and the third mode

is two phonons emission Raman scattering. The number of phonons involved in the scattering process is an indicator of the order of the perturbation process. If n phonons are involved, then n+2 order of perturbation processes will describe the phenomenon. Since no phonon need be involved in the electron photon interaction, a second order time dependent perturbation will describe the Raman scattering phenomenon and the corresponding matrix element can be written. Based on the involvement of photon, electron and/or phonon the matrix element will be different. Obviously for different matrix element the transition probability will be different which ultimately gives the corresponding scattering cross section. For detail mathematical derivation about the quantum mechanical Raman effect please refer to[17],

Thus, the final equation for scattering cross section is,

$$d\sigma(k_i\alpha_i;\omega_f\hat{\vartheta}\alpha_f) = \frac{2\pi}{\hbar v_g}\frac{n^3(\hbar\omega_f)^2 d(\hbar\omega_f)d\Omega}{(2\pi)^3 c^3\hbar^3}\sum_{E_iE_f}|K_{\omega_f}E_f;\omega_iE_i|^2\,(\hbar\omega_i + E_i - E_f)^2 \qquad (11)$$

Where $\sum_{E_iE_f} is$ restricted as, $\hbar\omega_f < \hbar\omega_i + E_i - E_f < \hbar(\omega_f + d\omega_f)$. Moreover, considering the polarization effect is very interesting as its effect on Raman spectroscopy can reveal the orientation and symmetry of the vibrational modes in a crystal. In this setup, the plane polarized light from the polarizer incident on the sample and light scattered from the sample is again incident on a second polarizer (analyzer), before entering the detector. The analyzer can be oriented perpendicular or parallel to the incident laser plane to get corresponding intensity. The polarizability of vibrational modes is not equal along and across bonds, so one would observe different intensities based on the polarization direction of the laser beam and the difference in intensity is key in determining crystal orientation. Also, if the vibrational modes in a material are

symmetric, then the polarization of the scattered laser light will be the same as the incident laser light, otherwise the scattered light will lose polarization fully or partially.

4.1.3 Confocal Raman Microscopy

The confocal microscope creates a sharper specimen image in comparison with the conventional microscope because this system can avoid the light coming from non-focal planes. Since only light coming from the exact focal plane creates the image there is less haze, better contrast, and the image represents a very thin slice of the specimen.

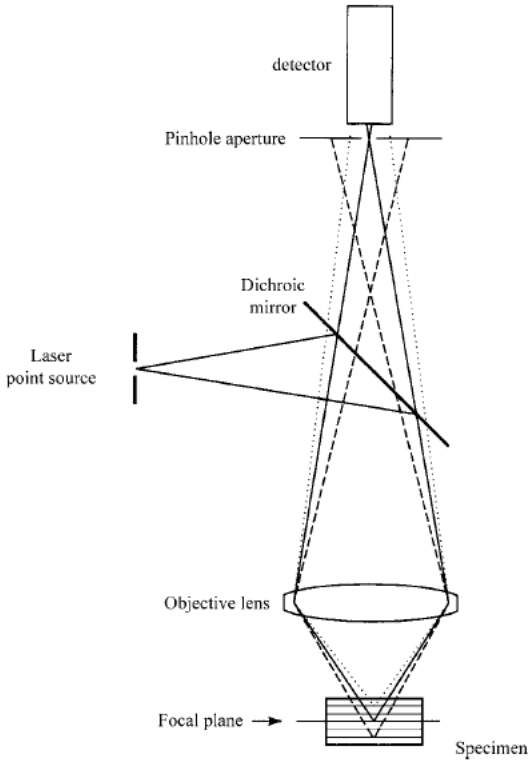

Figure 5: Basic principle of confocal microscope [18].

As shown in the schematic diagram in Figure 5 the laser point source is incident on the dichroic mirror which directs the light towards the specimen through the condenser. The condenser also acts as objective lens to collect the reflected rays from the specimen. A pinhole aperture is placed

near the detector which is very important to selectively allow only the reflected light to enter a photodetector. The position and size of the pinhole aperture is designed to allow the rays of light reflected from the focal plane and reject all other light. This setup generates a very sharp point image with increasing microscope resolution.

Another important factor is resolution which is strongly dependent upon the size of the Airy disc formed on the focal plane. Theoretically, the image is assumed to be a point on the focal plane but in practice it forms an image pattern with a certain radius which is the Airy disc. The minimum distance between two neighboring Airy discs determines the resolution. According to the Rayleigh criterion the minimum distance between two Airy discs to get a completely resolved image should be equal to the radius of the Airy disc. These criteria essentially indicate the minimum of one Airy disc superimposed to the maximum of another Airy disc and vice versa. Mathematically, the size of the Airy disc is dependent on the wavelength of the laser and numerical aperture of the lens. The resolution is directly proportional to the wavelength of the light used and inversely proportional to the numerical aperture of the objective lens used in the microscope. Hence to get the best resolution a small wavelength laser and high resolution objective lens is required:

$$Resolution = \frac{0.61\lambda}{NA} \tag{12}$$

Where, λ is the wavelength of light and NA is the numerical aperture of the lens. For light of wavelength 532 nm and 100X objective lens of NA 0.9, the lateral resolution of the confocal lens used in the present studies will be ~0.360 μm. Furthermore, the axial resolution of the Texas State LABRAM HR Evolution system is ≤ 2 μm with objective of 100X (NA=0.9) and confocal hole set at 100 μm.

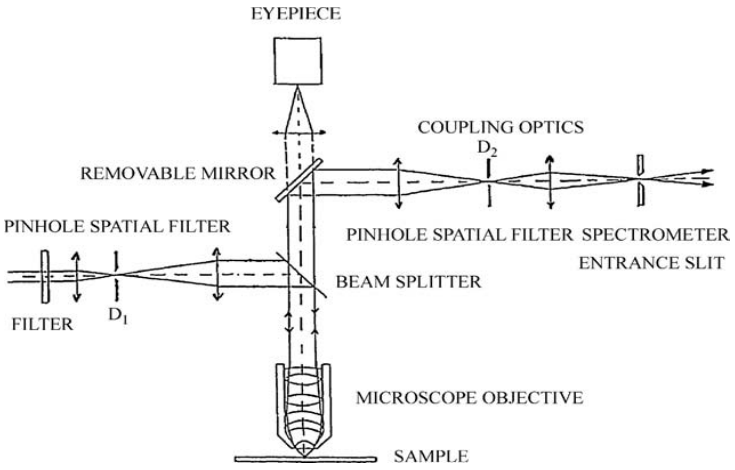

Figure 6: Schematic diagram of Raman confocal optical microscope showing a pinhole spatial filter which consist of pinhole confocal diagram D_1 and D_2 [18].

Figure 6 shows a schematic confocal microscope system that is used in the Raman system. The basic idea of the confocal is the same as presented in Figure 5. The laser from the source passes through filters to make it monochromatic and then through the pinhole spatial filter to obtain the clean point laser beam by removing all the diffraction rings and speckle noise from around the focus spot. The laser light reflected from the sample again passes through the pinhole spatial filter before entering the photodetector to remove the stray light coming out of the focus plane. Besides these confocal properties the microscope used in the Raman system should focus on a very small area unlike the normal microscope which focuses on a broad region of the specimen. As before, the numerical aperture of the lens should be comparatively higher to improve the resolution of the system.

4.1.4 Raman Properties of GaN

GaN crystallizes in both the wurtzite (hexagonal) and zinc blend (cubic) structures, but wurtzite is more stable. Wurtzite GaN is a direct transition semiconductor and has received significant attention for a variety of applications [19, 20]. More importantly, GaN shows an electron saturation velocity 2 to 3 times that of Si (~$1X10^7$ cm s^{-1}) and a critical breakdown field several

times higher than Si (~$3X10^5$ V s^{-1}) [21] which makes the use of GaN in high power and high frequency devices highly desirable.

Raman spectroscopy is nondestructive, contactless, needs no special attention for sample preparation, and relies on the modulation of electronic polarizability induced by various elementary excitations in solids such as phonons and plasmons. Furthermore, Raman spectroscopy can be used to determine lattice properties, electronic properties and magnetic properties of the material with a lateral resolution ~1 μm or less. Raman scattering is most useful for covalent crystals (compared with ionic crystals) because the fluctuation of polarizability induced by lattice vibrations is high and the valence electrons are less localized. GaN is suitable for Raman scattering as the chemical bond is a mixture of covalent and ionic bonding.

GaN crystallize in the hexagonal (space group C^4_{6v}) or cubic structure (space group T_d^2). In the hexagonal structure, the primitive cell contains two Ga-N atom pairs, but the cubic structure contains only one atom pair. The Ga atom is tetrahedrally surrounded by N atoms and vice versa in both types of crystal structure. The first order phonon Raman scattering is caused by phonons with wavevector K~0 (i.e. at Γ point) following momentum conservation. From group theory the hexagonal structure should have eight sets of phonon normal modes at the Γ point, $2A_1+2E_1+2B_1+2E_2$. One set of A_1 and E_1 are acoustic while the rest are optical which are shown in Figure 7. A_1 and E_1 are both Raman and infrared (IR) active, E_2 is Raman active while B_1 is neither Raman nor IR active. Hence, B_1 is also called a silent mode. The atomic displacement scheme of these optical modes is also shown in Figure 7. As shown in the figure, the A_1 and B_1 modes are due to the atomic displacement along the c direction while the rest are due to the atomic displacement perpendicular to the c axis.

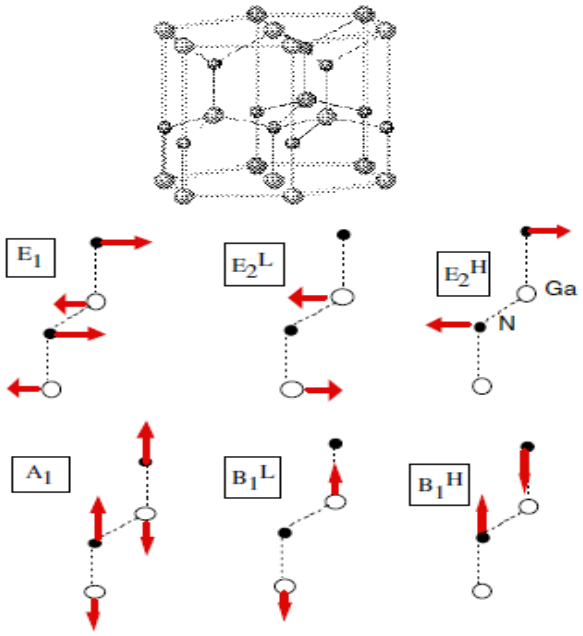

Figure 7: Optical phonon modes in the wurtzite structures[11]

The Raman scattering efficiency with polarization detection is given by ref. [8],

$$S = |e_L \, R \, e_s|2 \tag{13}$$

Where e_L and e_s are denoting the polarization for the incident and scattered light while R is the Raman stress tensor of the scattering process. For the wurtzite crystal the Raman stress tensor has diagonal components for the A_1 modes and both diagonal and off diagonal modes for the E_2 modes and only off diagonal components for the E_1 modes [8]. From this stress tensor it is concluded that A_1 modes are visible when the incident and scattered lights have parallel polarization while the E_1 mode is observed only in cross polarization geometry. The selection rule for the zinc blend GaN crystal is simple, comparatively. With no polarization detection, only the LO phonon is observed from the (100) plane while only the TO phonon is observed from the (110) plane while both TO and LO are simultaneously observed from backscattering from the (111) plane [8]. The hexagonal wurtzite GaN has $A_1(z)$, $2B_1$, $E_1(x,y)$ and $2E_2$ optical modes at the

Γ point of the Brillion zone which was explained in Section 4.1.3 [22]. Based on group theory selection rules, B_1 is not active in any Raman scattering experiment configuration. The other four modes are Raman active, at least in one of the configurations, which is summarized in Table 2 where the z axis is the axis parallel to the GaN c-axis while x and y are perpendicular to it [23].

Table 2. All possible Raman modes in different configurations.

Configuration	**Allowed modes**
Z(X--) $\bar{Z}$	A_1(LO), E_2
X(Y--) $\bar{X}$	A_1(TO), E_1(TO), E_2
X(Z--) $\bar{X}$	A_1(TO), E_1(TO)

Based on the table above if the Raman scattering experiment is conducted along the backscattered z direction, A_1(LO), E_2(LO) and E_2(TO) Raman modes are expected. Since A_1(z) and E_1(x,y) are polar modes polarized along the z optical axis and in the basal (x,y) plane, each of them breaks into LO and TO phonons modes. Breaking of the above-mentioned symmetry rule in Raman scattering experiments happens either if the incident laser light is not perfectly parallel to the c axis or the c axis is tilted by some angle during lateral overgrowth. Some peaks which are forbidden by the symmetry rule may also appear weakly on backscattering geometry because the incident laser light may not be perfectly aligned with the desired direction of that crystal scattering geometry. This effect is called symmetry breaking or relaxation of Raman selection rule. Since the TO-LO splitting (180-200 cm^{-1}) is much larger than A_1-E_1 splitting (7-30 cm^{-1}), long range electrostatic force dominates over the crystalline anisotropy[24]. Hence, mixing of A_1 and E_1 modes easily happens if the incident laser (phonon propagation direction) is not perfectly

aligned with the optical axes resulting in forbidden weak Raman modes as quasi TO or quasi LO modes breaking the symmetry rule.

$$\omega_Q^2(\mathrm{TO}) = \omega^2(\mathrm{E_1(TO)})\,\mathrm{Cos}^2\theta + \omega^2(\mathrm{A_1(TO)})\,\mathrm{Sin}^2\theta \qquad (14)$$

$$\omega_Q^2(\mathrm{LO}) = \omega^2(\mathrm{A_1(LO)})\,\mathrm{Cos}^2\theta + \omega^2(\mathrm{E_1(LO)})\,\mathrm{Sin}^2\theta \qquad (15)$$

Here θ is the angle between c axis and phonon propagation direction. The above equations show the appearance of quasi LO and TO modes with slightly different phonon frequency depending upon the angle θ.

If the GaN crystal is of high quality, there is the possibility of observing precise second order Raman modes. Basically, for the second order phonon scattering the momentum conservation rule demands that the sum of the two phonon wave vectors participating in Raman scattering should be zero.

$$k_1 + k_2 \sim 0 \qquad (16)$$

Thus, for second order Raman scattering phonon modes are not restricted on the Γ point but They will extend to the whole Brillion zone. Hence, second order phonon Raman spectra helps to estimate the density of states and can be regarded as the critical test of the calculated phonon dispersion curve. From the group theory analysis of the GaN spectrum the acoustic overtones appear at 300-420 cm^{-1}, the acoustic-optical combination at 850-1000 cm^{-1} and optical overtones and combination modes at 1150-1500 cm^{-1} [25].

4.1.5 Defects and Impurity Raman Modes

Not only the host lattice but also impurities present in the crystal can be detected by the Raman scattering phenomenon. If the impurity atom replaces the comparatively heavier atom from the host lattice, then the lattice vibration can be localized within a small lattice space and this mode

of lattice vibration is called the Localized Vibrational Mode (LVM). Basically, a small vibrating object between two large objects cannot set the large objects in motion so vibrations of the small object cannot propagate globally but remains within the small region. A similar scheme is observed if the semiconductor is doped by an atom having small atomic weight. The small impurity is sandwiched between two large host lattice atoms so the lattice vibration of the large atom cannot spread over the whole lattice but localized in a small area showing some Raman modes in the energy gap between the acoustic and optical branches of the phonons or above the optical branches. The frequency and polarization properties of the LVM are very sensitive to the impurities and neighbor atoms so LVM gives information about the geometry and impurity species. Vibration between the solid atoms can be imagined in such a way that they are connected by a spring. The LVM frequency and localization of the LVM modes are inversely proportional to the mass of impurity. The vibration of the atom due to incident light can be mathematically formulated by assuming a newly doped atom has mass $m_{imp,}$ effective charge q, doping constant of the medium Γ and vibrating frequency ω_{LVM}. The vibrational motion of the impurity atom can be formulated by assuming simple mass spring system as [26],

$$m_{imp}\ddot{x} = -k_{imp}x \tag{17}$$

And,

$$\omega_{LVM} = \sqrt{(\frac{k_{imp}}{m_{imp}})} \tag{18}$$

Where k_{imp} is the spring constant, m_{imp} is the mass of impurity atom and ω_{LVM} is the frequency of the LVM. A slight modification in the above equation arises considering the vibration of nearest neighbor atoms. This is more realistic as the center of mass of whole system remains constant. The modified equation will be of the form [27],

$$\omega_{LVM} = \sqrt{k_{imp}(\frac{1}{m_{imp}} + \frac{1}{\chi m_{nn}})} \quad (19)$$

Where k is the spring constant, χ is a parameter that depends upon the local angle bending and bond stretching force constant of vibrational mode and m_{nn} is the mass of the host atom. This equation shows that with the replacement of a heavy element with a lighter element, the localized vibrational mode frequency increases.

Also, the intensity of the LVM mode is related with the doping concentration as [24]

$$I_{LVM} \sim \text{Dopant concentration} \times V \times \sigma \quad (20)$$

Where V represents the scattering volume and σ represents the scattering cross section per impurity atom. Thus, this equation shows that with an increase in dopant concentration the intensity of the LVM increases for constant scattering volume and scattering cross section.

5. SAMPLE GROWTH AND CHARACTERIZATION METHODOLOGY

Thin film growth is a crucial process for realizing modern electronic and photonic devices with desired properties and dimensions. To properly understand the growth mechanisms, one must know about the kinetics and thermodynamics of the entire process. This section briefly discusses heteroepitaxial nucleation and growth mechanisms of thin films.

Optimizing structures for use in practical applications can only be achieved through careful characterization, typically by a variety of techniques. Raman spectroscopy provides meaningful information regarding the nature of the stress distribution, bonding between GaN and diamond, and the quality of the overgrown GaN in various regions of interest (coalescence, wing, and window) in the samples. These results will help determine the direction of future work on the GaN-Diamond structure.

5.1 Chemical Vapor Deposition of Diamond

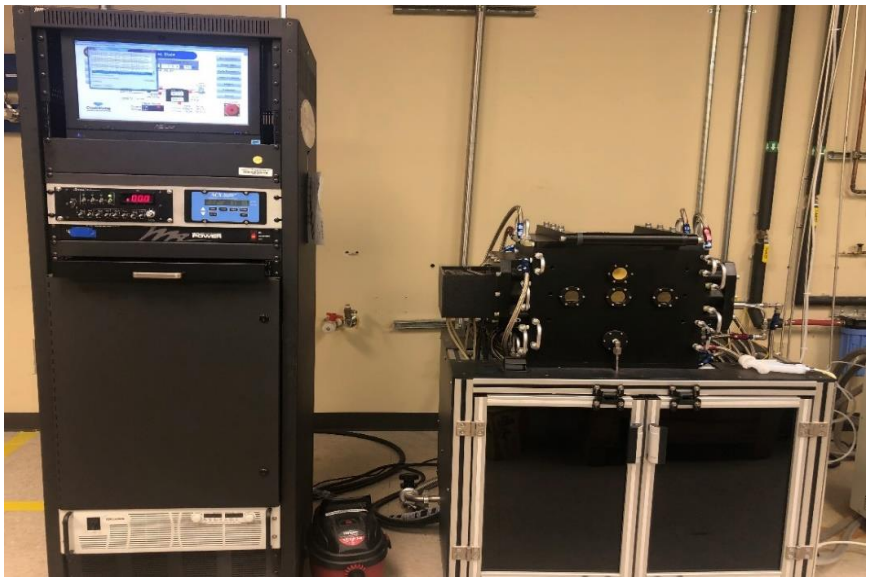

Figure 8: Texas State CVD System

Diamond growth by CVD has attracted the attention of the scientific community since 1980. In this method the carbon containing molecules are dissociated into active neutral radical (alkyl radical e.g.: methyl radical) and molecular hydrogen is converted into atomic hydrogen in the vapor phase which results in diamond deposition over the surface either homoepitaxially or heteroepitaxially. The hot filament (HF) CVD system at Texas State University used to grow the patterned diamond structures of different dimensions in the studied sample is shown in Figure 8. The typical nucleation method uses diamond seed to coat the substrate for subsequent diamond growth. From the seed the diamond grows three-dimensionally until it forms the polycrystalline diamond layer over the substrate. The seeding process will be discussed later, in the section 5.1.5.

The precursor molecules (hydrocarbon-based) and excess hydrogen should be at high temperature, between 1000-1400 K and high pressure which will maintain the optimal growth rate and quality of the diamond film. At temperatures above 1400 K, graphitic carbon deposition is favored while at temperatures below 1000 K, diamond like carbon (DLC) deposition tends to form. [28] The quality of the diamond film is indicated by the ratio of sp^3 to sp^2 carbon. To achieve the best quality diamond, the hydrogen is extremely important as it generally triggers the formation of sp^3, which can be explained by the fact replacing any two neighboring carbon atoms along a tetrahedral hydrocarbon chain by hydrogen atoms, the tetrahedral (sp^3) structure will remain preserved. Furthermore, the etching of graphite by hydrogen is more favorable, compared with diamond etching, and the atomic hydrogen thereby promotes the heteroepitaxial growth of the diamond film [15]. Based on the activation of the precursor molecules for the nucleation and growth of diamond, various methods have been developed, as discussed below:

5.1.1 Hot Filament CVD

Metals having a high melting temperature, like tungsten, have been used for the activation of the precursor methane molecule near the substrate. Typical pressures range between 10-100 torr, and substrate and filament temperatures are between 700−1000 ºC and 2000−2300 ºC, respectively. These conditions are favorable for dissociation of hydrogen and the formation of alkyl radicals just above the substrate so formation of diamond film will be enhanced. Carburization is the consumption of carbon from methane by the tungsten filament at high temperature and is responsible for the early low rate of nucleation and growth of diamond film. Also, the electrical resistance of the filament must be monitored to maintain a constant filament temperature by adjusting the current and voltage according to the resistant change during carburization. With its comparatively low temperature this process produces a smaller concentration of atomic hydrogen and, hence, the rate of diamond deposition is low [15]. This can be improved by plasma enhanced CVD.

5.1.2 Plasma Enhanced CVD

In plasma enhanced (PE) CVD, the plasma generated by induction heating or electric discharge is used to decompose the carbon containing precursor molecule and hydrogen. Although the binding energy of molecular hydrogen is 4.5 eV, most of the hydrogen dissociation is at 9.5 eV, so the atomic hydrogen produced in plasma enhanced methods has greater kinetic energy as compared to that of HFCVD. This is the reason why diamond film grown by PECVD has a higher growth rate [15].

Approximately 1 % of the molecules in a plasma are converted into neutral radicals while 0.01 % are converted to ions. Neutral molecules have high Gibbs free energy during their decomposition so molecule like CH_4 do not participate in the growth of diamond. Thus, the growth rate of diamond is determined mainly by the concentration of neutral radicals. The

effect of ionized radicals is not clear. Although their contribution to the growth rate is minimal, one cannot rule out ion-assisted processes. For example, Stoner et. al [18] reported an enhancement in the diamond nucleation density by microwave-plasma-assisted CVD on a negatively biased silicon substrate.

The plasma pressure is another important factor for PECVD. Even though the kinetic energy of an electron is high at low pressure, the transfer of energy from an electron to a molecule is lower compared to that at high pressure. The reason behind this is the relatively greater mean free path at low pressure then at high pressure. Hence, temperature of the high-pressure system needs to be high because less energy is lost over the small mean free path. Therefore, a system at high plasma pressure has higher temperature so the concentration of neutral radicals and atomic hydrogen is maximum which corresponds to the high deposition rate at high pressure. Plasma discharge at higher frequency, 2.45 GHz, produces a higher plasma density with higher electron energy (RF discharge at 13.5 MHz) and thereby produces a greater concentration of atomic hydrogen and neutral radicals. Finally, ideally, the plasma is confined to the center of the deposition chamber and in the form of a ball to reduce the possibility of diamond deposition on the walls of the chamber [15]. Being electrodeless, PECVD is free from filament contamination that occurs with HFCVD.

5.1.3 Combustion Flame Assisted CVD

Simple experimental design, low cost and high growth rate are the advantageous features of this method. A combustion flame generated from an oxygen-acetylene brazing torch at atmospheric pressure is used to grow diamond. The ratio of oxygen and acetylene is important for diamond deposition. Diamond will be deposited only when the ratio is between 0.70 to 0.98. A flame produced within this range is called an acetylene flame. The oxygen flame (ratio greater than 1)

and neutral flame (ratio equal to 1) do not yield thin film diamond deposition [29]. The mechanisms for diamond deposition are similar to the above mentioned methods.

5.1.4 DC Plasma Jet CVD

Extremely fast growth rate, 1 mm/hr., may be obtained at the high-pressure plasma discharge via conventional transport processes [17]. Hydrogen and methane gas used in this process obtain thermal and electrical energy by an electric discharge at temperatures between 1000-1500 K causing these gases to dissociate to form precursor molecules for diamond deposition. One of the important features of this process, besides very high growth rate, is that diamond and other materials (such as ceramics and metals) can be deposited simultaneously. Formation of different intermediate metal carbide layers is possible creating a functional gradient which reduces thermal stress and, hence, the adhesion strength of the diamond film over the substrate increases by several orders of magnitude [30].

5.1.5 Nucleation and growth of thin films

The phase change from supersaturated vapor to solid that occurs during the chemical vapor deposition process is termed nucleation - an important phenomenon which determines the fate of the diamond grain structure because what happens during the nucleation and growth processes is of great importance to determine the nature of the diamond thin film.

The nucleation rate, or the number of stable nuclei forming per unit volume per unit time, is influenced by the gas to solid transformation which decreases the free energy of the system. The decrease of the free energy is given by [31],

$$\Delta G = \frac{4\ \pi r^3 \Delta G_v}{3} \tag{21}$$

Where ΔG is the decrease in free energy per unit volume.

Nucleation will be continuous if $P_s > P_v$ as it decreases the total free energy of the system. As nucleation proceeds, different new surfaces and interfaces start to form resulting in an increase of the surface free energy given by $4\pi r_2\gamma$, the term γ is the surface free energy per unit area. Thus, the total free energy change is,

$$\Delta G = \frac{4\,\pi r^3 \Delta G_v}{3} + 4\pi r^2 \gamma \tag{22}$$

On equating the differential of above equation to zero, the minimum energy and radius required to continue the deposition through nucleation process is obtained.

Hence, the equilibrium nuclei size is,

$$r = r* = -\frac{-2\gamma}{\Delta G_v} \tag{23}$$

Hence, the minimum activation energy to initiate the nucleation process will be,

$$\Delta G_{T*} = \frac{16\pi \Upsilon^3}{3(\Delta G_v)} \tag{24}$$

In the nucleation process of the solid cluster, if the radii is less than r*, this unstable cluster loses atoms and will shrink. However, if clusters are of greater dimension than r*, they will continue to grow larger leading to lowering the free energy of the system.

5.1.5.1 Nucleation Rate

Nucleation rate (N), defined above, is directly proportional to three physical quantities [31],

$$\mathrm{N} = \mathrm{N} * \mathrm{A} * \omega \ (\mathrm{nuclei/cm^2 - sec}) \tag{25}$$

Where N* is the number of nuclei per unit area at equilibrium and ω is the rate of atomic impingement onto the nuclei of critical area, A*. The density of all possible sites (n_s) can be related to the Boltzmann factor as,

$$N * = n_s exp(-\frac{G*T}{kT}) \tag{26}$$

Now the flux (ω) can be defined as the product of the concentration of vapor atoms and the velocity of the vapor atoms striking the nucleus,

$$Flux(\omega) = \frac{\propto (P_\vartheta - P_s)N_A}{\sqrt{2\pi MRT}} \tag{27}$$

Where $\propto$ is the striking coefficient and M is the atomic weight,

$$N = n_s exp(-\frac{\Delta G*T}{kT}) 4\pi r^2 \frac{\propto (P_\vartheta - P_s)N_A}{\sqrt{2\pi MRT}} \tag{28}$$

The above equation shows that the exponential term is most influential while determining the nucleation rate during thin film deposition. From the above discussion of nucleation process, it is concluded that the nucleation rate is a function of vapor supersaturation (S=$(P_\vartheta - P_s)/P_s$), where the greater the S value, the higher will be the nucleation rate by decreasing the chemical energy of the system.

5.1.5.2 Growth Rate

Thin film growth rate primarily depends upon the,

- Rate of flow of the reactant to the substrate through the boundary layer.
- Rate of adsorption of reactant at the substrate.
- Adsorption of reactants on the substrate, surface diffusion, chemical reaction and incorporation into the lattice in atomic and molecular forms.

- Transport of product away from the substrate through the boundary layer.

Let us consider the case of a horizontal reactor with precursor gases flowing from one end (x = 0) then a mathematical expression for thin film growth rate can be written as below. (The complete derivation can be found in [31].)

$$G(x) = \frac{2C_i M_{si}}{b\rho M_s} D \exp\{-\frac{Dx\pi^2}{4vb^2}\} \quad (29)$$

The above equation is very informative as it gives the basic idea of growth rate dependent parameters in the horizontal reactor and may be applied broadly to CVD growth processes. Where D is the diffusion of individual gas molecule, C_i is the concentration of input source gas with drift velocity as v, b is width of the reactor, M_{si} and M_s are the weight of silicon and source gas respectively, ρ is the density of Si. The above equation gives the design guidelines to obtain the desirable thin film growth rate for the case of silicon. From the equation it is seen that the growth rate is exponentially decaying with the distance (x) from the source gases. The growth rate is not uniform in a reactor, with a maximum growth rate at the precursor gases input end and the growth rate is minimum on the opposite end. Similarly, an expression of diamond growth rate may be obtained by modifying the basic assumptions.

Nucleation and growth of thin films can be effectively analyzed via the following steps:

- Adsorption
- Surface Diffusion
- Chemical Binding

Depending upon the nature of the substrate and material to be deposited, different modes of crystal growth on the surface have been proposed.

5.1.5.3 Island or Volmer-Weber Mode

When the atoms to be deposited are bound more strongly to each other than to the substrate, small clusters tend to nucleate on the surface forming islands. These islands ultimately coalesce to form a thin layer. Most metals (alkali metals) when deposited over insulators (graphite, mica) show this type of growth mechanism [32]. The process of forming islands of different size over the substrate instead of a single thin layer and coalescence of those island can be visualized in Figure 9 (top).

5.1.5.4 Frank-Van der Merwe Mode

In contrast to the Volmer-Weber method, if the material to be deposited has a stronger affinity to the substrate then formation of a complete monolayer over the substrate is more favorable. The subsequent layer that forms over the first monolayer is less bound than the first monolayer. This type of growth scheme is prominently found in adsorbed gases on graphite, metal on metal and semiconductor on semiconductor growth [32]. The growth mode is shown in Figure 9 (middle).

5.1.5.5 Layer Plus Island or Stranski - Krastanov Growth Mode

In this mode, after the growth of one, or a few, monolayers over the substrate, layer formation terminates, and island formation becomes more favorable, thus yielding several islands over the preceding layers. This discontinuity in layer formation is because of the monotonic decrease in binding energy of the layers that are deposited sequentially. The lattice parameters, symmetry or molecular orientation are the important factors that decreases the binding energy of subsequent layers. This mode is commonly found in metal - metal, metal - semiconductor, gas - metal and gas - layer systems [32]. The formation of islands above a few layers is shown in

Figure 9(bottom) which is due to the decreasing binding energy of the layers as explained before.

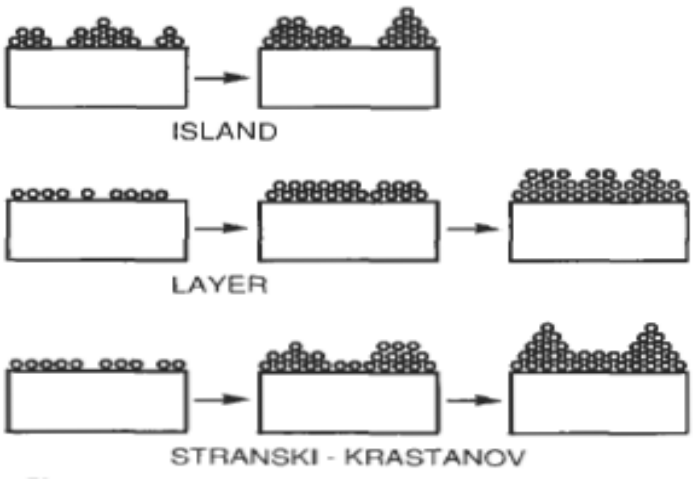

Figure 9: Different types of nucleation modes of epitaxial deposition process[31]

5.2 Metal Organic Chemical Vapor Deposition of III- Nitrides

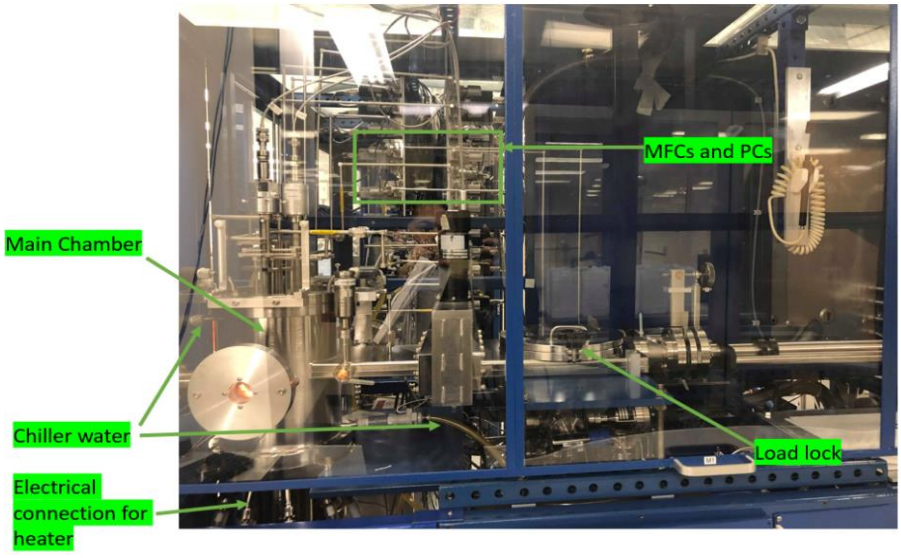

Figure 10: III-Nitride MOCVD reactor at Texas State University (view from deposition chamber side)

Figure 10 is the MOCVD system at Texas State University used to grow III-Nitride thin films for our research group's purposes. In the figure the main chamber, load lock chamber, MFs and PCs, chilled water circulation and electrical connections are visible whereas the MO bubblers, gas purifiers and gas cylinders are in separate compartments. Hydrogen is used as the carrier gas while Nitrogen is used for purging the system. All gases pass through chemical purifiers before reaching the main chamber. All the gas cylinders are connected to two stage regulators to control the gas pressure of the cylinders. There are three main components of the MOCVD systems: gas delivery system, main reaction chamber and exhaust system. The growth mechanism inside the MOCVD chamber requires the precise balance of hydrodynamics, thermodynamics, chemical kinetics and chamber geometry in order to grow thin films having excellent electrical, optical and geometrical properties [33].

The growth process is highly complex and involves organometallic compounds (such as TMGa and TMAl), hydride compounds (Ammonia and Silane) and Hydrogen (and/or Nitrogen) as the carrier gas. The organometallic compounds, also called precursors, are pyrolyzed and react with the ammonia to form thin layers of respective compounds (such as GaN and AlGaN). The detailed chemical reactions inside the MOCVD growth chamber is complicated but the basic reaction mechanism can be summarized by the following reaction equation [33].

Organometallic Compound (R_3M)(g) + Hydride (EH_3)(g) $\rightarrow$ ME(s) +3RH(g)

Where R is organic radical (methyl or ethyl) M is the column III metal atom (Ga, Al or In), and E is the group V atom (N).

AlGaN/GaN HEMTs are grown in a cold wall vertical flow MOCVD system following a standard growth recipe using Trimethylgallium (TMGa), Trimethylaluminum (TMAl), Ammonia (NH_3) and Silane as precursors along with H_2 as the carrier gas [34]. After heating the 100 mm diameter Si (111) substrate to ~ 1020 ºC ammonia is flowed for the nitridation of the silicon surface. A

420 nm AlN nucleation layer is first grown on the substrate. The precursor gases to grow AlN layer are TMA and ammonia. This nucleation layer is followed by transition layers, T_1 and T_2 of 550 nm (x=0.5) and 300 nm (x=0.26) $Al_xGa_{1-x}N$, respectively. The purpose of these transition layers is to minimize the effects of thermal mismatch due to CTE and lattice mismatch, since AlGaN is an intermediate material between AlN and GaN. Immediately after the transition layers, an 870 nm GaN buffer layer is grown, then topped with a 1.5 nm AlN layer followed by a 25 nm $Al_{0.28}Ga_{0.72}N$ layer then capped with a 1.5 nm GaN layer. The GaN cap reduces the surface roughness of the top layer. Formation of the two-dimensional electron gas (2DEG) due to piezoelectric polarization takes place on the GaN side of the AlGaN/GaN interface. These layers are all grown at temperature between 950 and 1020°C with a V/III ratio in the chamber between 1,900 to 8,000 and chamber pressure was 30-100 Torr. These growth steps lead to a complete HEMT structure but to make the desired ELOG GaN sample the process is halted immediately after the GaN buffer layer growth and then the sample is subjected to a SiN_x passivation/protection layer, diamond stripes and GaN ELO overgrowth.

5.3 Epitaxial Lateral Overgrowth of GaN

As mentioned above, a SiN_x protection layer was grown on top of the GaN buffer layer in order to protect the underlying layers during diamond stripe formation and deposition. This thin (100 nm) layer of SiN_x was grown by Plasma Enhanced Chemical Vapor Deposition (PECVD) as this deposition is an efficient means of depositing this kind of dielectric layer. Selective deposition of CVD diamond was done after patterning the wafer with nano-diamond seeds by photolithography [9]. Dimethyl Sulfoxide (DMSO) and Nano Diamond (ND) were sonicated to make a uniform suspension before depositing with a photoresist process. ~ 5 mL of the suspension was dispersed on the sample surface using a spin coater then soft baked for 90 sec at 110°C then exposed under a photolithography contact aligner (SUSS MicroTech) to create the desired patterns. After this development, the sample had diamond seed laden regions and clear,

unseeded regions. To further enhance the selectivity during the diamond CVD process, the sample was subjected to Reactive Ion Etching (RIE) plasma processing in a mixture of 45 sccm CF_4 and 5 sccm O_2. Any remaining diamond seeds on the exposed regions were removed by applying RIE for better selective diamond growth. Furthermore, RIE was performed after the selective diamond deposition to remove the SiN_x layer in the exposed (non-diamond) regions to expose the GaN layer to facilitate ELO GaN deposition.

Diamond was deposited by HFCVD with a filament temperature of 2200 °C, a substrate temperature of 720-750 °C, a drive power of 6 kW, and a 3.0 % methane concentration, which yields the best quality diamond with the lowest surface roughness and minimal occurrence of NDC. Based on the mask used, diamond stripes of nominally 1, 2, 5 and 10 µm width with many other features of approximately 600 nm thickness were formed.

ELO GaN over a dielectric mask is a proven technique to grow better quality GaN as it reduces the dislocation density [35]. The growth anisotropy of GaN in various crystallographic orientations is a function of growth temperature, pressure, V/III mole ratio and mask orientation [36]. High temperature and low pressure were the most favorable conditions to grow the ELO GaN as reported by Kapolnek et al. [36]. In the ELO process GaN is first grown in the window region (the opening between stripes) of the masked GaN template and once the opening is filled, GaN grows both in the vertical and lateral direction. Under suitable conditions the two wings growing from opposite sides of the masked region coalesce producing high quality GaN. For a circular mask opening ELO results in hexagonal pyramids with {1$\bar{1}$01} facets while for the parallel stripes, GaN growth direction is dictated by the mask orientation. The MOCVD growth process may not be perfectly isotropic. Even if all the incoming gases have uniform flow rate, the diffusion of the various active species through the boundary layer can be different which is the determining factor of growth rate. The diffusion rate of active species through the boundary layer is controlled by the surface structure within their mean free paths [37]. The

growth anisotropy, and hence ELO GaN, is possible in MOCVD because the diffusing molecular species are incorporated onto different crystallographic sites at different rates. These are the reasons why ELO is possible in MOCVD but not in molecular beam epitaxy.

To get a single crystalline ELO GaN on diamond with complete coalescence, GaN-diamond feature area, mask orientation, and growth process were varied [1]. The growth process was optimized by varying ammonia to trimethylgallium ratio from 8000 to 1330, chamber pressure from 40 to 200 torr and temperature from 975 to 1030°C. Higher V/III ratio results in higher lateral growth. The lateral overgrowth of GaN on the stripe edge or pyramid sidewall is proportional to the TMGa incorporation probability which is affected by the NH_3 partial pressure [36]. Hence, lateral growth can be increased by increasing NH_3 partial pressure to enhance its decomposition to surface active nitrogen. Also, higher surface-active nitrogen can be produced by higher growth temperature due to higher decomposition rate of NH_3. Hence, higher V/III ratio, higher NH_3 flow rate, and higher temperature increases the incorporation of Ga resulting in higher lateral growth [36]. Despite achieving higher Ga incorporation probability by maintaining the above-mentioned conditions there is one side effect of accumulating reducing agent (hydrogen atom): Surface etching. Hence, one should limit the V/III ratio to certain limits so as to achieve the maximum lateral growth rate and minimum surface etching phenomenon [36].

To investigate ELO GaN on diamond, the growth temperature 975-1030 °C, pressure 40-200 torr and V/III ratio between 1334-7880 were varied based on the system's capabilities. After a thorough study the best ELO GaN quality over the diamond stripes was produced with 100 torr pressure, V/III (ammonia to TMGa) ratio of 7880, and temperature at 1030°C [1].

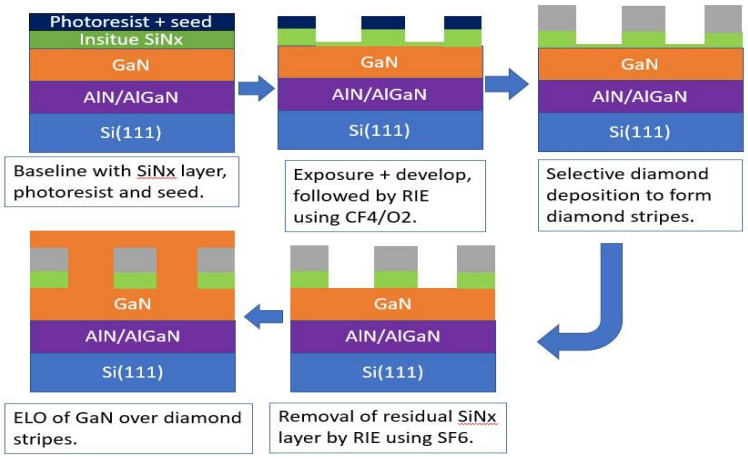

Figure 11: Overall process flow of the research plan.

5.4 Characterization of the Grown Sample

Optical microscopy, the Scanning Electron Microscope (SEM), and Visible Raman Spectroscopy was employed for the characterization of ELO GaN sample. A line scan in the Raman spectroscopy measurement was used to generate the stress map of the region of interest determined from optical microscopy and SEM. Additionally, point wise Raman mapping from the Visible Raman system was performed to get more detailed depth stress profile on the sample. All these characterizations targeted stress distribution and quality of overgrown GaN in the regions of interest.

5.4.1 Optical Microscopy

Figure 12: Analysis Research Service Center Optical Microscopy System at Texas State University.

The research samples on which Raman spectroscopy was planned had many different microscopic features, so determining the best region of ELO GaN was challenging. Optical microscopy was observed in brightfield mode (common mode of imaging in optical microscope) to locate potential regions of interest before conducting SEM on the larger wafer piece then used SEM to locate the exact position for Raman Spectroscopy of the ELO GaN region. In brightfield mode the light incident to the sample from the source gets reflected carrying the information of the sample to be examined. The optical microscope at Texas State University is shown in Figure 12.

5.4.2 Scanning Electron Microscopy

SEM may be used to observe the top surface and cross section of a sample from micrometer to nanometer range. Material can be removed in a very precise way by utilizing an ion beam, called the Focused Ion Beam (FIB) technique. Electron Dispersive X-ray Spectroscopy (EDS) is

available in the SEM with the help of a spectrometer to determine the chemical nature of material present in a given sample. The number of photons per second in a certain energy range is a strong indicator of the respective element(s) present in the sample and is the basic principle of EDS. The arrangement of various components of the SEM are shown schematically in Figure 13.

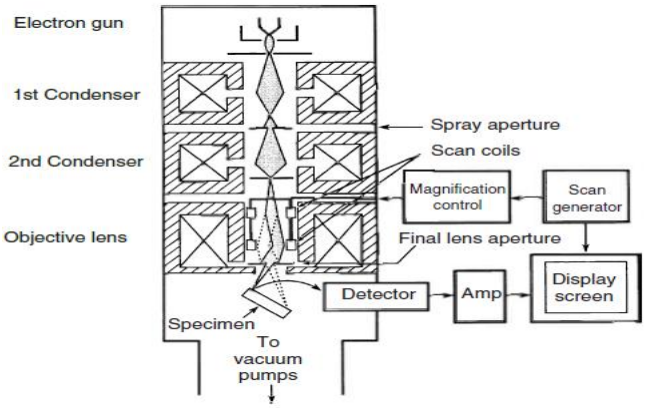

Figure 13: Schematic of Scanning Electron Microscope[18].

As shown in the figure SEM consists of an electron gun and a series of electromagnetic lenses. The electron gun used in SEM could be either thermionic or field emission and the beam produced from them will be passed through the condenser to finely focus the electron beam for surface scanning. Field emission type electron gun is mostly used in advanced SEM as it produces a stronger beam which gives better imaging quality [18]. Unlike TEM, the electromagnetic lenses (condenser 1 and 2 as shown in Figure 13) in SEM are not for image formation but for electron probe formation. Two condenser lenses focus the crossover diameter of the electron beam and then the objective lens focus the electron beam as a probe with a nanometer scale diameter. The objective lens acts like the condenser lens, so it is also called the third condenser lens in SEM. The SEM lens system demagnifies the electron beam by about 10,000× for a thermionic source and 10-100× for field emission source [18].

Thus, the electron beam interacts with the sample surface producing various types of signals from different depths of the sample such as secondary electron, backscattered electron, characteristic X-ray and other photons of different energies. The various detectors located in specific positions in the SEM receive the respective scattered electrons to reveal the various topographic, crystallographic, and compositional properties of the sample. Primarily, two detectors, the Everhart-Thornley detector (ETD) and through the lens (TLD) detector, are used for receiving the secondary electrons (SEs) and backscattered electrons (BSEs). BSEs are incident electrons scattered by the specimen after elastic scattering while SEs are the electrons ejected from atoms in the specimen after inelastic scattering. SEs mainly provide the topographic information about the sample while BSEs provide the information about the elemental composition of the sample. For low resolution field free imaging ETD is used while for high resolution immersion mode imaging TLD is used. The scintillator present in the detectors convert the signal electrons into photons by accelerating the electrons with +12 kV and striking them onto a disk. The produced photons travel through the light guide and enter a photomultiplier tube for signal gain (gain up to 10^6 times) and the output from the this tube is also amplified for display onto the screen [18].

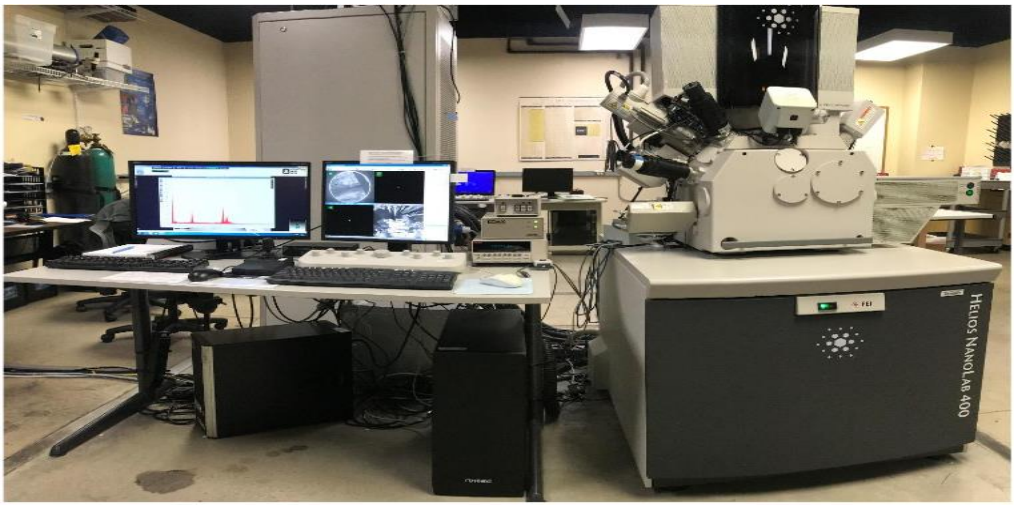

Figure 14: Analysis Research Service Center's SEM at Texas State University.

The picture in Figure 14 is the FEI HELIOS NanoLab 400 SEM available in Texas State University. This is fully equipped with FIB, EDS, electron beam deposition and electron beam lithography.

5.4.3 Raman Spectroscopy

Figure 15: Visible Raman Spectroscopy system in the Optical Microscopy Lab at Texas State.

Figure 16: Analysis Research Service Center's visible Raman System at Texas State University.

For the basic concept of Raman Spectroscopy, refer to Chapter IV where the classical and quantum approaches were presented. Raman spectroscopy was utilized to determine the stress distribution of the ELO GaN. Based on this Raman data and COMSOL modelling, the stress on diamond stripes, the ELO GaN just above the diamond stripes, and at the GaN wings and GaN in the window regions will be determined. Raman spectra across a cross section of the sample will be taken in order to obtain depth wise stress map. Additionally, determining stress distribution of the diamond stripes at the center and at the edge is especially interesting because our group has previously analyzed the stress distribution on diamond stripes without ELO GaN allowing for a comparison to observe the effect of ELO GaN on the diamond stripes. The setup of the visible Raman system residing in the optical microscopy lab that was used to obtain the line scan along the region of interest is shown in Figure 15. Figure 16 is the visible Raman system available in the ARSC lab which has the confocal focusing capability that is especially useful to conduct depth wise Raman mapping.

A coherent beam from a solid-state laser with wavelength of 532.0975 cm^{-1} was directed onto the sample with an Olympus microscope at magnification 100X and a Mitutoya Plan Apo infinity corrected objective of Numerical aperture 0.5. Emitted rays from the sample were directed into the spectrometer having a diffraction grating of 1800 gr/mm. Thus, incident rays were collected by the liquid nitrogen cooled CCD (Princeton Instruments) detector.

Before measuring the sample in Raman spectroscopy, the CCD must be calibrated using a standard Neon lamp. The Neon lamp is placed near the spectrometer slit and the diffraction grating of the spectrometer is rotated to get the peaks of the Neon lamp and compared to the calibration data. Once the known peaks are obtained, the corresponding wavelengths are correlated with the pixels and registered in the calibration software. The diffraction grating should be moved in such a way that it encompasses the desired Raman shift region related to

the sample. For example, a Raman shift of 520 cm^{-1} is included then the diffraction grating must be rotated in such a way that it displays a Neon peak of ~545 nm at one end.

$$Raman\ Shift(cm^{-1}) = 10^7[\frac{1}{\lambda_{ex}(nm)} - \frac{1}{\lambda(nm)}] \quad (30)$$

Mathematically, if ω_0 is the Raman shift for the reference sample and ω is the corresponding shift for a measurement sample, then the stress between the two can be related as follows,

$$\text{Stress} = \text{K}(\omega_0 - \omega) \quad (31)$$

where K is the stress factor which is known for given materials.

5.4.4 Data Analysis on MATLAB

In Raman Spectroscopy, the laser is rastered over a length of ~ 20 μm which corresponds to a CCD width of 400 pixels. Hence, each pixel corresponds to a position of the sample with a different Lorentzian curve. Handling 400 Lorentzian individual bases is difficult, so they are fit using a MATLAB program compatible with the curve fitting toolbox.

5.4.5 Finite Element Simulation to Determine the Thermal Stress

Finite Element Simulation was conducted with COMSOL Multiphysics 5.4 software. Structures of the sample were created using the structural mechanics module in the two-dimensional geometry. In this simulation the sample at high temperature (i.e. 1000 °C, the ~ GaN deposition temperature) was assumed as stress free, but at room temperature (20 °C) it has stress due to different CTEs of the involved materials. In the continuum model approach, the Finite Element Simulation is performed by solving Hooke's law [38],

$$\sigma_{ij} = \text{D}(\varepsilon_{ij} + \varepsilon_{ij}^{th} + \varepsilon_{ij}^{0}) + \sigma_{ij}^{0} \quad (32)$$

And thermal strain is expressed as,

$$\varepsilon_{ij}^{th} = \alpha_{ij}(T - T_{ref}) \quad (33)$$

Where ε_{ij}, σ_{ij} and α_{ij} are the components of strain, stress, and CTE tensors, respectively. D is the elasticity matrix which is a linear approximation independent of ε_{ij} and T_{ref} is the reference temperature at which the sample is in zero thermal stress. The elasticity matrix, D, can be derived from two quantities, Young's modulus, and the Poisson ratio.

The studied sample has several III-Nitride layers below the diamond stripes as discussed previously in Section 5.3, but for simulation purposes the structure was simplified by placing a GaN layer on the Si substrate then diamond stripes and finally the top layer ELO GaN as shown in Figure 17. The bottom Si substrate was 500 µm, above which a GaN layer of 2 µm then diamond stripes of different width (2, 5, and 10 µm), different spacing (1:1, 1:2, 1:3) and a thickness of 0.75 µm were placed. The top ELO GaN layer of 5-10 µm thickness is placed just above the diamond stripes without any intermediate layer.

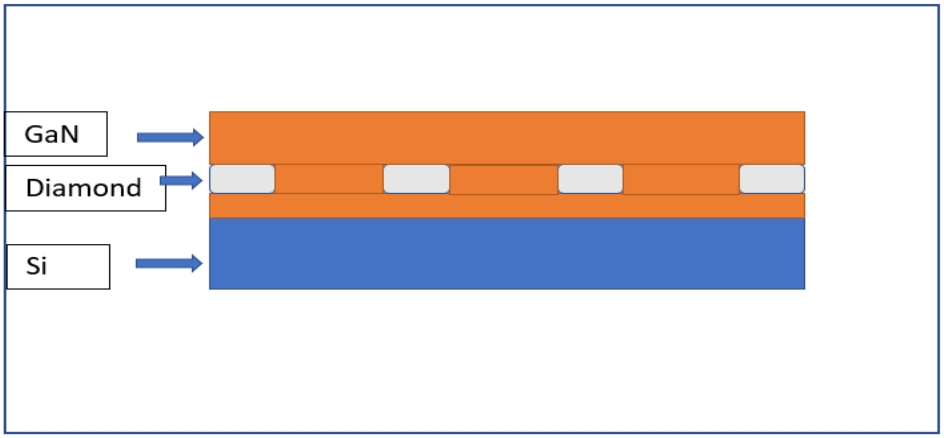

Figure 17: Simplified model of research sample for COMSOL modelling.

In the simulations, a 2D geometry was taken that contained at least 3 diamond stripes so that the effect of one stripe to the adjacent stripe can be compared, if present. Since the film is thin, the in-plane stress on the sample is of primary interest. Hence, the sample is restricted from moving in the z-direction (i.e., perpendicular to the cross-sectioned regions, or along the stripe), but is free for fictitious deformation (the grid itself is not moving, termed fictitious) in both the x and y directions. Theoretically, based on elastic formulation, the stresses at the corners of the diamond-GaN interface is infinite unlike the Finite Element Simulation where the stress is finite even at those corners. However, the stress value can be optimized by increasing the number of mesh points until saturation. Therefore, extremely fine mesh (optimized number of grid points and their separation), less than the dimensions of the thin film were formed so that the region of interest is sufficiently dense for the accuracy of the calculation. Since stress is a function of distance, different cut lines over the thickness of diamond and GaN were drawn to extract the average stress data from the respective region of interest.

COMSOL software was used to calculate the thermal stresses developed in the structures when the sample is taken from the deposition temperature (high temperature) to room temperature. Since CTE values for Si, Diamond and GaN are temperature dependent, using one value at all temperature is not reasonable. For thermal stress, CTE is the most important factor and CTE dependence with temperature is shown in Figure 31. Based on the CTE graph the stress variation on the sample from deposition temperature to room temperature is estimated. In principle, the greater the difference in CTE the higher will be the thermal stress at that temperature. To use the temperature dependent CTE values for all the materials the interpolation function from the COMSOL software is applied. That being said, the reliability of simulation results is dependent on the the reliability of the CTE value used in the simulation. For Si, the CTE value should be very close to what has been used here but for diamond and GaN, the CTE might be slightly different for the sample relative to published results. This is because CTE is a material dependent

property so the reference sample and the experimentl sample may not match well because of different growth conditions, different substrate, etc. From published results CVD diamond is known to have higher CTE as it has higher NDC content so the higher value found in Slake et. al. [39] was used. The temperature dependent CTE for Si was taken from Okada et. al. [40] and the respective values for GaN were taken from Reeber et. al. [41]. Finally, the CTE data for GaN could also be impacted by the ELO process due to different crystallinity, different underlying (substrate) materials and growth environment, compared to GaN deposited directly on silicon.

Besides CTE, there are other material properties to consider for the accuracy of the simulation. It is assumed that the material is perfectly isotropic. Another important factor to calculate thermal stress is Young's modulus which is strongly dependent upon the growth technique and growth chemistry. (Reports with different Young's modulus values can be found elsewhere [42, 43].) The prevailing direction of strain is determined by the crystallographic orientation of the Si. For Si(100), the biaxial stress value leads to deformation mostly along {110}, therefore Young's modulus of Si(110) was used in the modeling to improve the accuracy of the simulation. The anisotropy in mechanical properties of randomly orientated diamond is low [38]. The Young's modulus for CVD diamond increases with increasing diamond grain size, and is also dependent on the CVD method and measurement technique. However, the ratio of Young's modulus between Si and diamond is very low and, hence, the variation in Young's modulus for diamond, between 900-1200 GPa, does not significantly change the stress value as observed in COMSOL so Young's modulus for diamond as 1000 GPa [38] was chosen.

6. RESULT AND DISCUSSION

6.1 Scanning Electron Microscopy of ELO GaN Structure

The studied structures have several features, including nearly coalesced ELO GaN as well as uncoalesced ELO GaN. Finding a desired region with coalesced smooth surface ELO GaN on top of diamond is the starting point of the research. However, stress distribution in uncoalesced features is also interesting. While a smooth GaN top surface is observed in regions of interest, that may or may not indicate the presence of diamond stripes underneath such (mostly 1 mm and 2 mm) features. The Focused Ion Beam (FIB) technique was used to drill down until the diamond stripe was observed. A typical representative SEM image from the top view showing the coalescence of GaN wings to some extent and cross section view with a void near the coalescence region is shown in Figure 18.

Furthermore, the GaN top surface does not always have a smooth appearance everywhere. Instead the surface exhibits cracks, voids and pinholes in the ELO GaN region. Thus, finding good regions of interest while avoiding these features is one of the main purposes of employing SEM Characterization.

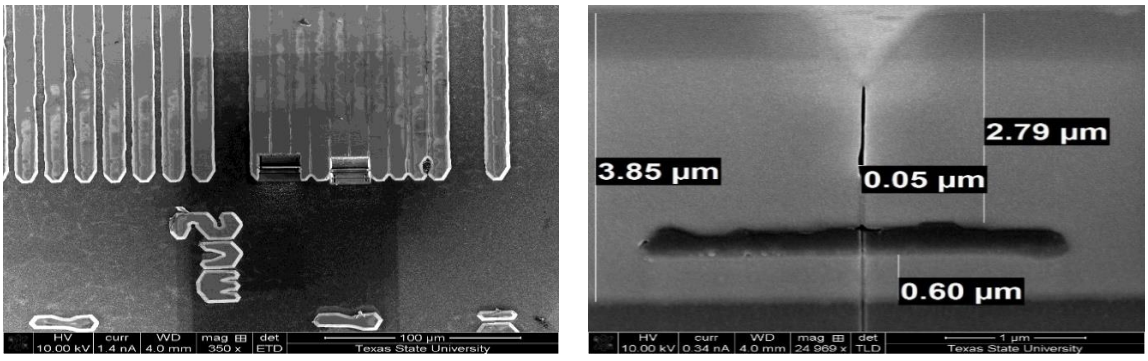

Figure 18: SEM images of ELO GaN features: top view (Left) and cross section view (Right).

6.2 Raman Spectroscopy of the ELO GaN

6.2.1 Epitaxial Lateral Overgrown GaN Stress

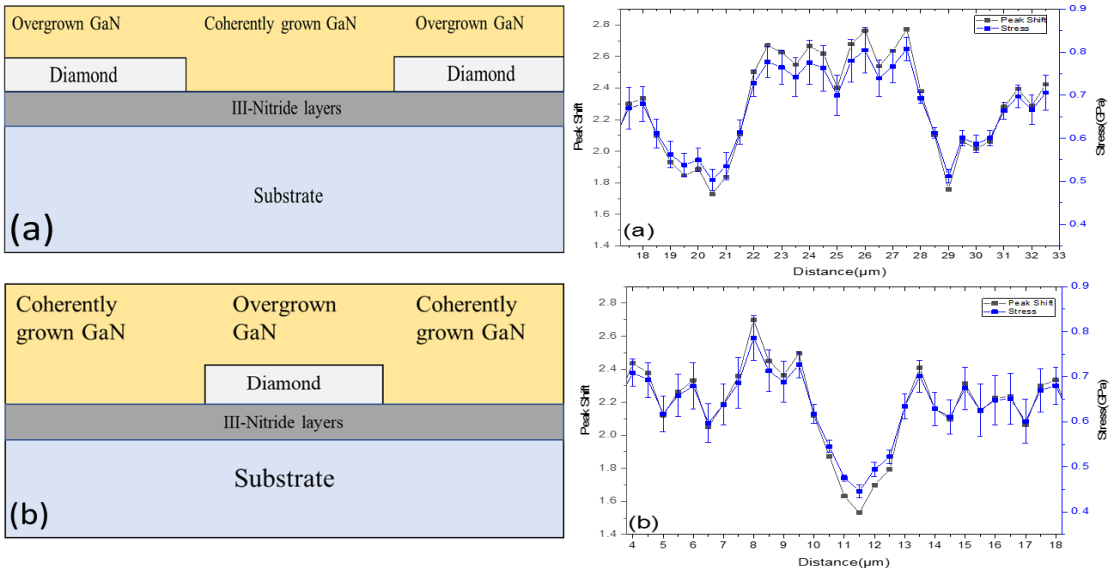

Figure 19: Schematic cross section of sample (left) and corresponding stress distribution (right) in the (a) ELO GaN (Overgrown) and (b) window GaN (Coherently grown) regions.

Figures 19(a) and 20(b) are representative graphs for horizontal stress distribution of the sample. Generally, window GaN has higher stress than ELO GaN. Determining stress distribution in ELO GaN is important to understand how the GaN layer is behaving over the diamond and non-diamond regions. Theoretically, greater stress in the GaN layer over the diamond region as compared to non-diamond region (GaN grown over the GaN window region) due to high lattice and thermal mismatch between GaN and diamond is expected. However, the result was completely different from the expectation as seen in Figure19. The GaN stress above the diamond stripe is low while the stress near the non-diamond region is high.

There are several prospective reasons for this partial relaxation. The two wings growing from the opposite sides of the diamond stripe are not perfectly coalesced so a “free space” near the coalescence region allows for the expansion of the GaN wings thereby causing lower GaN stress

over the diamond stripes. Described another way, if there was a perfectly coalesced ELO GaN layer above the diamond stripes then higher stress should be observed above the diamond region as compared to the non-diamond region, as indicated in COMSOL modelling (discussed later, in Section 6.4). Based on TEM observations (shown in Figure 30) the GaN nucleating over the diamond surface follows the diamond roughness for several nanometers which explains several of the observed gaps in-between diamond and ELO GaN. Also, the reactant species are not likely to deposit uniformly over the rough diamond surface giving greater GaN deposition at the hills which are the relatively tall facets of the diamond crystal. In between the hills, in the low diamond regions (or valleys), the GaN deposition probability is low because of the hills creating a discontinuity between the diamond-GaN surface forming voids and gaps which is observed in TEM as bright contrast at the interface. Thus, besides voids at the non-coalesced GaN wings, gaps are present in-between GaN and diamond thereby introducing regions of lower stress above the diamond stripe.

Another possible reason for lower stress could be diffusion of carbon into the GaN layer just above the diamond region that was observed by TEM[44]. However, the contribution of carbon doping for lowering the stress in overgrown GaN is significantly low as compared to impacts of the void between the GaN wings, gaps between the GaN-diamond surface and defects near the coalescence region.

In brief, dopant stress is based on the Raman results of Gogova et.al. [45] in which the carbon doped GaN layer was compressively strained. So, one possible contribution for getting lower tensile strain on GaN over the diamond stripes could be the carbon doping concentration which is not found in coherently grown GaN as discussed above. The impurities potentially increase the defects in the material and hence decreases the stress. The FWHM values of carbon doped GaN grown by Gogova et al. [9] was very close to the bulk good crystalline GaN which matches the present ELO GaN results. However, in the case of ELO GaN, the good FWHM value is not

principally due to carbon doping. Rather, the FWHM value close to bulk in ELO GaN, analogous to good crystalline GaN, above the diamond is attributed to the lateral overgrowth mechanism which significantly reduces the threading dislocation density. The FWHM value of ELO GaN was low compared to coherently grown GaN indicating good crystalline ELO GaN even though diffused carbon into the ELO GaN was observed. The theoretical understanding of carbon doping is further verified by TEM measurement with strong evidence of diffused carbon in the ELO GaN surface, however, the exact carbon concentration in the GaN surface is unknown[44]. (For a detailed explanation of the mechanism of carbon diffusion above the diamond stripes and stress relaxation refer to Appendix 1.)

When two wings coalesce, there is a high probability of defect formation at the coalescence region. The probable reasons for defects near the coalescence region is wing tilting [2] and insufficient lateral overgrowth of GaN wings to form fully coalesced overgrown GaN. These defects are expected to reduce the stress in ELO GaN as observed in the Raman data. Due to high interfacial stress energy at the GaN-diamond surface there is a significant probability of GaN wing tilting of the overgrown region by lowering the interfacial stress energy which is responsible for increasing defects in the ELO GaN [2]. While unequal wing growth rate has been reported to create difficulties to coalesce two wings, this is not evident in the sample studied here. Rather, in the 5 μm stripe regions studied, initially, the lateral wing growth rate seems to be insufficient to coalesce and because of this void of different dimensions near the diamond are observed. However, the wings are observed to coalesce after a certain ELO GaN thickness.

The material underlying the diamond stripe consists of a Si substrate, AlN, AlGaN and GaN, respectively, and these underlying layers are the major contributors for higher stress in the GaN above the non-diamond regions (i.e., the window regions). Since the Si thickness is substantially greater compared to AlN, AlGaNand GaN it is the most dominate factor for higher stress in GaN above the non-diamond regions. CTE of Silicon is lower compared to that of GaN, explaining the

tensile stress measured in the GaN layer. The local non-uniformity in stress map pattern, as shown in Figure 19, is attributed to the nature of the sample. While some regions have voids, pits and cracks over the surface, such defects were generally not present in the coherently grown GaN regions (i.e., GaN grown in the non-diamond windows). However, the ELO GaN had some of these defects in the region of interest. Furthermore, the GaN-diamond interface is not perfectly smooth as indicated by discontinuities due to the formation of gaps along the diamond-GaN interface and the distribution of dislocations is also not uniform which combine to create the small deviations and fluctuations in the stress map data. These small fluctuations are due to the different local stress distributions close to the void and dislocations compared to the GaN-diamond in perfect contact and dislocation-free regions.

Because of different CTEs the sandwiched GaN and diamond stripes located side-by-side do not have the same dimensional change upon cooling. During ELO growth the sample was ~ 1030˚C which is modeled as the stress-free state. As the sample cools to room temperature, because of its higher CTE, GaN sandwiched between two diamond stripes contracts more creating higher tensile stress in comparison to the diamond stripes that have a lower CTE. This mechanism will also aid in increasing the GaN stress in non-diamond regions of the sample.

Finally, Raman measurements were taken from the position where the diamond signal from depth dependent Raman scanning was maximum so that stress data are from the GaN layer very close to the diamond stripes. The stress difference between coherently grown GaN and overgrown GaN is about 0.20 GPa, on average. The stress is continuously decreasing from the window wing boundaries to the coalescence region as shown in Figure 19.

6.2.2 Diamond Stress Underneath the ELO GaN

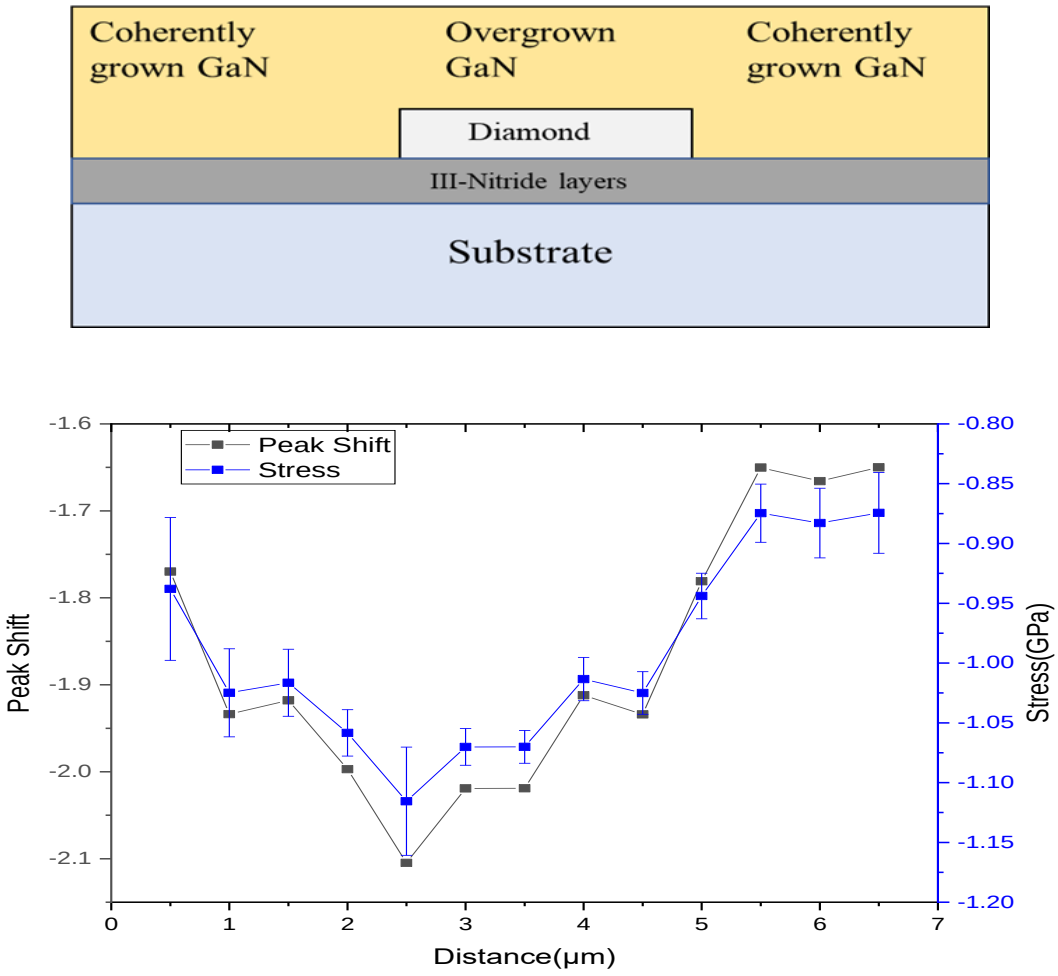

Figure 20: Cross section view of the sample(top) and stress distribution (negative sign indicates compression) on the diamond underlying the ELO GaN(bottom). Left axis is peak position shift while right axis indicates the corresponding stress.

Observing how the diamond stripes are stressed under the ELO GaN is of interest because the nature of stress distribution on the diamond stripes without ELO GaN was previously measured on 20, 40 and 80 um width diamond stripes grown over a Si wafer, as reported by Ahmed et.al. [9]. Since the CTE of diamond is less than both GaN and Si compressive stress across the diamond stripes is expected, which matched with the experimental results, as shown in Figure 20. Compressive stress is maximum at the center of the stripe and minimum at the edges. As

described by Ahmed et al. [9] the reason for low stress at the edge of the diamond is due to the presence of free side walls which permit relaxation of the diamond stripes. The maximum stress at the center of the diamond stripe, again similar to the results of Ahmed et.al., is explained by a lack of uniform contact between ELO GaN and diamond as seen in Figure 30. While diamond stress is expected to be lower for smaller stripe width, due to the significant thermal mismatch between diamond and GaN a maximum stress of -1.15 GPa is observed, which is comparable to the diamond stripe stress of 20 μm over a Si substrate measured by Ahmed et.al. The diamond rests upon a SiN_x protective layer but due to the harsh diamond growth environment parts of the SiN_x layer were ruptured as observed by TEM and shown in Figure 30. This structural defect is one reason for the local deviations in the stress pattern (fluctuating stress data points) because while most of the diamond regions have SiN_x as a protective layer, some regions have gaps directly underneath the diamond stripes. The SiN_x and GaN will have different thermal stress effects on the diamond stripe because of the intrinsic thermal properties of the involved materials.

6.2.3 Silicon Stress Distribution

The stress distribution in the Si substrate below the 5 μm diamond stripes was also measured. There was higher stress in the Si below the diamond stripes and lower stress in the Si below the non-diamond GaN regions as shown in Figure 21. This stress distribution is believed to be due to the diamond stripe patterns. The magnitude of the Si stress is low due to the intermediate GaN/AlGaN/AlN layers, acting as strain relief layers, sandwiched in between the diamond and Si substrate. The Si stress was expected to be highest for smaller diamond stripes if there were not any intermediate layers present as shown by Ahmed et.al. [9]. The higher Si stress with smaller diamond stripe width is due to the accumulated stress originating from the closely spaced diamond edges in comparison to wider diamond stripes (of comparable thickness).

The uncoalesced ELO GaN above the diamond stripe also contributions to lowering the Si substrate stress because the ELO GaN is relaxed thereby minimizing its stress effect on underlying diamond and Si. While the stress should be higher on the Si top surface near the GaN-Si interface the role of the visible laser to lower the Si stress must not be underestimated. The laser light is of 532 nm which corresponds to energy 2.3305 eV. The absorption coefficient for this equivalent energy is ~11190 cm^{-1} [46]that gives the penetration depth for silicon as ~890 nm being penetration depth is inverse of absorption coefficient. Hence one of the reasons for getting lower silicon stress is because of visible laser which has higher penetration depth then visible laser.

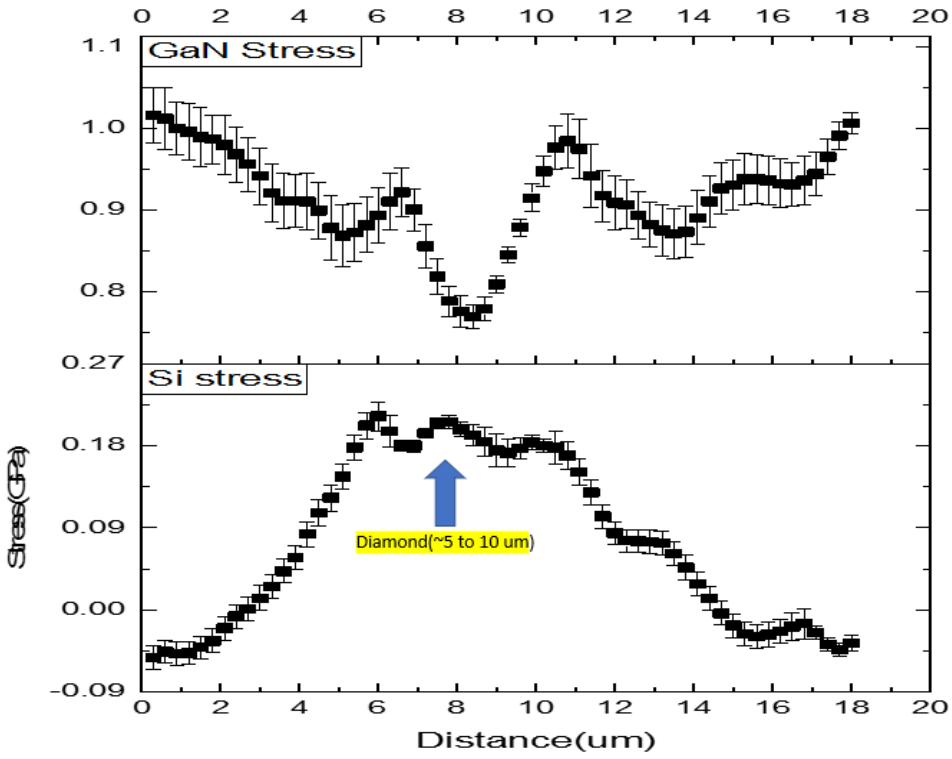

Figure 21: Graph showing the nature of Si and GaN stress above and by the side of diamond stripes. Diamond stripes of width 5 µm ranging from 5 µm to 10 µm in above graph.

6.2.4 Raman Modes of Epitaxial Lateral Overgrown GaN and window GaN

Since the diamond is polycrystalline, different diamond grains are expected to be oriented in different directions as shown schematically in Figure 22. From TEM measurements GaN is nucleated on the diamond facets, at least for a few nanometers, and dependent on diamond facet shape. The ELO GaN along the rough diamond could be laterally overgrown or directly deposited. This initial GaN orientation stops immediately after a few nanometers and then reorientation of the GaN occurs with the c axis parallel to the vertical direction.

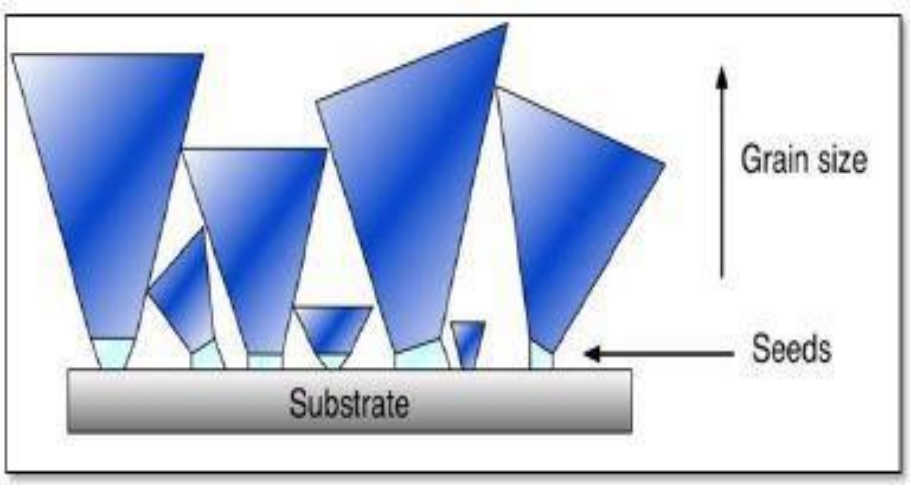

Figure 22: Schematic of diamond crystal orientation[47].

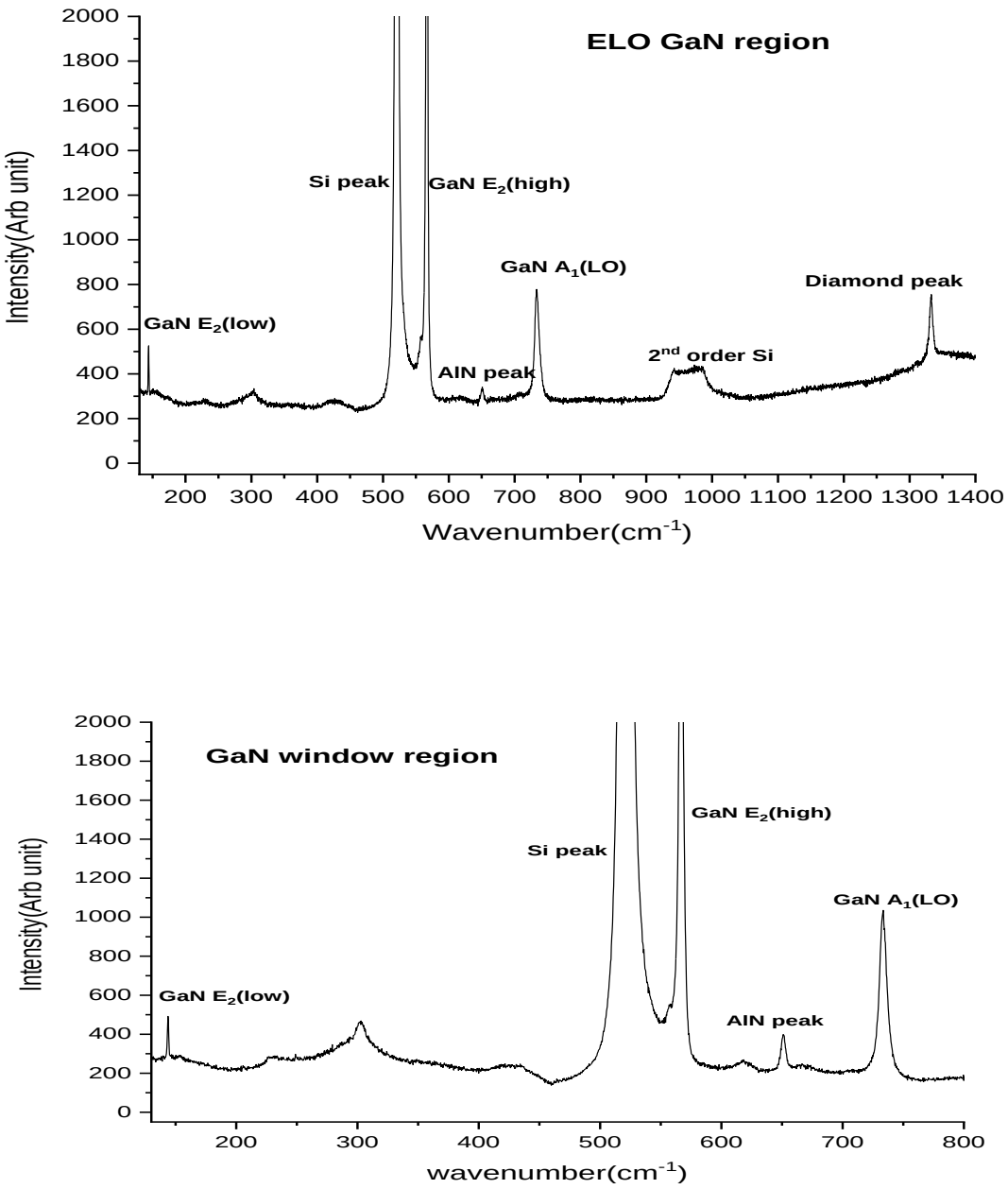

Figure 23: Representative Raman spectra observed in back scattering mode from the ELO GaN region (top graph) and from window GaN region (bottom graph).

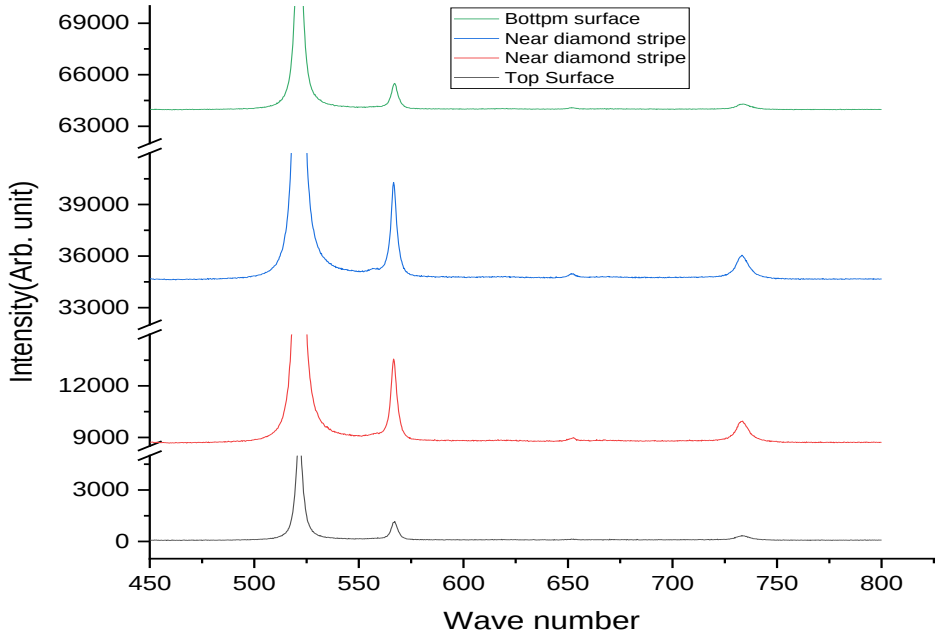

Figure 24: Depth wise Raman in non-diamond region. The highest dislocation density is observed in this region; however, the symmetry breaking Raman modes are not prominent.

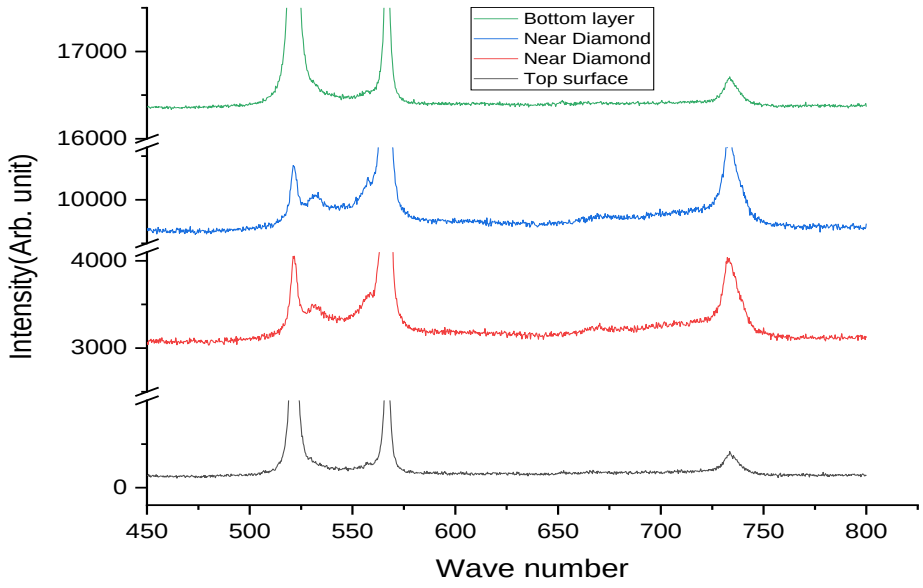

Figure 25: Depth wise GaN Raman from above the diamond region and near the coalescence region of the two wings. The spectra show the observation of symmetry breaking in the small peaks around 531 cm^{-1} and 558 cm^{-1} from the GaN near the diamond stripes which is absent in Raman peaks taken from the top and bottom GaN regions.

In Figure 23 (bottom graph), the weak GaN E_1(TO) peak around 558 cm^{-1} in the non-diamond region (window GaN region) is active even in backscattering mode which is likely due to the large threading dislocation density. This phonon mode does not appear (or has reduced intensity) while transitioning towards the top GaN surface on the same region, because of the comparatively lower threading dislocation density.

Scanning along the GaN growth direction on both the ELO GaN and window GaN regions, symmetry allowed Raman modes on window GaN is observed, as shown in Figure 24. However, on ELO GaN, interesting forbidden Raman modes are observed near the diamond stripes of the ELO GaN, as shown in Figure 25, which are not allowed in normal backscattering modes. The intensity of these forbidden Raman modes is higher near the coalescence region as compared to other ELO GaN regions indicating higher defect density near the coalescence region. The data presented in Figure 25 give a general indication that that the location of the forbidden Raman modes is near the diamond stripes.

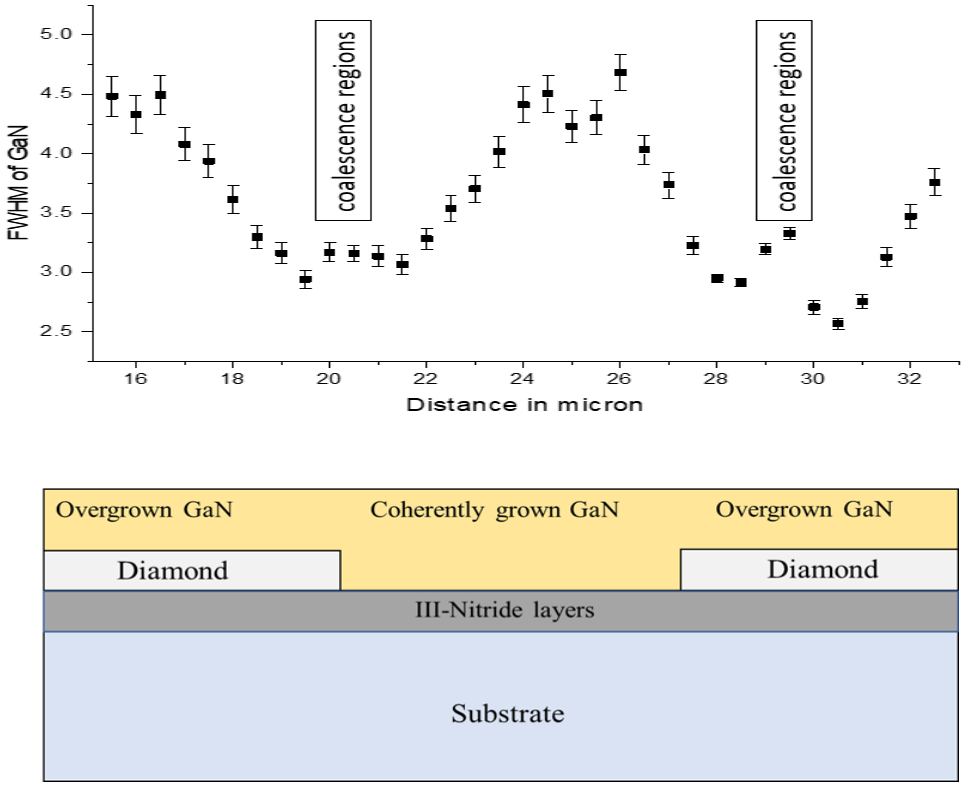

Figure 26: FWHM of ELO GaN corresponding to E_2 (high) phonons over diamond and non-diamond regions(top) and cross section view of measured sample(bottom).

As seen in the TEM images in Figure 30, the GaN threading dislocation density is greatly reduced over the diamond region because the diamond stripe acts as a barrier for threading dislocations and allow minimal dislocation bending along the GaN growth direction. Based on this observation the ELO GaN quality should be improved compared to the coherently grown GaN in the windows. The relatively small increase in FWHM locally at the coalescence region (near 20.5 µm and 29.5 µm in Figure 26) and the appearance of prominent symmetry breaking A_1(TO) at ~ 531 cm^{-1} and E_1(TO) at ~ 558 cm^{-1} modes from the Raman data indicate the presence of dislocations where the laterally growing wings coalesce, which is above the void in this sample. There is also the possibility of crystal tilting of two coalescing wings resulting in an off angle between the GaN c axis and backscattered photons in Raman [2]. The root cause of the high

defect density at the coalescence region is due to wing tilting and insufficient lateral growth rate. Globally, much higher FWHM at the nondiamond region is observed compared to the diamond region due to the higher defect densities in the nondiamond region. The FWHM continually decreases moving from the non-diamond region to the coalescence region indicating highest GaN crystalline quality along the wings.

The c axis tilting occurs to reduce the interfacial stress energy between the ELO GaN layer and diamond mask [2]. The GaN-diamond interface at the center of the 5 μm diamond stripe has a void (diamond is not directly in contact with GaN) and the potential for c axis tilting above the void is minimum as there is no interfacial stress energy. However, intrinsic defects and an unintentionally doped region may have high free carrier concentration [2] creating the possibility for different Raman modes which will be discussed later.

Hiramatsu et.al.[2] characterized the ELO GaN grown over SiO_2 and W masks and observed the accumulation of threading dislocations near the coalescence region in both types of stripes and detected the origin of threading dislocations from the center of the SiO_2 mask using TEM so this observation supports the above explanation of having higher FWHM value and pronounced A_1(TO) and E_1(TO) modes at the coalescence region of ELO GaN. However, the sample studied here does not have perfectly coalesced ELO GaN to compare to Hiramatsu's sample.

Another reason for higher defect density near the coalescence region is due to the stress accumulating in the diamond stripes and ELO GaN which may affect to some extent defect formation as a result of wing tilting up to several microns from the diamond surface. These symmetry breaking phonon modes decrease as one moves towards the top above the diamond stripes as shown in Figure 25 due to reorientation of GaN along the Z direction. The appearance of these phonon modes is prominent in the coalescence region and very low (sometimes absent) in the wing region (the region in-between no diamond and coalescence region). This observation

may indicate the diamond stress can be a factor for c axis tilting (wing tilting) as diamond stress is maximum at the center.

As previously discussed, the ELO GaN is distinguished by surface features such as voids, pinholes, and cracks while the GaN in the nondiamond regions (growing up through the windows) lack these surface defects. The ELO GaN / coalescence regions were easily distinguished with optical microscopy providing a convenient surface reference for taking Raman data. The symmetry breaking A_1(TO) and E_1(TO) phonon modes were more pronounced in Raman spectroscopy in the overgrown GaN region where the surface morphology has comparatively higher defects, i.e., near the coalescence region. Hence, the appearance of these symmetry breaking Raman modes is due to the presence of defects and misorientation of the GaN above the diamond stripes. The GaN orientation (at least for a few nanometers) is guided by the diamond crystal orientation, roughness and the stress accumulated on or above the diamond stripe.

The stress distribution pattern shows highest compressive stress at the center of the diamond stripes, this leads to an energy imbalance between the GaN wings and diamond stripe. This energy imbalance can tilt the wings at the coalescence region. Hence, a void is observed after which GaN is coalesced.

Due to the symmetry breaking effect five different phonon modes are observed in the Raman scattering experiment. Unfortunately, the E_1(LO) mode which would be present near 745 cm^{-1} was not ascertained. The reason for this is the overlapping A_1(LO) and E_1(LO) modes which will be discussed in detail in chapter 6.2.6. Only the E_2(high) phonon mode is highly sensitive to stress so the presence of its wave number is not constant because of the stress distribution pattern while other Raman mode peak positions are presented in Table 3 along with literature values for comparison [23, 48, 49].

Table 3. Phonon frequency comparison of different phonon modes collected from various references.

Reference	Phonon Frequency (cm^{-1})					
	A_1(TO)	A_1(LO)	E_1(TO)	E_1(LO)	E_2(low)	E_2(high)
6(Kozawa et al.)	534	736	563	745	…..	572
7(Perlin et al.)	531	…..	560	…..	144	568
8(Manchon et al.)	533	…..	559	…..	145	568
Present Work	531	733	558	…..	143.66	Varies with position

6.2.5 Stress Variation Along the GaN Growth Direction on ELO Sample

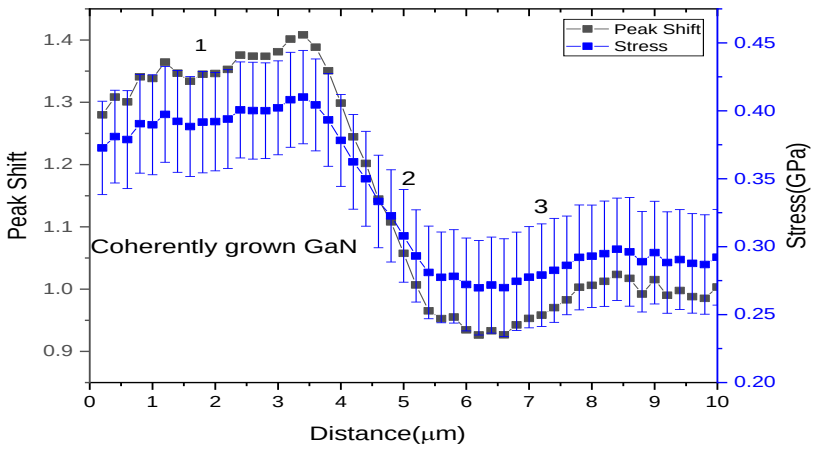

Figure 27: Depth wise peak shift in the non-diamond region of ELO GaN. 1 is the top GaN surface, 2 is the GaN region in between two diamond stripes and 3 is the bottom GaN region.

A relaxed GaN reference sample has an E_2(high) peak position of (567.760 ± 0.004 cm^{-1}). From this peak position the nature and magnitude of the stress distribution along the thickness of the ELO GaN can be estimated. In depth wise Raman scans above the diamond stripe region the diamond peak intensity increases around 5 to 6 μm from the top indicating the location of the diamond stripe. From Figure 27, a dramatic increase in peak shift of GaN E_2(high) is observed at the depth equivalent to the diamond stripe location as indicated by section 2 in Figure 27 which denotes an abrupt increase in stress along section 2. This increase in stress in the coherently grown GaN is due to the diamond stripes located on both sides of the GaN in this region and the effect of the relatively thick Si substrate. The coherently grown GaN and the diamond stripes on either side of it do not contract equally during cooldown because of different CTEs thereby creating a different stress level in the sandwiched GaN. Due to higher CTE, the GaN contracts more as compared to diamond which reduces the spacing between two diamond stripes assuming good GaN-diamond lateral bonding. The laterally located diamond restrict the relaxation of coherently grown GaN, hence, explaining the observed increasing stress pattern seen in section 2 of Figure 27. Moving towards the top, i.e. section 1 of Figure 27, the peak shift decreases while transitioning toward the surface, however, the decreasing trend is low compared to section 2 indicating a slow stress relaxation in the GaN layer. As the GaN layer thickens the stress relaxation is continuous moving toward the top surface, however, the stress relaxation trend is low. The trend in section 1 suggests that relaxed GaN can be achieved by increasing the overgrown GaN thickness. However, as previously discussed, cracks are present at the top surface alleviating a substantial component of the overall GaN stress, so increasing the GaN thickness further may not be practicable under the present growth conditions and sample geometry.

Section 3 in Figure 27 indicates the stress in the GaN below the level of the diamond stripe. While the GaN stress near the level of the diamond stripe is small, the stress increases moving towards the bottom. The increasing stress towards the bottom of the sample is due to the impact

of CTE mismatch from the nearby thick Si substrate. The lower GaN stress near and below the diamond stripe is due to the SiN_x layer which also acts as a stress relaxation layer in the sample. Thus, the Si substrate plays the major role in stress distribution in section 3 while the presence of the SiN_x layer in-between bottom III-Nitride layers and diamond stripe also has some effect.

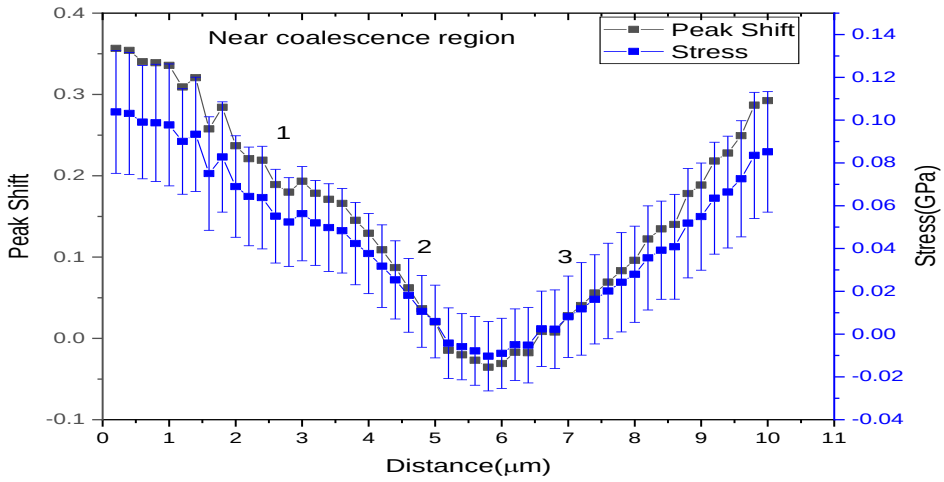

Figure 28: Variation of peak position in the diamond region of ELO GaN very close to the coalescence region (at the center of diamond stripe). Section 1 is the top GaN surface region, 2 is near the diamond stripe and 3 is the bottom GaN region which is below the diamond stripe.

The diamond stripe resides between 5 to 6 μm below the GaN surface. Figure 28 shows the lowest GaN stress on either side of the diamond stripe. The increasing GaN stress below the diamond stripes is because of the increasing impact of the thick Si substrate. Also, as explained in the previous section, comparatively low GaN stress under and near the diamond stripe as seen in section 3 of Figure 28 is most likely due to the presence of SiN_x which helps to relax the GaN near the diamond stripe. The stress is increasing going further away from the diamond stripe. In section 2 of Figure 28, i.e. close to and above the diamond stripe, the stress is low initially but increases monotonically throughout the ELO GaN. Initially, near the diamond interface the two wings do not coalesce forming a void but after a certain thickness they coalesce to some extent which tends to increase stress. This monotonically increasing stress pattern is an indication of

insufficient ELO GaN thickness to achieve fully relaxed GaN over the 5 μm diamond stripe. Sufficiently thick GaN must grow to remove the stress effect of diamond on the overgrown GaN. Low ELO GaN stress near the diamond stripe is due to the presence of voids at the coalescence region and gap between diamond-GaN interface.

6.2.6 Possibility of Longitudinal Optical Phonon Plasmon Coupling (LOPC)

The LOPC modes in III-V semiconductors has been studied extensively for many years and is useful to estimate the carrier concentration through the plasmon phonon coupling [23]. The LO phonon can couple with plasmons causing the line shape and peak position of LO phonons in semiconductors to change [23]. Based on the comparative study of line shape and peak position of LO phonons before and after coupling the concentration of free carriers in the semiconductor may be estimated. In the ELO GaN / diamond sample there are two regions which have the probability of having different carrier concentrations. Specifically, the window GaN and ELO GaN regions. The ELO GaN over diamond is likely to have more diffused carbon as evidenced by TEM[44]. Another important factor affecting the carrier concentration is defects which are high in the coalescence region and may result in a large number of carriers in that region. Based on this evidence, higher carrier concentration is expected on the overgrown GaN near the coalescence region as compared to the wings.

From the fitted graphs given in Figure 29, two overlapping LO phonon modes are observed in the coalescence region for A_1(LO) at 732.90 cm^{-1} and E_1(LO) at 736.24 cm^{-1} and the corresponding FWHM values are 5.90 and 7.36, respectively. Similarly, in the GaN window region the A_1(LO) and E_1(LO) modes are at 732.68 and 735.37 cm^{-1}, respectively while their corresponding FWHM values are 5.99 and 5.56. The data rule out the possibility of phonon plasmon coupling in the regions of interest because the broadened peaks (deviation from the Lorentzian line shape) are due to the overlapping of two LO phonons modes as seen in Figure 29. The A_1(LO) and E_1(LO)

phonon peak positions are comparable to the standard reference values and the FWHM values are also within the reasonable range [50] (not exceptionally narrow or broad). The fitted peak positions and their associated FWHM values validate the conclusion that peak broadening is due to the overlapping LO phonons mode and not due to coupling between LO phonons and plasmons.

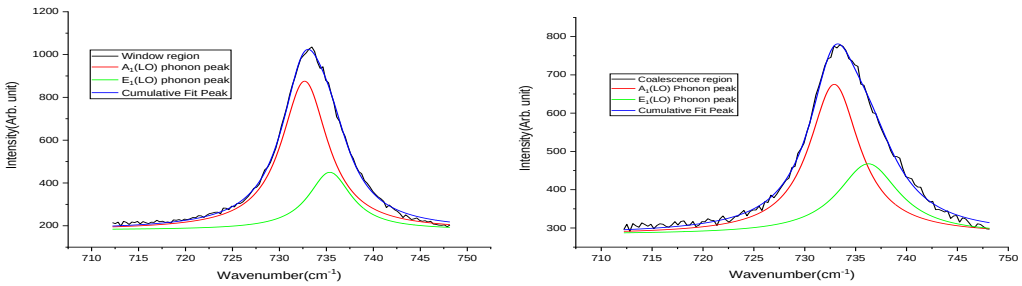

Figure 29: Raman Spectra near A_1(LO) modes on the diamond region and non-diamond region. The bottom graphs show overlapping A_1(LO) and E_1(LO) modes at the window region (left) and the coalescence region (right). The broadened peaks are due to overlapping two phonon modes.

6.3 Transmission Electron Microscopy of ELO GaN

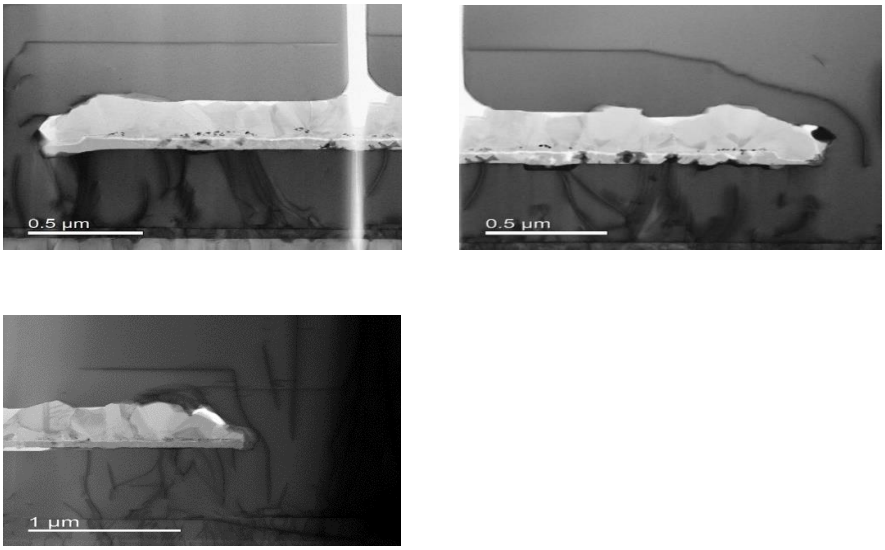

Figure 30: Cross-sectional TEM images of the ELO GaN / diamond stripe region. 2 mm diamond stripe (top) and one side of 5 mm stripe (bottom).

The most important parameters that effect stress distribution of ELO GaN over the diamond stripe are the degree of coalescence, contact between GaN and diamond, and the threading dislocation density variation over the region. TEM images proved useful for comparing and validating the Raman data with COMSOL stress distribution simulations.

The diamond stripe acts as a barrier for threading dislocations thereby reducing the dislocation density above the diamond stripes while the dislocation density is high just below the diamond stripes and in the coherently grown GaN regions. Furthermore, there is a high likelihood of dislocations when two ELO wings coalesce. (TEM analysis of the coalesced ELO GaN would be interesting in the future.) The bending of threading dislocations above the diamond stripe indicates the direction of GaN growth verifying ELO above the diamond stripe. Bright contrast regions at the GaN diamond interface indicates gap between these layers which is most probably due to GaN growth laterally and above the rough polycrystalline diamond stripes. As explained previously, there is a high probability of GaN ELO over the diamond hills as compared to valleys. The bright vertical line seen in Figure 30 (top left) below the diamond stripe is an image artifact produced due to the focused ion beam milling process. The ELO GaN above the diamond stripe follows the orientation of the diamond for several nanometer [44](not seen in these images) after which the GaN crystal reorients perfectly along the z axis i.e., vertically. Diffused carbon was observed above the diamond stripe with TEM EDS[44], however, the exact carbon concentration is unknown. The TEM images in Figure 30 also show the imperfect coalescence between the GaN wings. Also, due to the harsh growth environment the SiN_x protective layer is ruptured in some places making direct contact between GaN underlying the SiN_x layer and diamond stripes which indicates the SiN_x layer thickness is insufficient to fully protect the underlying device structure.

6.4 Finite Element Simulation of Thermal Stress

Validating the experimental results with simulation is important to gain a better understanding of how the sample is reacting during growth and its subsequent cooling. Due to high thermal mismatch (~73 %) between the GaN and diamond, most of the stress induced in the sample is expected to be from thermal stress and was modeled using COMSOL Multiphysics 5.4 software.

The COMSOL Multiphysics software simulates differential equations for complex geometrical situations, where analytical solutions are not possible, by dividing regions into finite elements. These finite elements are created by meshing and calculations are performed at each nodal intersection of the mesh elements. Several physics problems can be solved simultaneously by this technique by applying corresponding model information and boundary conditions. For the present study, the solid mechanics model was employed by applying appropriate desired boundary conditions to calculate thermal stress of the various structures.

CTE is the main factor for stress distribution on the ELO GaN / diamond sample which is itself temperature dependent. For modelling purposes, the sample is initially assumed to be at the GaN growth temperature of ~ 1030°C and then cooled to room temperature. Because the temperature range is large, to properly calculate the thermal stress it is necessary to use the temperature dependent CTEs as shown in Figure 31 instead of applying a single CTE value throughout the whole temperature range. Based on the relative differences in magnitude of thermal expansion the stress level of all involved materials at a given temperature can be comparatively estimated.

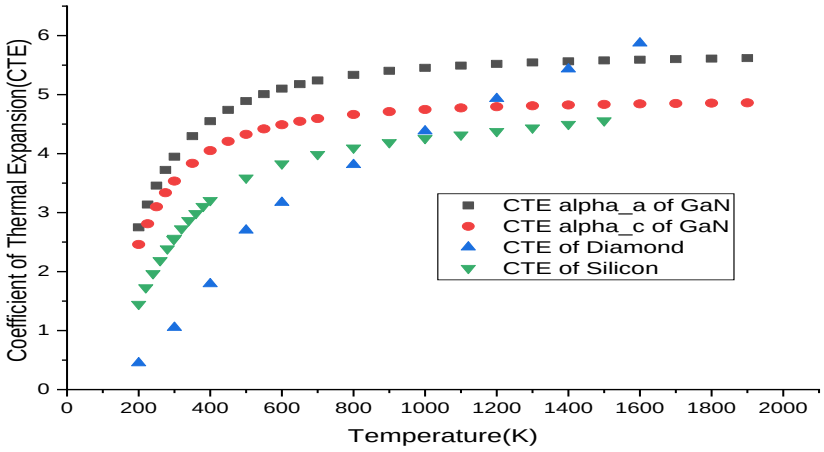

Figure 31: Temperature dependent CTEs of GaN, diamond and silicon [39-41].

6.4.1 Stress on GaN and Diamond on Fully Coalesced ELO Structure

The modelling approach was discussed in section 5.4.5. Here the focus is on the modelling result and comparison to the experimental results. For simplicity the AlGaN, AlN, SiN_x and GaN layers below the diamond stripes were replaced by a single equivalently thick GaN layer, as shown in Figure 32. Because of this approximation, in the non-diamond (regrown GaN on bottom GaN) regions the simulated stress will be less than it would be had all the constituent intermediate layers been included. However, since the focus of this thesis is on the ELO GaN and diamond region, the idealized structure is sufficient to describe the stress distribution as the differences in the stress parameters for the underlying III-Nitride layers is significantly less than the CTE differences of GaN, diamond, and silicon (Figure 32).

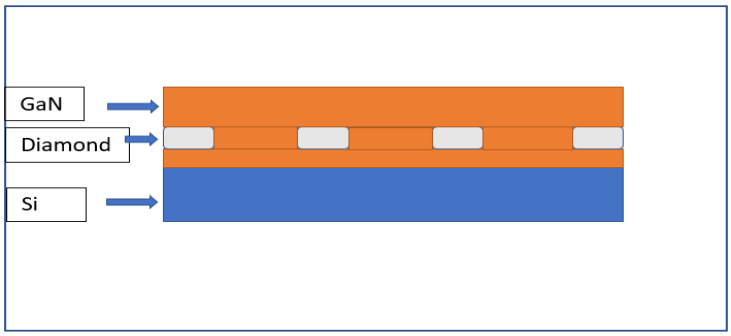

Figure 32: ELO GaN on diamond stripe perfectly coalesced structure for the initial model.

The cause of stress is mainly due to the insertion of the diamond stripes located within the GaN so the stress is maximum near the diamond stripe regions. As the distance from diamond increases the stress decreases as shown in the cross section plots from the COMSOL modelling in Figure 33. Since GaN has higher CTE than diamond, GaN has tensile stress and diamond is compressed. The presence of cracking on the top ELO surface on some structures verifies the extensive tensile stress on the ELO GaN layer. Fundamentally, this tensile stress originates from the silicon substrate that contracts slower than free-standing GaN, as the temperature decreases from 1030°C growth temperature to ambient room temperature, as seen in Figure 33. The stress along the cut lines (black horizontal dashed lines) illustrated in Figure 33 was examined. As shown in Figure 34 the GaN stress is maximum just above the diamond while the non-diamond region has comparatively lower stress. This is due to the lower CTE of diamond than silicon. Diamond contracts more slowly than silicon so it enhances the tensile stress of the overgrown GaN. The ELO and window GaN has close proximity to diamond and farther away from Si which is an important factor leading to the higher stress in the overgrown GaN and the stress relaxation with distance away from the diamond stripe. The stress accumulation at the edge of the diamond stripes creates spikes in the GaN stress at the lower and upper edges as seen in Figure 34. One critical outcome of this simulation is that the GaN coalescence has a major impact on the stress state in the structure. The simulated geometry in Figure 34 does not included an uncoalesced GaN

void and, hence, the GaN stress is not comparable. But interestingly the diamond modelling stress is very close to the experimental stress presented in Figure 34. Both the experimental and modelling stress data for diamond indicate a maximum stress magnitude of ~ -1.10 GPa at the center of the diamond stripes while the stress is decreasing towards the diamond edge. The GaN by the side of diamond stripes has less stress as does the diamond away from the center.

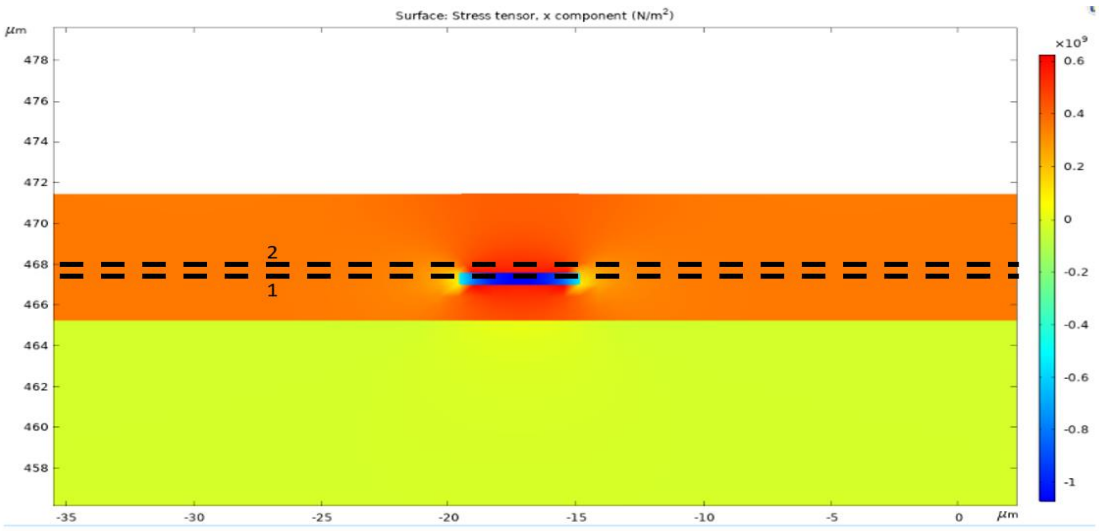

Figure 33: Cross-section plot of simulated stress on idealized coalesced GaN ELO structure.

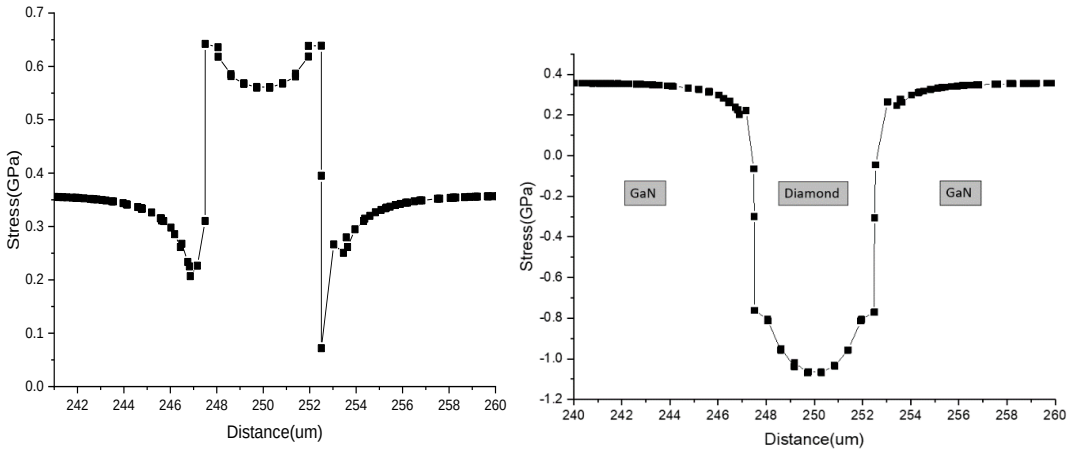

Figure 34: GaN stress (Left) and Diamond stress (Right) obtained on idealized coalesced ELO GaN from COMSOL modelling. The right-hand panel indicates the diamond stress between 247.5 μm to 252.5 μm, while on either side of this region the window GaN simulated stress is indicated.

6.4.2 Stress on GaN and Diamond with Void Just Above Diamond on Coalescence Region

The modified geometry shown in Figure 35 is a more realistic representation of the studied structure as the samples generally have voids near the coalescence region. Because of the void, the GaN wings can relax freely thereby decreasing the stress at the coalescence region. The bottom left graph in Figure 36 shows the stress decreasing near the void, up to around 1 μm from the void. Unlike the diamond stress in perfectly coalesced ELO GaN the diamond stress just below the void has a sharp spike in tensile stress in the diamond instead of compressive stress, however, the rest of the diamond stripe stress is still compressive in nature as shown in Figure 36 (right). The reason for this spike in compressive stress is stress accumulation at the free edge of diamond near the void.

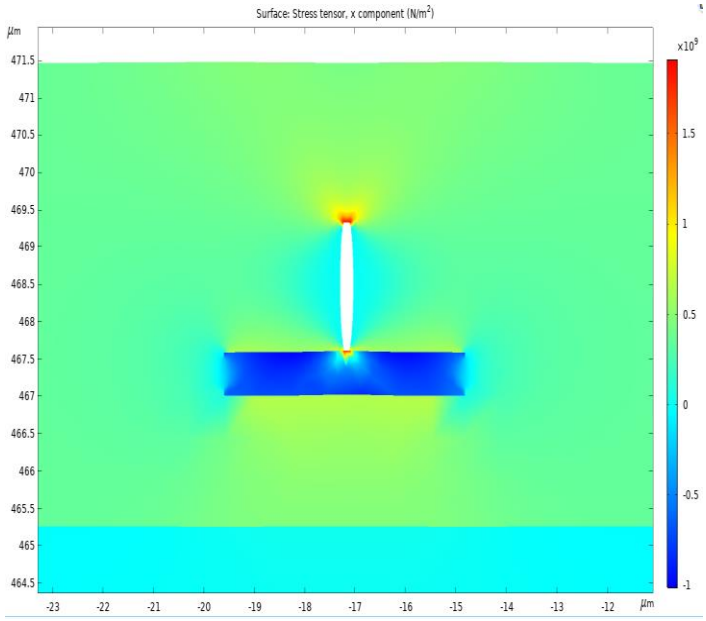

Figure 35: Simulated ELO GaN sample including a void at the coalescence region.

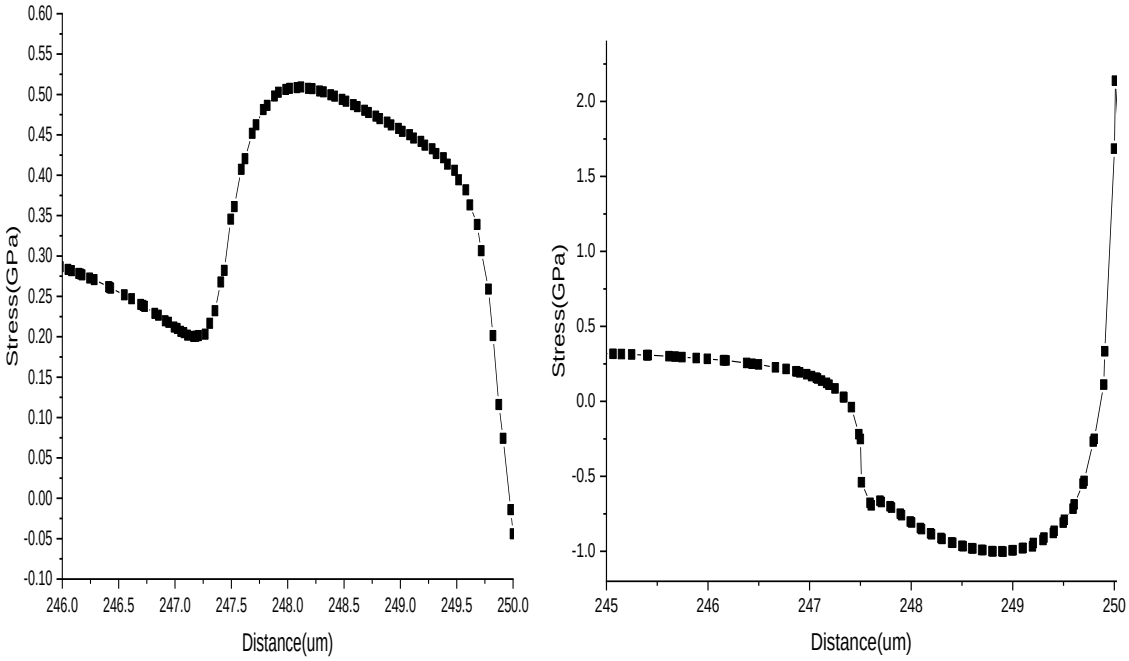

Figure 36: Stress distribution of ELO GaN with a void at the coalescence region (left graph) and diamond stress pattern (right graph). The graphs are from left of the stripe and toward the center of the void. The right half will be similar due to symmetry.

6.4.3 Stress on GaN and Diamond on Non-Coalesced ELO Structure

This model (Figure 37) is representative of a structure in which the ELO GaN does not coalesce. Such non-coalescence is representative of insufficient lateral GaN growth. For the samples studied, all 10 μm diamond stripes did not coalesce while 5 μm coalescence was intermittent. To model stress relaxation, the uncoalesced structure was centered above the 5 μm diamond stripe keeping all the parameters and conditions the same as explained above. The GaN wings are not coalesced which allows the top ELO GaN surface to relax along the center of the diamond surface due to the presence of free GaN wings. This sharply decreasing stress can be visualized with Figure 38 (left graph) which is one of the contributing factors in decreasing the stress in ELO GaN as observed in the experimental Raman measurements. Similar to the sample with a void at the coalescence region, a sharp tensile stress peak is observed at the diamond top surface near the

cleaved GaN which is due to stress accumulation at the edge of the GaN wings. Away from the center, the diamond stress is compressive which is similar to other structures modelled, shown in sections 6.4.1 and 6.4.2.

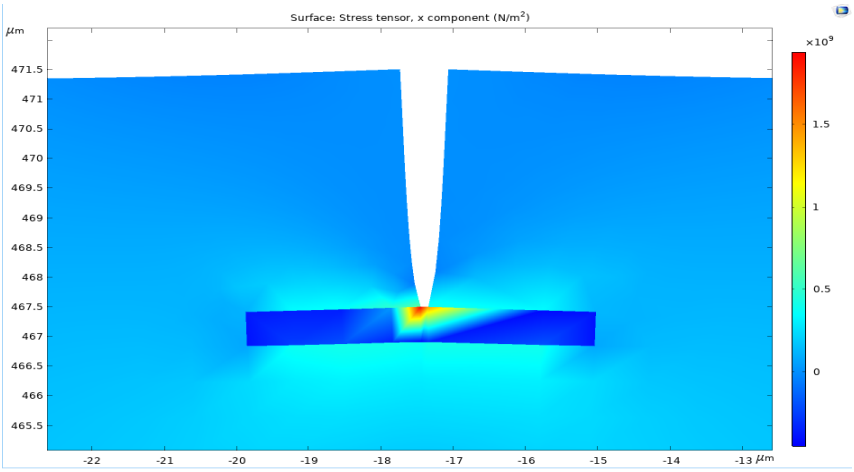

Figure 37: Surface stress plot on the ELO sample with a cleavage on the coalescence region.

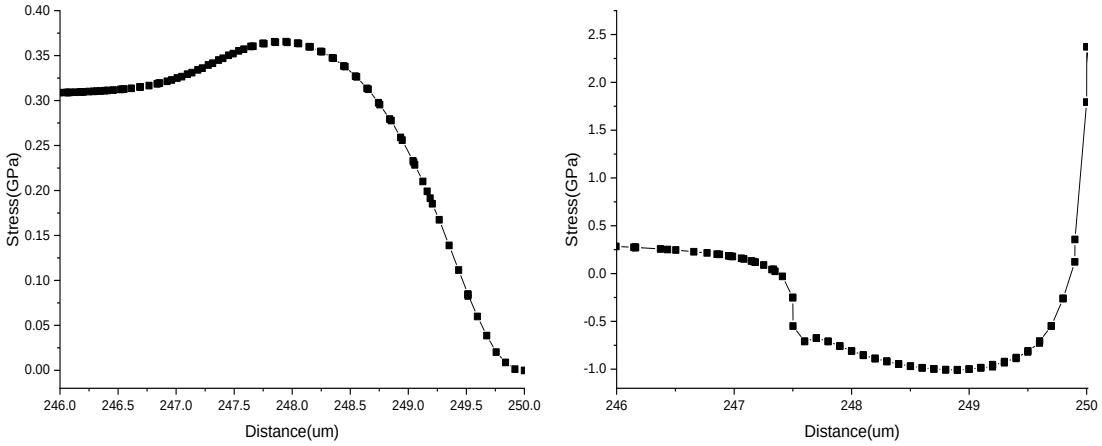

Figure 38: Stress distribution of ELO GaN just above the diamond stripes with a non-coalesced geometry (left graph) and diamond stress pattern (right graph). The graphs are from left of the stripe and toward the center of the void. The right half will be similar due to symmetry.

6.4.4 ELO GaN with Void at Coalescence Region and Gaps in between GaN and Diamond

This model is considered the most accurate as it represents the coalescence void as well as gaps between ELO GaN and diamond that are observed in TEM (Figure 30).

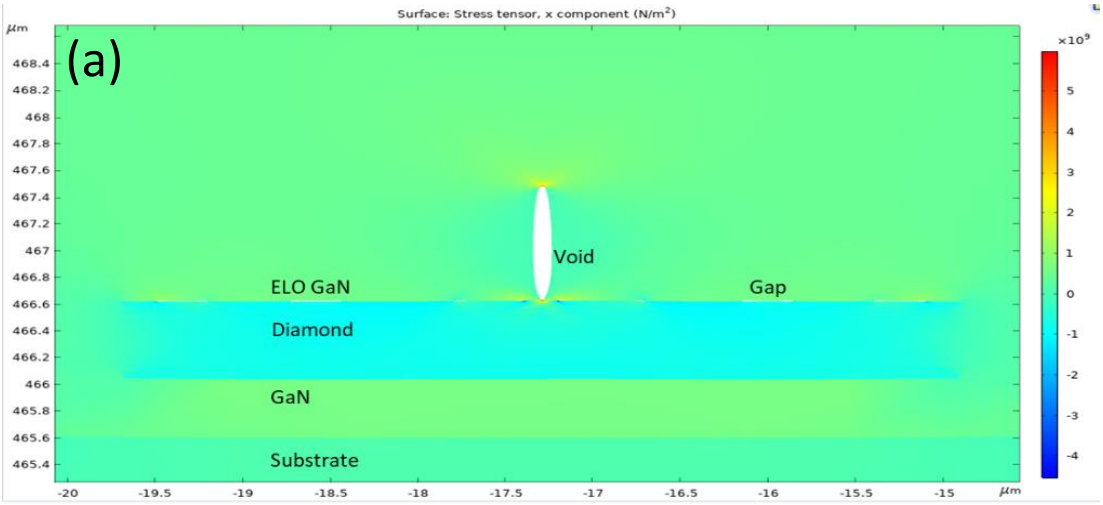

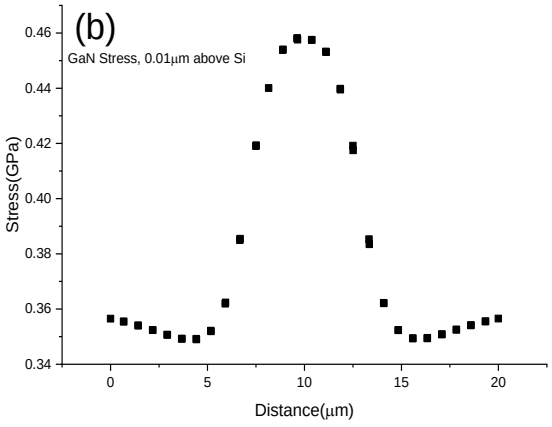

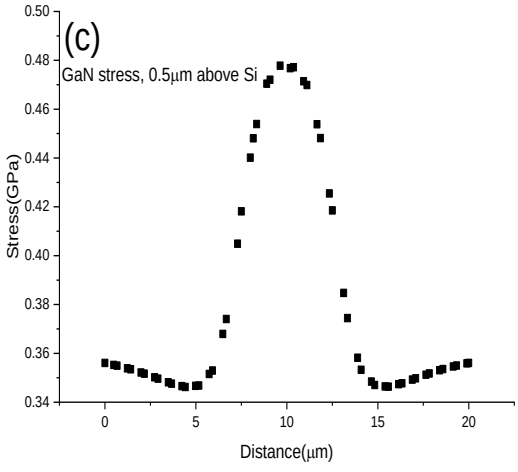

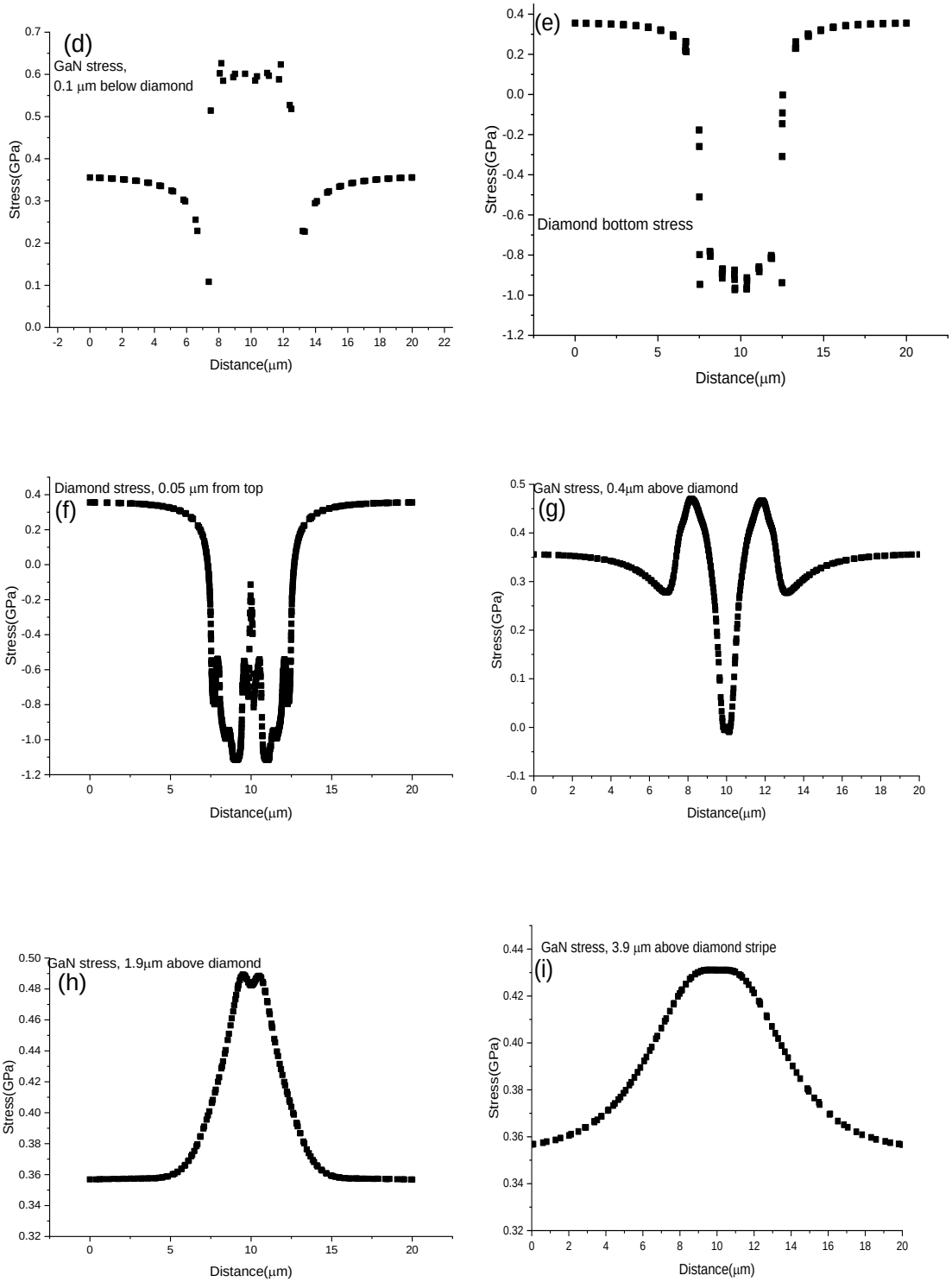

Figure 39. COMSOL simulation. (a) Cross section with void at the coalescence region and gaps between GaN and diamond stripe, (b)-(d) GaN stress below the diamond stripe, (e) and (f) diamond stress and (g)-(i) are the GaN stress above the diamond. Vertical cut lines are as indicated on the graphs.

The graphs in Figure 39 show the evolution of stress starting from the Si-GaN interface up to the top GaN surface. Initially the GaN stress is due to CTE mismatch with Si (Figures 39(b) and (c)). Approaching the diamond stripe, the underlying GaN stress becomes impacted by the CTE mismatch with diamond (Figure 39(d)). The stress at the bottom and top of the diamond stripe are both compressive. Moving into the ELO GaN region, interestingly, as shown in Figure 39(g), there is zero stress in the GaN near the coalescence region while the stress is increasing away from the coalescence region. The zero stress at the coalescence region is because of the presence of the void. The result shown in Figure 39(g) gives insight that averaging the Raman stress data throughout the depth of focus can result in lower nonzero stress at the coalescence region.

Summarizing the modelling results, the GaN stress simulation cannot fully reflect the experimental stress results, however, there is strong evidence of decreasing stress in ELO GaN due to the presence of voids and/or cleavage between GaN wings. However, the impact of void / cleave is not sufficient to explain the measured lower stress in ELO GaN in comparison to the coherently grown GaN. This is because the overgrown GaN, especially at the coalescence region, is highly defective and is thought to be one of the major factors for lower stress in the ELO region. Furthermore, the evidence of carbon doping as seen in TEM measurements may also contribute to decreasing the stress. Another important reason is that the GaN-diamond contact is not uniform but, instead, gaps between GaN and diamond are observed in the TEM data. The defect density, threading dislocation distribution and impurities cannot readily be simulated with COMSOL explaining the main difference between the experimental Raman results and simulations.

On the other hand, the experimental results and COMSOL modelling of the diamond stress generally agree. Following the diamond stress pattern as observed by Ahmed et.al. [9], the stress on 5 μm diamond stripes should be lower than what was obtained experimentally if there was not ELO GaN. Hence, the higher compressive stress in the 5 μm diamond stripe is due to the ELO

GaN above the diamond. Thus, the effect of ELO GaN on the diamond stress distribution may be estimated and, thus, explain the higher stress in diamond stripes with ELO GaN.

7. FUTURE RESEARCH

7.1 Need for More Lateral Overgrowth

Significant voiding was observed at the coalescence region above the 5 μm diamond stripes thereby requiring optimization of the growth condition to achieve higher GaN lateral growth rate. Higher lateral growth rate may also reduce the presence of gaps in between GaN and diamond. However, minimizing the presence of gaps will probably require optimizing other GaN and diamond growth conditions as well as lateral growth rate. Based on the MOCVD system's capability the TMG flow rate, NH_3 flow rate, the ratio between them, and temperature and pressure of the growth environment need to be optimized to achieve the best ELO method giving better coalescence between the wings and more uniform GaN-diamond contact. Another way of improving the ELO growth mechanism may be modifying the process gas flow in such a way that the ratio favors the vertical growth until GaN is growing through the window region and then modifying the ratio to enhance the lateral growth which hasn't been done before for this project.

7.2 Modified ELO GaN to Improve GaN Quality

The ELO GaN above the diamond stripes has superior crystal quality than epitaxially grown GaN. However, there are some dislocations present, and bending from the window regions, as evidenced by TEM images. Because the defects in GaN tend to act as non-radiative recombination sites, carrier scattering centers and leakage current path, it is better to minimize them to improve device performance. One way of reducing dislocations on the epitaxially grown GaN is by multiple bending and blocking the threading dislocations as shown in Figure 40 which should give the best GaN quality. In addition to improved GaN, the diamond stripes should act as a heat spreader for the thermal management of the HEMT structure.

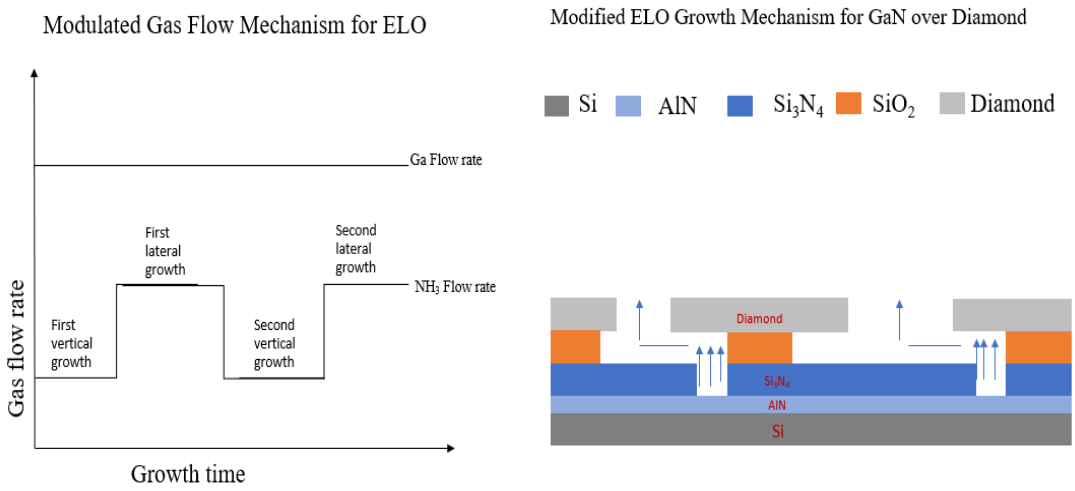

Figure 40: Modified ELO growth mechanism to get the best GaN quality.

7.3 Determination of Thermal Boundary Conductance (TBC) between GaN and Diamond

GaN directly grown over diamond without an interfacial layer has been achieved for the first time so the TBC should be high. The determination of TBC on such a unique structure is extremely important to estimate the effectiveness on the thermal management of the HEMT structure. One common technique to determine TBC is Time Domain Thermo Reflectance (TDTR) that may be conducted via collaboration with other universities (such as Georgia Tech).

7.4 Development of HEMT over Best Quality GaN-Diamond Structure

The final objective is thermal management of the GaN HEMT structure, so it needs to be grown on top the best quality GaN-diamond substrate. Thus formed, the HEMT structure should demonstrate the most efficient HEMT device because of the combination of low defect GaN attached with high TBC to highly thermally conductive diamond.

APPENDIX SECTION

Appendix 1

Effect of carbon dopant on GaN stress

Stress relaxation of GaN due to Si doping as observed by Lee et al. [51] showed increased FWHM with increasing Si doping concentration, hence, this observation indicates that stress relaxation could be related to the increased crystal imperfection. Decreasing trend of c-lattice constant was observed with the increasing Si doping concentration because the Si was incorporated on Ga site of GaN crystal, but this increased strain energy was negligible and compensated by antibonding state of additional electrons, giving the relaxed Si doped GaN. Going through various literatures [52-57] related to GaN doping by carbon atom suggested that C is mostly incorporated on the N site in GaN lattice. Since the Carbon and Nitrogen size are very close, the strain energy ($= \frac{\Delta c}{c_o}$, c is the height of GaN crystal) induced due to C incorporation on N site is very negligible. The exact mechanism of defects induced by carbon incorporation in GaN is still unknown, however one of the most promising reasons of low stress above the diamond stripes is assumed to be due to carbon induced defects. Unlike threading dislocations in the non-diamond region, no dislocations were observed to originate above the diamond stripes via TEM observation on the region of interest, however there is a possibility of diamond induced misfit dislocation near the GaN-diamond interface as explained by I.-H. Lee et al. [51] in the stress measurement study of Si doped GaN thin films. This type of misfit dislocation may also have some contribution at least on some of the structures to relax the GaN stress above the diamond stripes. Carbon doping on GaN was also done by Gogova et al.[45] and they claim that at high temperature ammonia reacts with carbon to form pseudo halide hydrogen cyanide(HCN).

$C(s) + NH_3(g) \rightarrow HCN(g) + H_2(g)$

The pyrolysis of TMG gives dimethylgallium (DMG) which on subsequent pyrolysis gives monomethylgallium (MMG) as follows[33]:

$(CH_3)_3Ga \rightarrow (CH_3)_2Ga + CH_3$

$(CH_3)_2Ga \rightarrow (CH_3)\ Ga + CH_3$

Thus, formed hydrogen cyanide (HCN) reacts with MMG to form volatile Gallium compounds such as Gallium monocyanide (Ga (CN)) which decomposes thermally to deposit crystalline GaN and carbon. This carbon plays the role of dopant and in most cases this carbon replaces the Nitrogen site acting as a p-type impurity in epitaxial GaN.

$Ga(CH_4)\ (g) + HCN(g) \rightarrow Ga(CN)(g) + CH_4(g)$

$Ga(CN)(g) \rightarrow GaN(s) + C\ (s)$

Or the chemical reaction may happen as follows,

$Ga(CN)(g) + NH_3(g) \rightarrow GaN(s) + HCN(g) + H_2(g)$

Appendix 2

The vertical stress distribution close to void in coalescence region

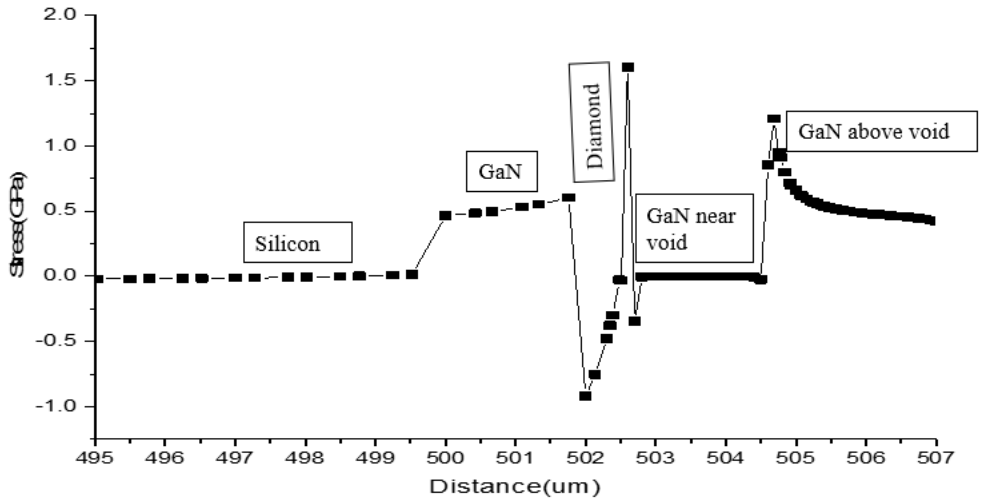

Figure I. Vertical Scan throughout the depth of sample near the void in ELO GaN with a small void near the coalescence region.

To see the stress distribution along the depth of the sample a vertical cutline was taken along the thickness of the modelling geometry near the void and the stress distribution is shown in Figure 37. Silicon thickness spans 0 to 500 µm where the stress is minimal due to this comparatively huge thickness. After that, the GaN layer is present until 502 µm which has higher tensile stress. Following GaN, the diamond begins, and compressive stress is observed up to the top diamond surface near the void where the diamond shows very high tensile stress breaking the stress pattern. Starting from 502.6 µm to 504.5 µm, while in the void, the stress graph is nearly zero. Above the void, the GaN stress decreases moving towards the free top surface on the far right of Figure 45.

Appendix 3

Useful MATLAB programs for Raman data analysis

The MATLAB files shared below are examples only, I do not expect they can be used directly. Based on the location of text file, text file property, Raman system (number of pixels in full chip, wavelength), analysis window, binning size and error of interest for the calculation you need to customize these files before using them.

1.Loading the data file.

```
clear all;



path='C:\Users\gauta\Desktop\Output directory\5micronfeaturesof1by1_fullchip_174' %file path minus extension

LoadExtension='_1.txt';

SaveExtension='Vars';

filename1=strcat(path,LoadExtension)

filename2=strcat(path,SaveExtension)

fid = fopen(filename1, 'rt');

data = textscan(fid,'%s %f %f %f','headerlines', 1, 'delimiter', ',');

fclose(fid);

chr=data{1}{1};
```

```
chr=erase(chr,'"Wavelength"');

C = textscan(chr,'%f');

M=[];

H=M;

for n= 1:399

      chrr=data{1}{3+n};

   chrr=erase(chrr,'"1 "');

   D = textscan(chrr,'%f');

   D{1}(1)=[];

   A=cat(2,C{1},D{1});

   sensitivity=0.041;

    M=cat(2,M,A(:,2));

 end

%% Wavenumber Capture

W=str2num(chr);

MaxWave=max(W)

CCDStep=(W(1)-W(1340))/1340

H=hampel(M,5);
```

```
figure('name',"Raw Data")

waterfall(M);

figure('name',"Hempel Outlier Filter 5 units")

waterfall(H);

save(filename2,'H','M','MaxWave','CCDStep');
```

2. Analysis of data file

```
clear all;

Peaks=[];

AA=[];K=[];

%%   Load Files

path='C:\Users\gauta\Desktop\Friday_Small_1180302B\5by5PerfectlyCoalescedFriday_1180302
B431' %file path minus extension

LoadExtension='Vars';

SaveExtension='Analysis';

filename1=strcat(path,LoadExtension)

load(filename1,'H','M','MaxWave','CCDStep');

filename2=strcat(path,SaveExtension)
```

```
%% Expected Peak Locations

AproxX=[567 1333];

correction=0;

%%  CCD Setup %%

figure

waterfall(H);

step=CCDStep;       %CCD datapoint separation

t=MaxWave;          %Max Wavenumber

  for n= 1:1340

XX(n)=t;  %X axis values

t=t-(step+correction);

end

%%  Main Analysis

max=size(AproxX);   % stablishes the total number of peaks to find and fit

figure;

hold on;

for n=1:399         %First Loop runs through all the pixel strips

    A=H(:,n);
```

```
Z(n)=n*.1;

 for peakNum=1:max(2)        %This Loop runs through all the peaks per strip and fits them



 [fitresult, gof] = LorentzFit(XX, A, (AproxX(peakNum)));

    errors=confint(fitresult);

    PeakPositions(peakNum,n)=fitresult.PP;

 PPerr(peakNum,n)=(errors(2,1)-errors(1,1))/3.92;

 Widths(peakNum,n)=fitresult.w;

 Werr(peakNum,n)=(errors(2,4)-errors(1,4))/3.92;

    Intensities(peakNum,n)=fitresult.a;

 Ierr(peakNum,n)=(errors(2,2)-errors(1,2))/3.92;

        for i = 495:1460

    L(i)=(fitresult(i)-fitresult.back);

           end

 K{peakNum}=L;

 end

    KK=K{1};

 if max(2)>1
```

```
            for n=2:max(2)
          KK=KK+K{n};
       end
   end
   AA=cat(1,AA,KK);
plot(KK);
end
figure;
waterfall(AA);
for peakNum=1:max(2)
   figure('name',"Peak position as function of position for Peak at "+AproxX(peakNum)+"
wavenumber")
  errorbar(Z,PeakPositions(peakNum,:),PPerr(peakNum,:));
     figure('name',"Linewidth as function of position for Peak at "+AproxX(peakNum)+"
wavenumber")
  errorbar(Z,Widths(peakNum,:),Werr(peakNum,:));
```

```
  figure('name',"Intensity as function of position for Peak at "+AproxX(peakNum)+"
wavenumber")
  errorbar(Z,Intensities(peakNum,:),Ierr(peakNum,:));
end
filename2
save(filename2,'AA','XX','PeakPositions','PPerr','Widths','Werr','Intensities','Ierr')
%% FUNCTIONS
function [fitresult, gof] = LorentzFit(XX, A, aproxX)
%CREATEFIT(XX,A)
%  Create a fit.
%  Data for 'untitled fit 1' fit:
%      X Input : XX
%      Y Output: A
%  Output:
%      fitresult : a fit object representing the fit.
%      gof : structure with goodness-of fit info.
%  See also FIT, CFIT, SFIT.
%  Auto-generated by MATLAB on 04-Feb-2019 11:25:46
```

```
%% Fit: 'untitled fit 1'.

[xData, yData] = prepareCurveData( XX, A );

% Set up fittype and options.

% ft = fittype( '(a/(p*((x-PP)^2 + 1))+b)+background', 'independent', 'x','dependent', 'y' );

% opts = fitoptions( 'Method', 'NonlinearLeastSquares' );

% opts.Display = 'Off';

% opts.StartPoint = [aproxX 0.99 0.78 360 4];

% ft = fittype( '(a/(p*((x-PP)^2 + 1)))+back', 'independent', 'x', 'dependent', 'y' );

% opts = fitoptions( 'Method', 'NonlinearLeastSquares' );

% opts.Display = 'Off';

% opts.StartPoint = [aproxX 0.978732191344639 370 4];

ft = fittype( 'back+(2*a/3.1416)*(w/(4*(x-PP)^2+w^2))', 'independent', 'x', 'dependent', 'y' );

opts = fitoptions( 'Method', 'NonlinearLeastSquares' );

opts.Display = 'Off';

pplow=aproxX-5;

pphigh=aproxX+5;

opts.Lower = [pplow 0 100 0];

opts.StartPoint = [aproxX .97 150 8];
```

```
opts.Upper = [pphigh Inf Inf 8];

%           [pp   A  back  width]

% Fit model to data.

[fitresult, gof] = fit( xData, yData, ft, opts );

%Plot fit with data.

% figure( 'Name', 'lorentz fit' );

% h = plot( fitresult, xData, yData );

% legend( h, 'A vs. XX', 'untitled fit 1', 'Location', 'NorthEast' );

% % Label axes

% xlabel XX

% ylabel A

% grid on

end

function [fitresult, gof] = createSpline(XX, A)

%CREATEFIT(XX,A)

%  Create a fit.

%  Data for 'untitled fit 1' fit:

%      X Input : XX
```

```
%      Y Output: A
%  Output:
%      fitresult : a fit object representing the fit.
%      gof : structure with goodness-of fit info.
%  See also FIT, CFIT, SFIT.
%  Auto-generated by MATLAB on 12-Mar-2019 12:24:46
%% Fit: 'untitled fit 1'.
[xData, yData] = prepareCurveData( XX, A );
% Set up fittype and options.
ft = fittype( 'smoothingspline' );
opts = fitoptions( 'Method', 'SmoothingSpline' );
opts.Normalize = 'on';
opts.SmoothingParam = 0.9999999;
% Fit model to data.
[fitresult, gof] = fit( xData, yData, ft, opts );
% Plot fit with data.
% figure( 'Name', 'untitled fit 1' );
% h = plot( fitresult, xData, yData );
```

```
% legend( h, 'A vs. XX', 'untitled fit 1', 'Location', 'NorthEast' );
% % Label axes
% xlabel XX
% ylabel A
% grid on
end
function [fitresult, gof] = createFourFit(CC)
%CREATEFIT(CC)
%  Create a fit.
%  Data for 'untitled fit 1' fit:
%      Y Output: CC
%  Output:
%      fitresult : a fit object representing the fit.
%      gof : structure with goodness-of fit info.
%  See also FIT, CFIT, SFIT.
%  Auto-generated by MATLAB on 12-Mar-2019 13:06:15
%% Fit: 'untitled fit 1'.
[xData, yData] = prepareCurveData( [], CC );
```

```
% Set up fittype and options.

ft = fittype( 'fourier6' );

opts = fitoptions( 'Method', 'NonlinearLeastSquares' );

opts.Display = 'Off';

opts.Robust = 'Bisquare';

opts.StartPoint = [0 0 0 0 0 0 0 0 0 0 0 0 0 0.012];

% Fit model to data.

[fitresult, gof] = fit( xData, yData, ft, opts );

% Plot fit with data.

% figure( 'Name', 'untitled fit 1' );

% h = plot( fitresult, xData, yData );

% legend( h, 'CC', 'untitled fit 1', 'Location', 'NorthEast' );

% % Label axes

% ylabel CC

% grid on

End
```

Appendix 4

COMSOL Simulation

Screenshots of COMSOL simulation with different parameters, and conditions used for simulations.

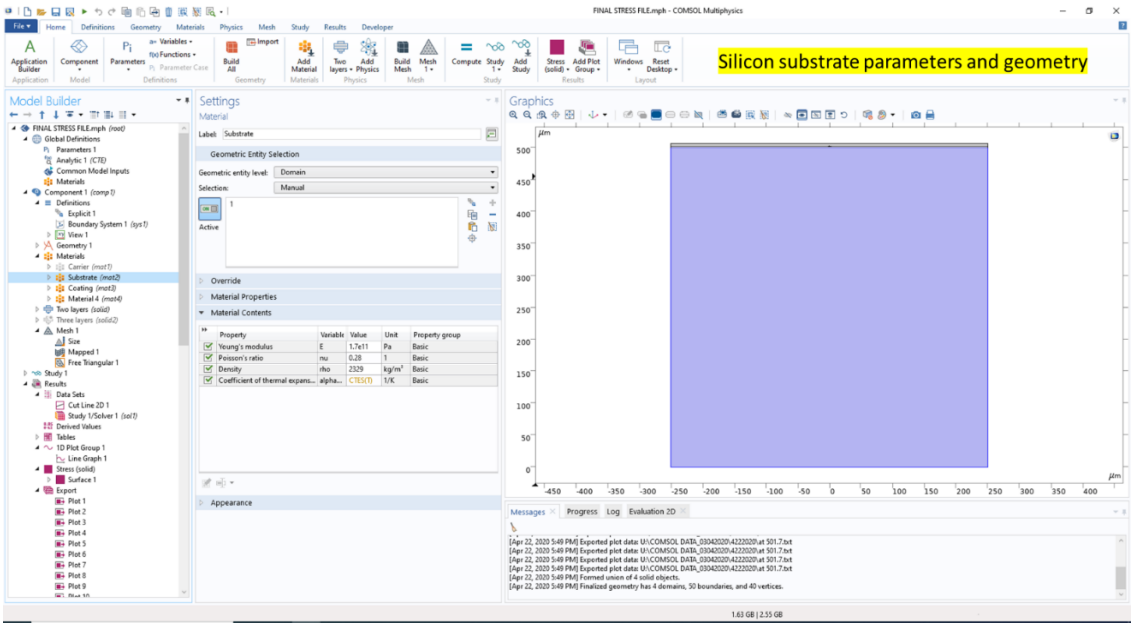

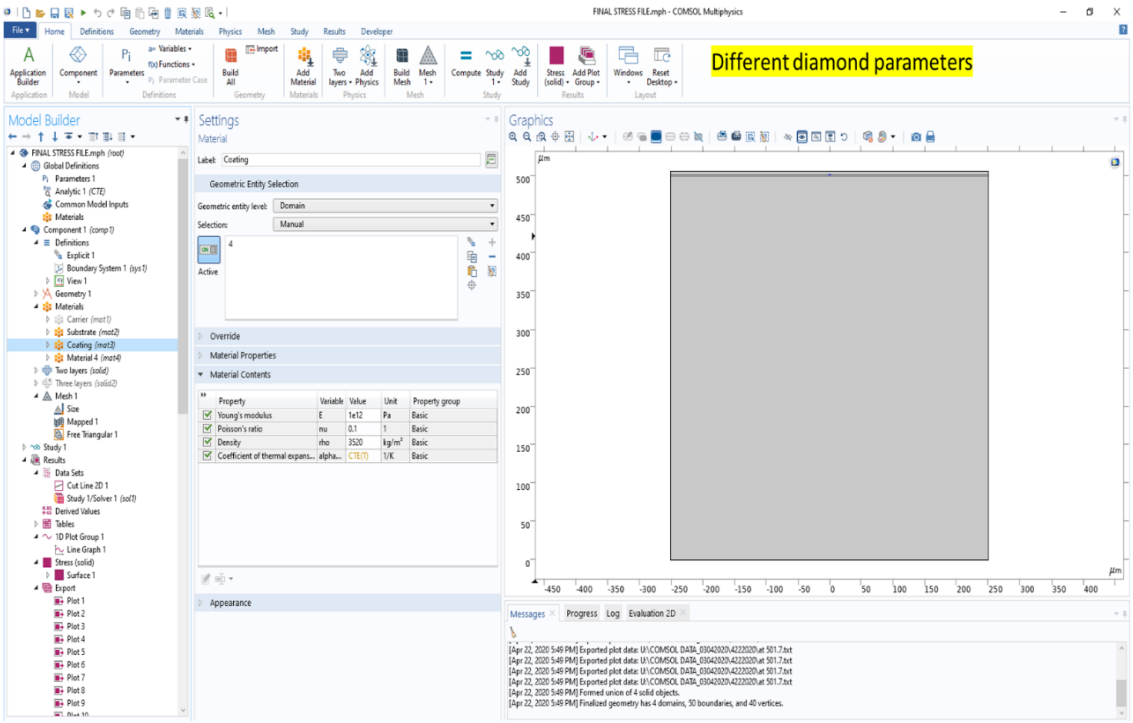
FINAL STRESS FILE.mph - COMSOL Multiphysics
Different diamond parameters
Model Builder
Settings
Material
Label: Coating
Geometric Entity Selection
Geometric entity level: Domain
Selection: Manual
Override
Material Properties
Material Contents
Property | Variable | Value | Unit | Property group
Young's modulus | E | 1e12 | Pa | Basic
Poisson's ratio | nu | 0.1 | 1 | Basic
Density | rho | 3520 | kg/m³ | Basic
Coefficient of thermal expans... | alpha... | CTE(T) | 1/K | Basic
Appearance
Graphics
Messages
Progress
Log
Evaluation 2D

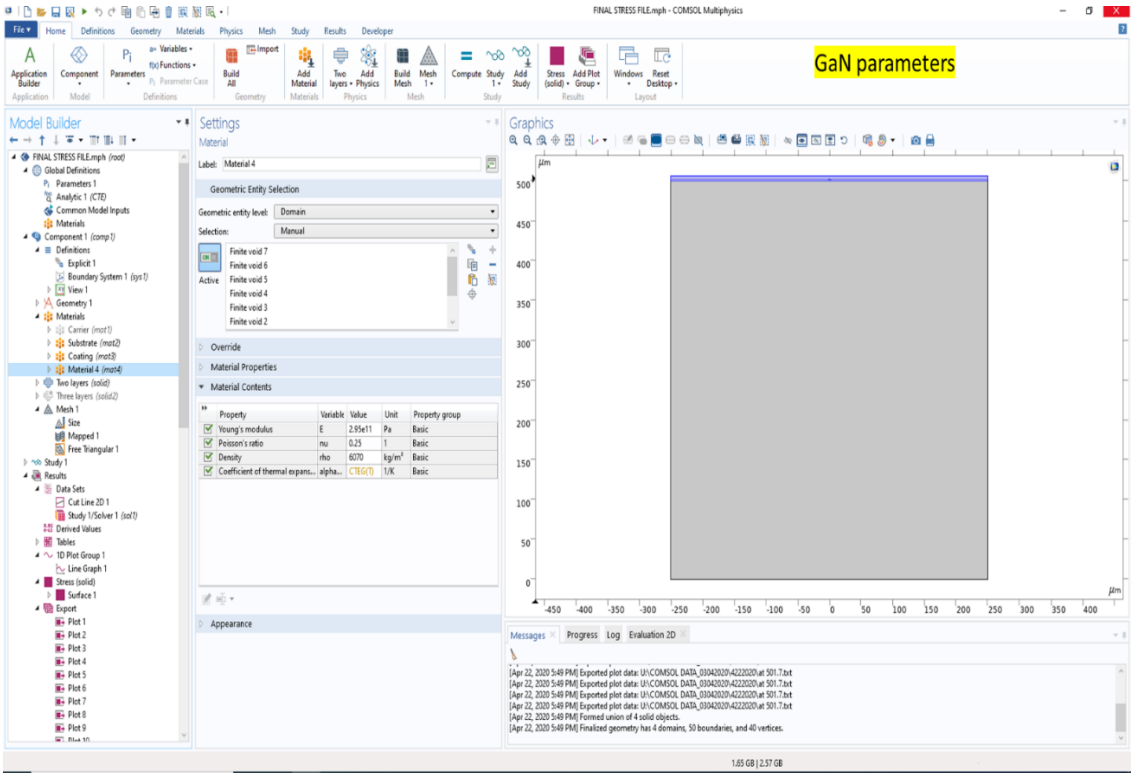
FINAL STRESS FILE.mph - COMSOL Multiphysics
GaN parameters
Model Builder
Settings
Material
Label: Material 4
Geometric Entity Selection
Geometric entity level: Domain
Selection: Manual
Override
Material Properties
Material Contents
Property | Variable | Value | Unit | Property group
Young's modulus | E | 2.95e11 | Pa | Basic
Poisson's ratio | nu | 0.25 | 1 | Basic
Density | rho | 6070 | kg/m³ | Basic
Coefficient of thermal expans... | alpha... | CTE(T) | 1/K | Basic
Appearance
Graphics
Messages
Progress
Log
Evaluation 2D

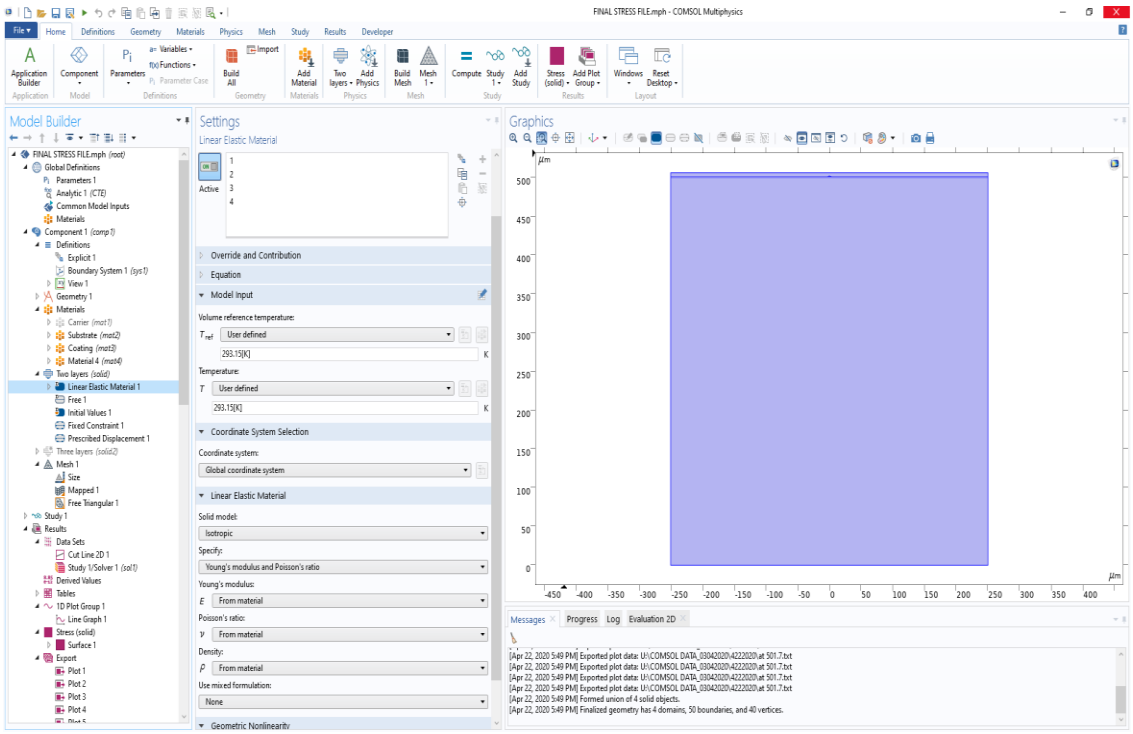
FINAL STRESS FILE.mph - COMSOL Multiphysics
Model Builder
Settings
Linear Elastic Material
Graphics
Messages
Progress
Log
Evaluation 2D

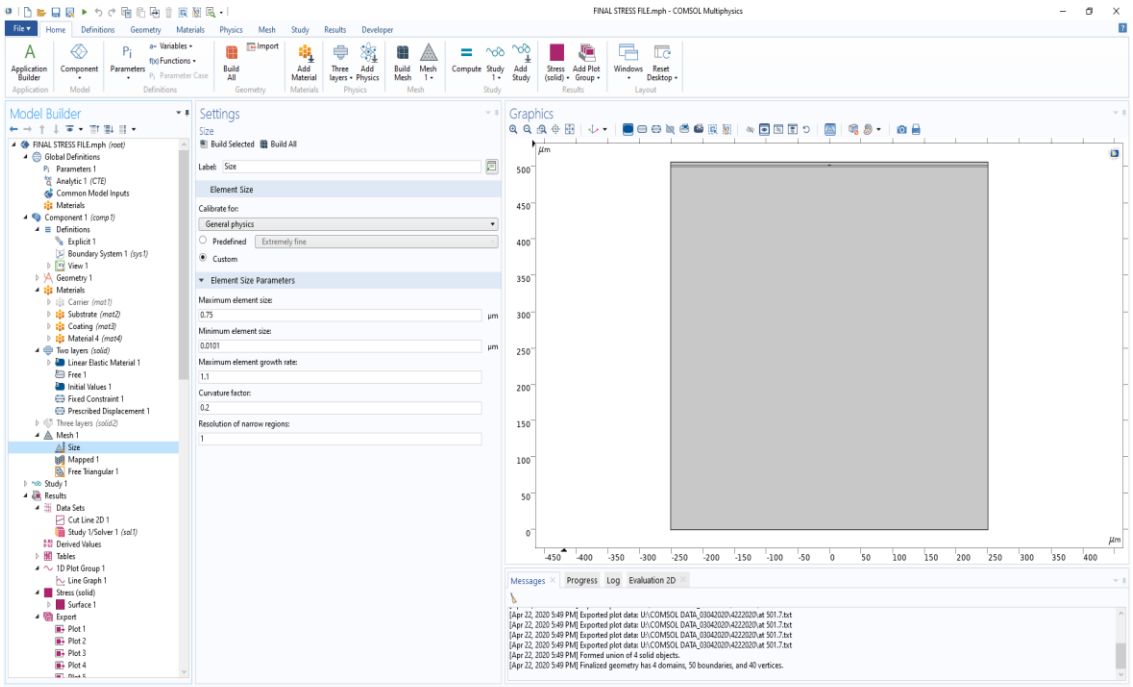
FINAL STRESS FILE.mph - COMSOL Multiphysics
Model Builder
Settings
Size
Graphics
Messages
Progress
Log
Evaluation 2D

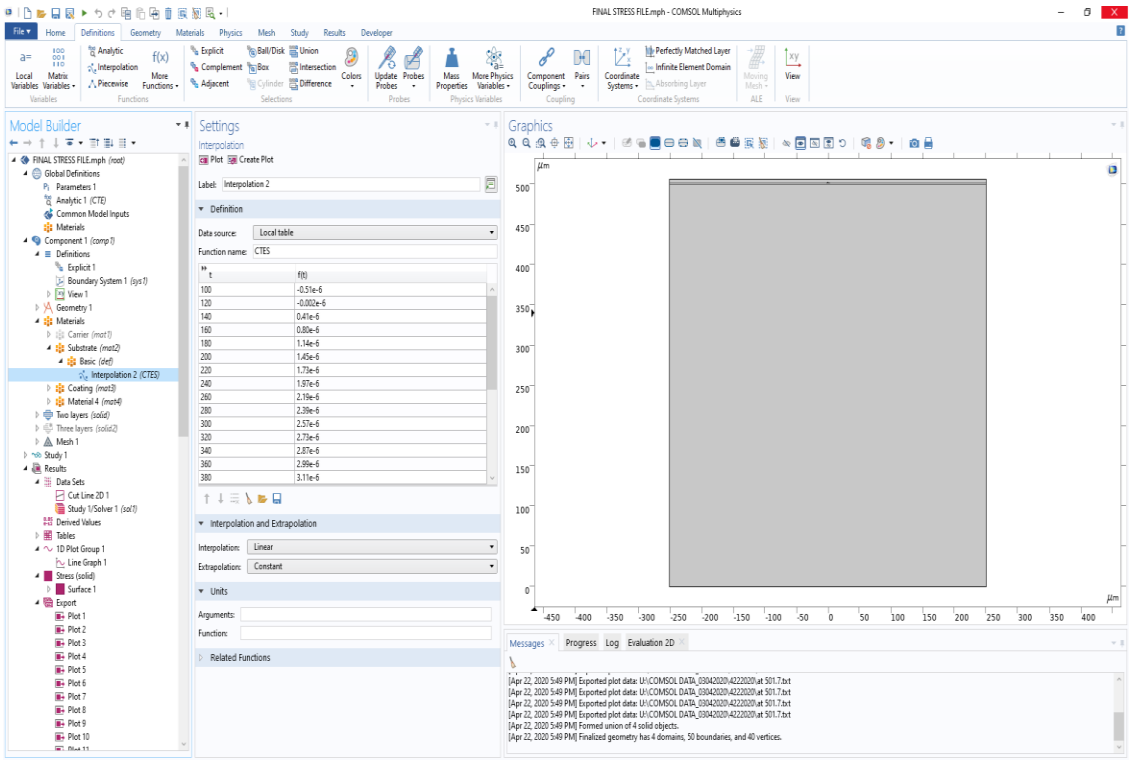
FINAL STRESS FILE.mph - COMSOL Multiphysics
Model Builder
Settings
Interpolation
Label: Interpolation 2
Definition
Data source: Local table
Function name: CTES
Interpolation and Extrapolation
Interpolation: Linear
Extrapolation: Constant
Units
Related Functions
Graphics
Messages
Progress
Log
Evaluation 2D

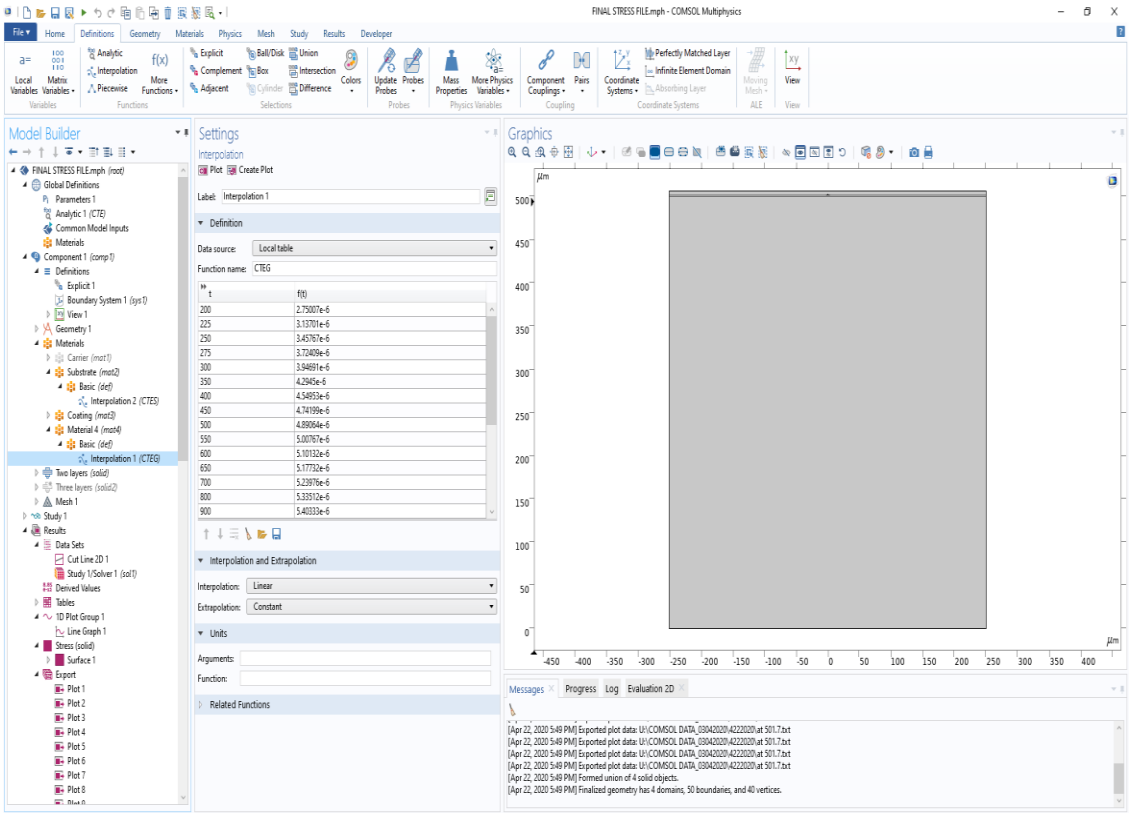
FINAL STRESS FILE.mph - COMSOL Multiphysics
Model Builder
Settings
Interpolation
Label: Interpolation 1
Definition
Data source: Local table
Function name: CTEG
Interpolation and Extrapolation
Interpolation: Linear
Extrapolation: Constant
Units
Related Functions
Graphics
Messages
Progress
Log
Evaluation 2D

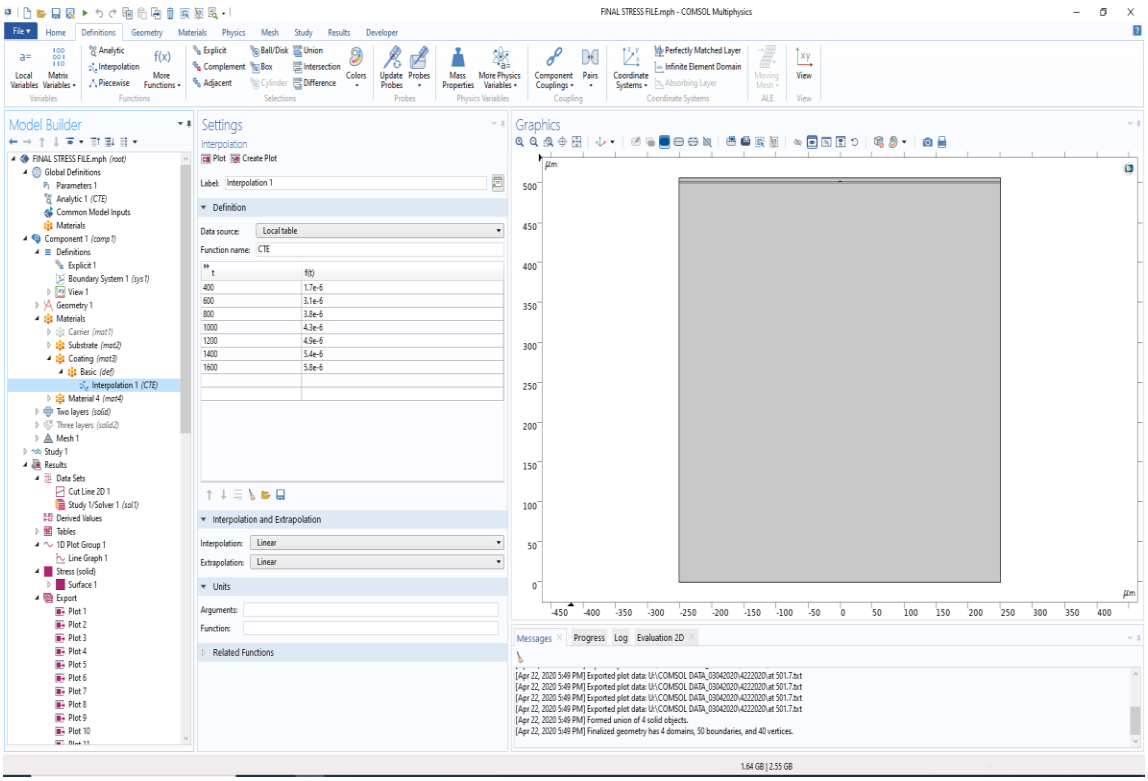
FINAL STRESS FILE.mph - COMSOL Multiphysics
Model Builder
Settings
Interpolation
Graphics
Definition
Interpolation and Extrapolation
Units
Related Functions
Messages
Progress
Log
Evaluation 2D

LITERATURE CITED

[1] R. Ahmed, "Growth and Characterization of Nitride Semiconductors on Chemical Vapor Deposited Diamond," PhD, Material Science Engineering and Commericialization, Texas State University, 2018.

[2] K. HIRAMATSU *et al.*, "Crystalline and optical properties of ELO GaN by HVPE using tungsten mask," *IEICE transactions on electronics*, vol. 83, no. 4, pp. 620-626, 2000.

[3] M. Kuball, M. Benyoucef, B. Beaumont, and P. Gibart, "Raman mapping of epitaxial lateral overgrown GaN: Stress at the coalescence boundary," *Journal of Applied Physics*, vol. 90, no. 7, pp. 3656-3658, 2001.

[4] G. Jessen *et al.*, "AlGaN/GaN HEMT on diamond technology demonstration," in *2006 IEEE Compound Semiconductor Integrated Circuit Symposium*, 2006: IEEE, pp. 271-274.

[5] J. W. Pomeroy *et al.*, "Contactless thermal boundary resistance measurement of GaN-on-diamond wafers," *IEEE Electron Device Letters*, vol. 35, no. 10, pp. 1007-1009, 2014.

[6] R. Quay, *Gallium nitride electronics*. Springer Science & Business Media, 2008.

[7] R. Ahmed, A. Siddique, J. Anderson, C. Engdahl, M. Holtz, and E. Piner, "Selective Area Deposition of Hot Filament CVD Diamond on 100 mm MOCVD Grown AlGaN/GaN Wafers," *Crystal Growth & Design*, vol. 19, no. 2, pp. 672-677, 2019.

[8] A. Siddique *et al.*, "Structure and Interface Analysis of Diamond on an AlGaN/GaN HEMT Utilizing an in Situ SiN x Interlayer Grown by MOCVD," *ACS Applied Electronic Materials*, vol. 1, no. 8, pp. 1387-1399, 2019.

[9] R. Ahmed *et al.*, "Ultraviolet micro-Raman stress map of polycrystalline diamond grown selectively on silicon substrates using chemical vapor deposition," *Applied Physics Letters,* vol. 112, no. 18, p. 181907, 2018.

[10] T. Kozawa, T. Kachi, H. Kano, H. Nagase, N. Koide, and K. Manabe, "Thermal stress in GaN epitaxial layers grown on sapphire substrates," *Journal of applied physics,* vol. 77, no. 9, pp. 4389-4392, 1995.

[11] H. Harima, "Properties of GaN and related compounds studied by means of Raman scattering," *Journal of Physics: Condensed Matter,* vol. 14, no. 38, p. R967, 2002.

[12] A. Neves and M. H. Nazaré, *Properties, growth and applications of diamond* (no. 26). IET, 2001.

[13] H. O. Pierson, *Handbook of carbon, graphite, diamonds and fullerenes: processing, properties and applications*. William Andrew, 2012.

[14] C. E. Nebel, "Electronic properties of CVD diamond," *Semiconductor Science and Technology,* vol. 18, no. 3, p. S1, 2003.

[15] C. Kittel, *Introduction to solid state physics*. Wiley New York, 1976.

[16] J. D. Jackson, "Classical electrodynamics john wiley & sons," *Inc., New York,* vol. 13, 1999.

[17] L. M. Fu, *Modern semiconductor quantum physics*. World scientific, 1995.

[18] Y. Leng, *Materials characterization: introduction to microscopic and spectroscopic methods*. John Wiley & Sons, 2009.

[19] O. Ambacher, "Growth and applications of group III-nitrides," *Journal of Physics D: Applied Physics,* vol. 31, no. 20, p. 2653, 1998.

[20] U. K. Mishra, P. Parikh, and Y.-F. Wu, "AlGaN/GaN HEMTs-an overview of device operation and applications," *Proceedings of the IEEE,* vol. 90, no. 6, pp. 1022-1031, 2002.

[21] S. Sze, "Physics of Semiconductor Devices, Jhon Wiley &," *New York,* pp. 96-98, 1981.

[22] W. Hayes and R. Loudon, *Scattering of light by crystals*. Courier Corporation, 2012.

[23] T. Kozawa *et al.,* "Raman scattering from LO phonon-plasmon coupled modes in gallium nitride," *Journal of Applied Physics,* vol. 75, no. 2, pp. 1098-1101, 1994.

[24] R. Loudon, "The Raman effect in crystals," *Advances in Physics,* vol. 13, no. 52, pp. 423-482, 1964.

[25] M. Seon, M. Holtz, W. Duncan, and T. Kim, "Raman studies of heavily carbon doped GaAs," *Journal of applied physics,* vol. 85, no. 10, pp. 7224-7230, 1999.

[26] A. Barker Jr and A. J. Sievers, "Optical studies of the vibrational properties of disordered solids," *Reviews of Modern Physics,* vol. 47, no. S2, p. S1, 1975.

[27] M. Stavola and W. B. Fowler, "Tutorial: Novel properties of defects in semiconductors revealed by their vibrational spectra," *Journal of Applied Physics,* vol. 123, no. 16, p. 161561, 2018.

[28] J. Gracio, Q. Fan, and J. Madaleno, "Diamond growth by chemical vapour deposition," *Journal of Physics D: Applied Physics,* vol. 43, no. 37, p. 374017, 2010.

[29] Y. Hirose, S. Amanuma, and K. Komaki, "The synthesis of high-quality diamond in combustion flames," *Journal of applied physics,* vol. 68, no. 12, pp. 6401-6405, 1990.

[30] K. Kurihara, K. Sasaki, M. Kawarada, and Y. Goto, "Formation of functionally gradient diamond films," in *Materials Science Monographs*, vol. 73: Elsevier, 1991, pp. 461-466.

[31] M. Ohring, *Materials science of thin films*. Elsevier, 2001.

[32] J. Venables and G. Spiller, "Nucleation and growth of thin films," in *Surface Mobilities on Solid Materials*: Springer, 1983, pp. 341-404.

[33] A. C. Jones and M. L. Hitchman, *Chemical vapour deposition: precursors, processes and applications*. Royal society of chemistry, 2009.

[34] A. Siddique, R. Ahmed, J. Anderson, and E. L. Piner, "Effect of reactant gas stoichiometry of in-situ SiNx passivation on structural properties of MOCVD AlGaN/GaN HEMTs," *Journal of Crystal Growth,* vol. 517, pp. 28-34, 2019.

[35] K. Hiramatsu, K. Nishiyama, A. Motogaito, H. Miyake, Y. Iyechika, and T. Maeda, "Recent Progress in Selective Area Growth and Epitaxial Lateral Overgrowth of III-Nitrides: Effects of Reactor Pressure in MOVPE Growth," *physica status solidi (a),* vol. 176, no. 1, pp. 535-543, 1999.

[36] D. Kapolnek *et al.*, "Anisotropic epitaxial lateral growth in GaN selective area epitaxy," *Applied Physics Letters,* vol. 71, no. 9, pp. 1204-1206, 1997.

[37] D. Koleske, A. Wickenden, R. Henry, W. DeSisto, and R. Gorman, "Growth model for GaN with comparison to structural, optical, and electrical properties," *Journal of Applied Physics,* vol. 84, no. 4, pp. 1998-2010, 1998.

[38] V. Jirásek, T. Ižák, M. Varga, O. Babchenko, and A. Kromka, "Investigation of residual stress in structured diamond films grown on silicon," *Thin Solid Films*, vol. 589, pp. 857-863, 2015, doi: 10.1016/j.tsf.2015.07.022.

[39] G. A. Slack and S. F. Bartram, "Thermal expansion of some diamondlike crystals," *Journal of Applied Physics*, vol. 46, no. 1, pp. 89-98, 1975, doi: 10.1063/1.321373.

[40] Y. Okada and Y. Tokumaru, "Precise determination of lattice parameter and thermal expansion coefficient of silicon between 300 and 1500 K," *Journal of Applied Physics*, vol. 56, no. 2, pp. 314-320, 1984, doi: 10.1063/1.333965.

[41] R. R. Reeber and K. Wang, "Lattice parameters and thermal expansion of GaN," *Journal of Materials Research*, vol. 15, no. 1, pp. 40-44, 2011, doi: 10.1557/jmr.2000.0011.

[42] P. Hess, "The mechanical properties of various chemical vapor deposition diamond structures compared to the ideal single crystal," *Journal of Applied Physics*, vol. 111, no. 5, 2012, doi: 10.1063/1.3683544.

[43] M. A. Hopcroft, W. D. Nix, and T. W. Kenny, "What is the Young's Modulus of Silicon?," *Journal of Microelectromechanical Systems*, vol. 19, no. 2, pp. 229-238, 2010, doi: 10.1109/jmems.2009.2039697.

[44] J. W. Anderson, "Characterization of Diamond-Semiconductor Interfaces," Ph.D, Material Science, Engineering and Commercialization, Texas State University, 2020.

[45] D. Gogova *et al.*, "A new approach to grow C-doped GaN thick epitaxial layers," *physica status solidi c*, vol. 8, no. 7-8, pp. 2120-2122, 2011.

[46] D. E. Aspnes and A. Studna, "Dielectric functions and optical parameters of si, ge, gap, gaas, gasb, inp, inas, and insb from 1.5 to 6.0 ev," *Physical review B*, vol. 27, no. 2, p. 985, 1983.

[47] K. D. Malcolm, "Characterization of the Thermal Properties of Chemical Vapor Deposition Grown Diamond Films for Flectronics Cooling.," Thesis, School of Mechanical Engineering, Georgia Institute of Technology, 2016.

[48] P. Perlin, C. Jauberthie-Carillon, J. P. Itie, A. San Miguel, I. Grzegory, and A. Polian, "Raman scattering and x-ray-absorption spectroscopy in gallium nitride under high pressure," *Physical Review B*, vol. 45, no. 1, p. 83, 1992.

[49] D. Manchon Jr, A. Barker Jr, P. Dean, and R. Zetterstrom, "Optical studies of the phonons and electrons in gallium nitride," *Solid State Communications*, vol. 8, no. 15, pp. 1227-1231, 1970.

[50] S. Nikishin *et al.*, "High quality GaN grown on Si (111) by gas source molecular beam epitaxy with ammonia," *Applied physics letters*, vol. 75, no. 14, pp. 2073-2075, 1999.

[51] I.-H. Lee *et al.*, "Stress relaxation in Si-doped GaN studied by Raman spectroscopy," *Journal of applied physics*, vol. 83, no. 11, pp. 5787-5791, 1998.

[52] R. Zhang and T. F. Kuech, "Photoluminescence of carbon in situ doped GaN grown by halide vapor phase epitaxy," *Applied physics letters*, vol. 72, no. 13, pp. 1611-1613, 1998.

[53] D. As and U. Köhler, "Carbon-an alternative acceptor for cubic GaN," *Journal of Physics: Condensed Matter*, vol. 13, no. 40, p. 8923, 2001.

[54] H. Tang, J. Webb, J. Bardwell, S. Raymond, J. Salzman, and C. Uzan-Saguy, "Properties of carbon-doped GaN," *Applied Physics Letters,* vol. 78, no. 6, pp. 757-759, 2001.

[55] C. Seager, A. Wright, J. Yu, and W. Götz, "Role of carbon in GaN," *Journal of applied physics,* vol. 92, no. 11, pp. 6553-6560, 2002.

[56] S. Fischer, C. Wetzel, E. Haller, and B. Meyer, "On p-type doping in GaN—acceptor binding energies," *Applied physics letters,* vol. 67, no. 9, pp. 1298-1300, 1995.

[57] C. Abernathy, J. MacKenzie, S. Pearton, and W. Hobson, "CCl 4 doping of GaN grown by metalorganic molecular beam epitaxy," *Applied physics letters,* vol. 66, no. 15, pp. 1969-1971, 1995.